

WEB-SPLINES SOLUTION OF 3D ELECTROMAGNETIC PROBLEMS

by

Fulya Kunter

B.S., in Electronic and Communication Engineering, Yıldız Technical University, 2001

M.S., in Electrical and Electronics Engineering, Boğaziçi University, 2004

Submitted to the Institute for Graduate Studies in  
Science and Engineering in partial fulfillment of  
the requirements for the degree of  
Doctor of Philosophy

Graduate Program in Electrical and Electronics Engineering  
Boğaziçi University

2011

*To my son, Alp Erol Kunter ...*

## ACKNOWLEDGEMENTS

I would like to express my deepest gratitude to my PhD supervisor, Prof. Ş. Selim Şeker, for his guidance and valuable help throughout the thesis. He provided me with a better understanding of many concepts as well as academic insight. His contributions will effect in the rest of my academic life.

I would like to thank Prof. Avni Morgül and Prof. Tayfun Günel for their precious feedback and scientific comments about my PhD research. I would also like to thank Prof. Oğuzhan Çiçekođlu and Prof. M. Tunaya Kalkan for being part of my defense jury.

I would like to thank Dr. Gökhan Apaydın for giving me the chance to work on this topic, to Dr. Nazlı Güney for her constructive contributions and suggestions, and to Assos. Prof. Şükrü Özen. I have special thanks to my friends and colleagues, especially Dr. Belkis Ünaldı, and Erdal Kayacan. A short break with them was enough to make long hours of work bearable. Thank you for being so special. Thanks to my friends, Dr. Hatice Akakın, Oya Çeliktutan, Yasin Çitkaya, Dr. Emre Arslan, Yeşim Öniz, Özkan Çiğdem, Çisel Aras, and İpek Şen for their friendship and support.

I could not succeed without the support of my family. I am grateful to my father, Prof. Fethi Çallıalp, for his extensive knowledge of mathematics, and my mother Füsün Çallıalp, who has continued to stand beside me anytime that I was in need. I would also like to thank the members of Kunter family for their encouragement. Finally, my very very special thanks goes to my husband Sedat Oytun for his continuous support all these years. Thank you for being with me and all your patience. Without his love, presence beside me, his encouragement and support, this thesis would never have started or ended. I hope that now I can spend more time with my sweet son, Alp Erol, and husband.

## ABSTRACT

# WEB-SPLINES SOLUTION OF 3D ELECTROMAGNETIC PROBLEMS

This dissertation proposes the weighted extended basis splines (web-splines) approach in the finite element method (FEM) for electrostatic, electromagnetic, and bioheat problems for radially symmetric and three dimensional (3D) structures. The most important advantage of this new method is that it does not need mesh generation which overcomes some of the drawbacks of using meshes and piecewise-uniform or linear trial functions.

In this thesis, the theoretical development of web-spline formulations has been done. The mathematical contributions have been supported by the simulations in both electrostatic and electromagnetic wave problems for inhomogeneous boundary conditions in cylindrical coordinates for the first time. Furthermore, this newly developed computational approach is employed to calculate the steady-state temperature distribution in a normal human eye. As a first step, the human eye is evaluated in two dimensions (2D). The simulation results which are verified using the values reported in the literature, point out to better efficiency in terms of the accuracy level. Next, to give a more precise representation of the actual human eye, 3D modeling is simulated using these new finite elements in conjunction with linear, quadratic and cubic b-splines. Grid convergence number estimates are derived for both sets of simulations. It is shown that this method reaches higher precision in a shorter period of time with fewer nodes. Finally, FEM with web-spline computer modeling have been applied to human eye to study the intraocular temperature during microwave irradiation. Our findings indicate that web-spline solutions improve the computational methods for health care.

## ÖZET

### ÜÇ BOYUTLU ELEKTROMANYETİK PROBLEMLERİNİN WEB-SPLINE ÇÖZÜMÜ

Bu tez, radial simetri ve üç boyutlu (3B) yapılar için elektrostatik, elektromanyetik ve biyo-ısı problemlerinde sonlu eleman yönteminde ağırlıklı genişletilmiş b-spline yaklaşımını önermektedir. Ağ oluşumuna ihtiyaç duymayan bu yeni yöntemin en önemli yanı, ağ, parça-düzgün veya doğrusal test fonksiyonlarının kullanımındaki sonlu eleman yöntemindeki eksikliklerin üstesinden gelebilmesidir.

Tezde, ağırlıklı genişletilmiş b-spline formülasyonunun teorik gelişimi yapılmış ve ilk olarak silindirik koordinatlarda homojen olmayan sınır koşulları için elektrostatik ve elektromanyetik dalga problemlerinde matematiksel katkılar benzetimlerle desteklenmiştir. Buna ek olarak, bu yeni geliştirilmiş sayısal yaklaşım, normal bir insan gözünde kararlı hal sıcaklık dağılımının hesabı için kullanılmıştır. İlk olarak, insan gözü iki boyutlu (2B) olarak değerlendirilmiştir. Literatürde verilen değerler kullanılarak doğrulaması yapılan benzetim sonuçlarının, kesinlik seviyesi açısından çok başarılı olduğu gösterilmiştir. Daha sonra, daha gerçekçi bir insan gözü sunabilmek için, doğrusal, ikinci dereceden ve üçüncü dereceden b-splinelarla birlikte yeni sonlu elemanlar kullanılarak üç boyutlu (3B) modelin benzetimi yapılmıştır. Her iki benzetim için de ızgara yakınlık sayısı tahmini yapılmıştır. Bu da, çok az düğüm sayısı ile çok kısa zaman periyodunda daha yüksek kesinliğe ulaşıldığını göstermiştir. Son olarak, ağırlıklı genişletilmiş b-spline sonlu eleman yöntemi bilgisayar modeli, mikrodalga yayılımı sırasında insan gözündeki sıcaklık etkilerini hesaplamak için kullanılmıştır. Sonuçlar, ağırlıklı genişletilmiş b-spline çözümlerinin, sağlık hizmetlerinde sayısal yöntemlerin iyileştirdiğini göstermektedir.

## TABLE OF CONTENTS

ACKNOWLEDGEMENTS . . . . .	iv
ABSTRACT . . . . .	v
ÖZET . . . . .	vi
LIST OF FIGURES . . . . .	ix
LIST OF TABLES . . . . .	xiii
LIST OF SYMBOLS/ABBREVIATIONS . . . . .	xiv
1. INTRODUCTION . . . . .	1
1.1. Research Overview and Contributions . . . . .	3
1.2. Outline of the Thesis . . . . .	4
2. OVERVIEW OF ELECTROMAGNETICS AND SPLINES . . . . .	5
2.1. The Maxwell's Equations . . . . .	5
2.2. Vector Wave Equations . . . . .	7
2.3. Boundary Conditions . . . . .	8
2.4. Finite Element Method . . . . .	10
2.5. B-splines . . . . .	14
2.5.1. The Concept of Splines . . . . .	15
2.5.2. Scalar and Tensor Products of B-splines . . . . .	18
2.5.3. Error Analysis . . . . .	19
3. FEM WITH B-SPLINES . . . . .	22
3.1. Flow Chart . . . . .	22
3.2. Classification of b-splines . . . . .	24
3.3. Extension Coefficients . . . . .	24
3.4. The Weight Function . . . . .	28
3.5. Weighted Extended B-splines . . . . .	30
4. WEB-SPLINE APPLICATIONS FOR ONE AND TWO DIMENSIONS . . . . .	32
4.1. One Dimensional EM Problems . . . . .	32
4.1.1. Electromagnetic Waves Between Parallel Plates . . . . .	33
4.2. Two Dimensional EM Problems . . . . .	34
4.2.1. Wave Equation Analysis For Circular Domain . . . . .	35

5. RADIALLY SYMMETRIC WEIGHTED EXTENDED B-SPLINE MODEL	38
5.1. Web-spline in cylindrical coordinate	38
5.2. FEM with web-spline	41
5.3. Numerical results	45
5.3.1. Electrostatic problems	45
5.3.2. The EM wave equation	48
5.3.3. Conclusion	50
6. 3D WEB-SPLINES SOLUTION TO HUMAN EYE HEAT DISTRIBUTION USING BIOHEAT EQUATION	53
6.1. Introduction	53
6.2. Mathematical Model of the Human Eye	54
6.3. Method of Analysis	57
6.3.1. The Weak Formulation of the Bioheat Equation	57
6.3.2. Web-spline Approximation	59
6.4. Simulation Results	59
6.4.1. 2D results	59
6.4.2. 3D results	62
6.5. Conclusion	68
7. WEB-SPLINE COMPUTATION OF TEMPERATURE RISE WITHIN A MODEL OF THE MICROWAVE-IRRADIATED HUMAN EYE	69
7.1. Introduction	69
7.2. Thermal Model of The Human eye	71
7.2.1. Electrical Parameters of Eye	71
7.2.2. Time Dependent Heat Conduction	73
7.2.3. Derivation of Finite Element Equations	74
7.2.4. Numerical Time Integration	76
7.3. Simulation Results	78
7.4. Conclusion	79
8. CONCLUSIONS	84
8.1. Contributions and Discussion	84
8.2. Future Directions	85
REFERENCES	86

## LIST OF FIGURES

Figure 1.1.	A solid perfectly conducting sphere is modeled with wire grid. Each wire is divided into subsegments. BEM calculates the current induced on each subsegment . . . . .	2
Figure 2.1.	Structured tetrahedral mesh around a metallic sphere . . . . .	11
Figure 2.2.	Linear tetrahedral element . . . . .	12
Figure 2.3.	The uniform b-splines . . . . .	15
Figure 2.4.	Cubic b-spline functions . . . . .	17
Figure 2.5.	The derivative of cubic b-spline . . . . .	18
Figure 2.6.	Tensor product of cubic b-spline in 2D and first order partial derivative of cubic b-spline with respect to $x$ . . . . .	19
Figure 2.7.	Tensor product of cubic b-spline in 3D and first order partial derivative of cubic b-spline with respect to $x$ . . . . .	20
Figure 3.1.	The flow diagram of FEM with web-method . . . . .	23
Figure 3.2.	The projection view of layers and all layers of the sphere . . . . .	25
Figure 3.3.	Outer and inner b-splines for degree $n=1$ . . . . .	25
Figure 3.4.	Outer and inner b-splines for degree $n=2$ . . . . .	26
Figure 3.5.	Outer and inner b-splines for degree $n=3$ . . . . .	26

Figure 3.6.	Outer and inner b-splines for degree $n=3$ for three layers of sphere domain . . . . .	27
Figure 3.7.	All relevant outer and inner b-splines for degree $n=3$ . . . . .	27
Figure 3.8.	The weight functions . . . . .	30
Figure 3.9.	The weight function using Rvachev's R-function . . . . .	31
Figure 4.1.	Parallel plates . . . . .	33
Figure 4.2.	Error analysis of parallel plates using standard FEM (solid) and linear (dash), quadratic (dot), and cubic (dash-dot) web-splines . .	34
Figure 4.3.	Triangulation for circular domain . . . . .	36
Figure 4.4.	Quadratic extended b-splines for circular domain . . . . .	36
Figure 4.5.	The relative $L_2$ error norm for various basis functions which are linear Lagrange polynomial ( $\Delta$ ), linear ( $\circ$ ), quadratic ( $\bullet$ ), and cubic ( $\diamond$ ) extended b-splines versus the number of nodes for circular domain . . . . .	37
Figure 5.1.	The weight function . . . . .	40
Figure 5.2.	The standard ( $\bullet$ ), extended inner ( $\blacktriangle$ ) and outer ( $\circ$ ) web-splines for coaxial cable . . . . .	41
Figure 5.3.	Coaxial cable . . . . .	46
Figure 5.4.	Error analysis for the coaxial cable using standard FEM, linear, quadratic, and cubic web-splines for a grid width of 2.5 mm . . . .	47

Figure 5.5.	Error analysis for the coaxial cable using standard FEM, linear, quadratic, and cubic web-splines for a grid width of 1.0 mm in logarithmic scale . . . . .	48
Figure 5.6.	The $L_2$ error norm of coaxial cable for various basis functions versus the number of nodes . . . . .	49
Figure 5.7.	The error analysis of the coaxial cable using standard FEM (solid), linear (grey), quadratic (dot), and cubic (dash-dot) web-splines for a grid width of 0.1 mm in logarithmic scale . . . . .	51
Figure 5.8.	Maximum error analysis versus permittivity using standard FEM (solid), and linear (dash), quadratic (dot), and cubic (dash-dot) web-splines . . . . .	52
Figure 6.1.	The 2D human eye model . . . . .	55
Figure 6.2.	Grid convergence for the 2D web-spline model . . . . .	60
Figure 6.3.	The standard ( $\bullet$ ), extended inner ( $\blacktriangle$ ) and outer ( $\circ$ ) cubic b-splines for the human eye . . . . .	61
Figure 6.4.	Thermal pattern of the 2D model without exposure to radiation . . . . .	61
Figure 6.5.	Comparison between the 2D web-spline model, [49] and [51] . . . . .	62
Figure 6.6.	The 3D human eye model . . . . .	63
Figure 6.7.	Grid convergence for the 3D web-spline model . . . . .	64
Figure 6.8.	Grid representation for the 3D human eye model . . . . .	65

Figure 6.9.	Comparison of the results for the 3D model using the methods in [49], [52] and the cubic web-spline method . . . . .	67
Figure 6.10.	Comparison of the results for the 3D model using the method in [52] and the linear, quadratic, and cubic web-spline method . . . . .	67
Figure 7.1.	Dielectric and conductivity variations of cornea tissue . . . . .	72
Figure 7.2.	Temperature rise on the cornea surface at 6 min. duration at 5 $mW/cm^2$ . . . . .	79
Figure 7.3.	Temperature rise on the cornea surface at 6 min. duration at 10 $mW/cm^2$ . . . . .	80
Figure 7.4.	Temperature rise on the cornea surface at 6 min. duration at 10 $mW/cm^2$ . . . . .	81
Figure 7.5.	Temperature rise on the cornea surface at 6 min. duration at 6 GHz	82
Figure 7.6.	Temperature rise on the cornea surface at 6 min. duration at 10 GHz	82
Figure 7.7.	Cubic web-spline solution of temperature rise on the human eye for $I_0 = 5mW/cm^2$ at 10 GHz (-.), 6 GHz (-) and 2.45 GHz (-) . . . . .	83

## LIST OF TABLES

Table 2.1.	The classification of boundary conditions . . . . .	10
Table 2.2.	The representation of polynomials for linear, quadratic, and cubic 1D b-splines . . . . .	16
Table 2.3.	The representation of polynomials for linear, quadratic, and cubic 3D b-splines . . . . .	16
Table 3.1.	3D extension coefficients . . . . .	29
Table 3.2.	The weight functions and rule for the 3D domain . . . . .	30
Table 5.1.	Spline functions used in cylindrical coordinates . . . . .	39
Table 6.1.	Properties of the human eye for different domains [51] . . . . .	56
Table 6.2.	Efficiency comparison of web-splines with standard FEM studies . . . . .	63
Table 6.3.	The summary of the results of the corneal surface temperature ob- tained from the previous studies . . . . .	66
Table 6.4.	Comparison between the mean value of the experimental results, 34.65°C with FEM and the web-spline method solutions on the corneal surface . . . . .	68
Table 7.1.	Electrical parameters of the cornea at the certain frequencies . . . . .	73
Table 7.2.	Temperature increase values on the cornea surface for plan wave exposure . . . . .	81

## LIST OF SYMBOLS/ABBREVIATIONS

$1D$	One dimensional
$2D$	Two dimensional
$3D$	Three dimensional
$a$	The maximum diameter of circle circumscribing domain
$\mathbf{B}$	Magnetic flux density vector
$B$	Basis function
$\mathbf{D}$	Electric flux density vector
$e$	Error
$\mathbf{E}$	Electric field intensity vector
$f$	Frequency
$F$	Load matrix
$h$	Grid width
$\mathbf{H}$	Magnetic field intensity vector
$I$	Set of inner b-splines
$j$	Imaginary unit
$\mathbf{J}$	Electric current density vector
$J$	Set of outer b-splines
$K$	Stiffness matrix
$\tilde{k}$	Wave number
$m$	Dimension
$M$	Mass matrix
$\mathbf{M}$	Magnetic current density vector
$\hat{n}$	The normal unit vector
$n$	Degree of functions
$R$	Reflection coefficient
$T$	Thickness
$u$	Time harmonic magnetic and electric field
$u_e$	Exact solution
$\tilde{u}$	Approximated solution

$U$	Matrix consisting of coefficients
$v$	Smooth function
$w$	Weight function
$\Delta$	Laplace operator
$\nabla$	Gradient
$\nabla \cdot$	Divergence
$\nabla \times$	Curl
$\Omega$	Defined region
$\partial\Omega$	Boundary of the region
$\beta$	Loss parameter
$\gamma$	Smoothing parameter
$\delta$	Size of boundary strip
$\varepsilon$	Permittivity
$\varepsilon_r$	Relative permittivity
$\mu$	Permeability
$\rho$	Electric charge density
$\sigma$	Electric conductivity
$\omega$	Wave angular frequency
BC	Boundary Condition
BEM	Boundary Element Method
CAD	Computer Aided Design
EM	Electromagnetic
FDTD	Finite Difference Time Domain
FEM	Finite Element Method
FVM	Finite Volume Method
MOM	Method of Moments
PDE	Partial Differential Equation
WEB-SPLINES	Weighted Extended Basis Splines

## 1. INTRODUCTION

The discovery and understanding of electromagnetic (EM) phenomena can be traced back thousands of years, to when ancient philosophers were interested in the physical world around them. Lightning in the sky was the subject of heavenly worship, but complex electromagnetic processes were involved in the natural phenomenon, which is still being studied by scientists armed with the latest equipment. Those natural phenomena led to the recognition of the existence of electric power, yet a truly scientific explanation and quantization were completed a little more than a century ago. Generation and utilization of such power for human life have fully blossomed only in the last few decades.

Although most electrical engineering curricula begin with a study of electric and magnetic circuits, it is now recognized that the more basic theory of the electric and magnetic fields deserves subsequent attention in approximating the EM field equations. Numerical techniques for calculating electromagnetic fields surpassed analytical techniques many years ago. Analytical methods work for only a few basic geometries that do not apply to most practical problems. There are more articles on numerical calculation of fields than on analytical calculation. The computer has become a critical part of electromagnetics.

Computational electromagnetics is the simulation of Maxwell's equations and their variations on a computer. Numerical approaches to solving Maxwell's equations find the fields in either the time domain or frequency domain. Maxwell's equations have yielded some partial differential equations (PDE) which model the behavior of the electromagnetic waves. These equations are widely used in engineering designs and are often difficult to solve analytically.

Numerical solutions of electromagnetic scattering and radiation problems are obtained by solving partial differential equations with different methods. The most widely used techniques are Finite Difference Time Domain (FDTD) Method, Boundary El-

ement Method (BEM) or Method of Moments (MOM), and Finite Element Method (FEM). Thus, numerical computation techniques promote faster and more accurate solution techniques.

FDTD was developed by Yee in 1966 [1]. His idea was to divide the three dimensional region into cubic cells, take values of points on each cell, and to convert the partial derivatives into difference equations. The idea comes from Taylor expansions. The finite differences are used to approximate derivatives. In this method, continuous equations are replaced with their finite difference of values of selected points, which are easy to implement. However it is difficult to implement this method for complex objects.

BEM requires calculating only boundary values, rather than values throughout the space defined by a partial differential equation. It is controlled by points on the boundary of the domain. It is a way of converting integral equations to matrix equations. This technique works best for wires and flat plates. More complex systems are assembled from wires and/or metal plates. Each wire or metal plate is further subdivided into wire segments or patches that are small compared to the frequency's wavelength. Figure 1.1 shows an example of a solid sphere modeled using wires [2].

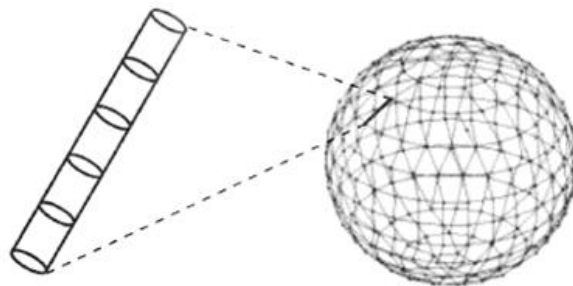


Figure 1.1. A solid perfectly conducting sphere is modeled with wire grid. Each wire is divided into subsegments. BEM calculates the current induced on each subsegment

In FEM, which is an important tool in this work, the problem space is subdivided into finite regions (elements) over which the solution is assumed to follow a simple local

approximating trial function, and then minimizes the energy of the given function for the given domain [3].

Although FDTD and BEM are conceptually simpler and easier to program than FEM, FEM is a more powerful and versatile numerical technique for handling problems involving complex geometries and inhomogeneous media. The systematic generality of the method makes it possible to construct general purpose computer programs for solving a wide range of problems. Consequently, programs developed for a particular discipline have been applied successfully to solve problems in a different field with little or no modification [4].

### 1.1. Research Overview and Contributions

This study presents on the use of web-splines in the FEM method. The spline functions are often used in approximation, data fitting, computer aided design (CAD), and many other applications [5, 6]. The contributions of Carl De Boor, de Casteljaou, and Bezier have played an important role for splines. The b-splines can be used as basis functions for their flexibility and continuity between points. Many researches have been done on spline finite element solutions [7-9]. Despite the fact that boundary conditions and stability requirements prevent b-splines from being used on uniform grids, these difficulties can be overcome with the new method called web-spline. Hollig [10] constructed the web-spline method and used it with the FEM. Thus the combined advantages of standard finite elements and web-spline representations inspired many authors to work on this new subject [11-19].

This study will illustrate the web-splines as basis functions for FEM in axisymmetrical 3D EM problems and in bioheat transfer problems for analyzing the temperature distribution in 2D and 3D models of the human eye with and without external sources. The benefits of using web-splines in solving axisymmetrical problems and approximating the heat distribution in the eye are that no mesh generation is required and uniform grids are used instead of irregular partitions of domain, thus eliminating the difficult and time consuming preprocessing step. In fact, as reported in this

dissertation, high accuracy can be obtained with relatively few parameters.

## 1.2. Outline of the Thesis

This thesis is organized as follows: In Chapter 2, we review the overview of electromagnetics, PDE, and FEM. After introducing the general background of FEM, it explains the b-splines.

Using FEM and b-splines, the steps of FEM with web-spline method are studied in Chapter 3. Finite element basis functions are constructed by using web-splines without mesh generation. Then, finite element assembly and solution are studied.

Chapter 4 shows the applications of EMs in one dimension (1D) and 2D. This chapter shows why the b-splines are used for constructing basis functions. The simulation results using FEM with b-splines are compared with the exact results and the general FEM methods.

The novel contributions of this research are explained in Chapters 5, 6 and 7. In Chapter 5, we apply FEM with web-spline technique to radially symmetric electrostatic and EM wave problems. The findings of the error analysis with the standard FEM analysis are also reported in this Chapter. Chapter 6 investigates the heat transfer in the normal unexposed 2D and 3D representations of the human eye. Web-spline model have been developed and employed to calculate the steady-state temperature distribution based on the properties and parameters reported in the literature. The presented method in Chapter 7 is based on the intraocular temperature distribution during microwave irradiation.

Although each chapter has its own concluding section, we summarize our results in Chapter 8. It concludes this dissertation with a summary of our findings and the future directions of our research.

## 2. OVERVIEW OF ELECTROMAGNETICS AND SPLINES

### 2.1. The Maxwell's Equations

Maxwell's equations are a set of fundamental equations that govern all macroscopic electromagnetic phenomena. The equations can be written in both differential and integral forms. For general time-varying fields, Maxwell's equations in integral form are given by

$$\oint_C \mathbf{E} dl = -\frac{d}{dt} \iint_S \mathbf{B} ds \quad (\text{Faraday's law}) \quad (2.1)$$

$$\oint_C \mathbf{H} dl = \frac{d}{dt} \iint_S \mathbf{D} ds + \iint_S \mathbf{J} ds \quad (\text{Maxwell - Ampere law}) \quad (2.2)$$

$$\oiint_S \mathbf{D} ds = \iiint_V \rho dv \quad (\text{Gauss's law}) \quad (2.3)$$

$$\oiint_S \mathbf{B} ds = 0 \quad (\text{Gauss's law - magnetic}) \quad (2.4)$$

where  $\mathbf{E}$  is electric field intensity ( $V/m$ ),  $\mathbf{D}$  is electric flux density ( $C/m^2$ ),  $\mathbf{H}$  is magnetic field intensity ( $A/m$ ),  $\mathbf{B}$  is magnetic flux density ( $Wb/m^2$ ),  $\mathbf{J}$  is electric current density ( $A/m^2$ ),  $\rho$  is electric charge density ( $C/m^3$ ) [20, 21].

In Equations (2.1) and (2.2),  $S$  is an arbitrary open surface bounded by contour  $C$ , whereas in Equations (2.3) and (2.4),  $S$  is a closed enclosing volume  $V$ .

Another fundamental equation, known as the equation of continuity, is given by:

$$\oiint_S \mathbf{J} ds = -\frac{d}{dt} \iiint_V \rho dv \quad (2.5)$$

This equation, which can be derived from (2.2) and (2.3), is the mathematical form of the law of the conservation of charge. Equations (2.1) - (2.5) are valid in all circumstances regardless of the medium and the shape of the integration volume, surface, and contour. They can be considered as the fundamental equations governing the behavior of electromagnetic fields.

Maxwell's equations in differential form can be derived from (2.1) - (2.5) by using Gauss's and Stokes's theorems. When field quantities in Maxwell's equations are harmonically oscillating functions with a single frequency, the field is referred to as time-harmonic. Using the complex phasor notation, differential forms can be written in a simplified form as:

$$\nabla \times \mathbf{E} = -j\omega\mathbf{B} \quad (2.6)$$

$$\nabla \times \mathbf{H} = j\omega\mathbf{D} + \mathbf{J} \quad (2.7)$$

$$\nabla \cdot \mathbf{B} = 0 \quad (2.8)$$

$$\nabla \cdot \mathbf{D} = \rho \quad (2.9)$$

$$\nabla \cdot \mathbf{J} = -j\omega\rho \quad (2.10)$$

where the time convention  $e^{j\omega t}$  is used and suppressed and  $\omega$  is angular frequency.

Maxwell's equations become definite when constitutive relations between the field quantities are specified. The constitutive relations describe the macroscopic properties of the medium being considered. For a simple medium, they are:

$$\mathbf{D} = \varepsilon \mathbf{E} \quad (2.11)$$

$$\mathbf{B} = \mu \mathbf{H} \quad (2.12)$$

$$\mathbf{J} = \sigma \mathbf{E} \quad (2.13)$$

where the constitutive parameters,  $\varepsilon$ ,  $\mu$ , and  $\sigma$  denote, respectively, the permittivity ( $F/m$ ), permeability ( $H/m$ ), and conductivity ( $S/m$ ) of the medium. These parameters are tensors for anisotropic media and scalars for isotropic media. For inhomogeneous media, they are functions of position, whereas for homogeneous media they are not.

## 2.2. Vector Wave Equations

The differential wave equation for either  $\mathbf{E}$  or  $\mathbf{H}$  can be obtained from Equations (2.6) - (2.7) with the aid of the constitutive relations (2.11) - (2.13), by taking the curl of the equations and employing the following vector identity:

$$\nabla \times \nabla \times \mathbf{E} = \nabla(\nabla \cdot \mathbf{E}) - \nabla^2 \mathbf{E} \quad (2.14)$$

$$\nabla \times \nabla \times \mathbf{H} = \nabla(\nabla \cdot \mathbf{H}) - \nabla^2 \mathbf{H} \quad (2.15)$$

Since the divergences of the field quantities are zero for the free source and no

conducting medium, vector wave equations are obtained as:

$$\nabla^2 \mathbf{E} + \omega^2 \mu \varepsilon \mathbf{E} = 0 \quad (2.16)$$

$$\nabla^2 \mathbf{H} + \omega^2 \mu \varepsilon \mathbf{H} = 0 \quad (2.17)$$

These wave equations must always be satisfied, whatever boundary conditions are imposed. The wave equations in Equations (2.16) and (2.17) can be written as:

$$\nabla^2 \mathbf{u} + \tilde{k}^2 \mathbf{u} = 0 \quad (2.18)$$

where  $\tilde{k} = \omega \sqrt{\mu \varepsilon}$  is the wave number,  $\omega$  is the wave angular frequency, and  $\mathbf{u}$  shows the time harmonic magnetic or electric field. This is called homogeneous wave equation or Helmholtz's equation.

### 2.3. Boundary Conditions

The EM fields obtained from the solution of Maxwell's equations must also satisfy the boundary conditions at the interface between different media. At a source-free interface between two media, medium 1 and medium 2, the fields must satisfy four conditions, given by

$$\hat{n} \times (\mathbf{E}_1 - \mathbf{E}_2) = \mathbf{M}_m \quad (2.19)$$

$$\hat{n} \cdot (\mathbf{D}_1 - \mathbf{D}_2) = \rho_s \quad (2.20)$$

$$\hat{n} \times (\mathbf{H}_1 - \mathbf{H}_2) = \mathbf{J}_s \quad (2.21)$$

$$\hat{n} \cdot (\mathbf{B}_1 - \mathbf{B}_2) = 0 \quad (2.22)$$

where the unit vector  $\hat{n}$  at the interface points into medium 1,  $\rho_s$  is the free surface electric charge density, and  $\mathbf{J}_s, \mathbf{M}_m$  are the free surface electric and magnetic current density at the interface, respectively. If magnetic current and charges are assumed to be ignored,  $\mathbf{M}_m$  and  $\rho_m$  are zero. So the tangential components of the electric field intensity vectors and the normal components of magnetic flux density vectors are continuous at the interface [22].

There are one of several types of classes of PDE problems defined by the information given at the boundary, including Dirichlet, Neumann and Cauchy problems. The general form of the boundary conditions can be shown as:

$$ru + \left( s_x \frac{\partial u}{\partial x} \hat{x} + s_y \frac{\partial u}{\partial y} \hat{y} + s_z \frac{\partial u}{\partial z} \hat{z} \right) \cdot \hat{n} = g(x, y, z) \quad (2.23)$$

where  $\hat{n}$  shows the outward normal unit vector of the region with the coefficients  $r, s$  and function  $g$  which depends on the boundary conditions. A dirichlet problem is the problem of finding a function which solves a specified PDE in the interior of a given region that takes prescribed values on the boundary of the region ( $s = 0$ ). As a concrete physical example one can give the problem of determining the steady temperature distribution inside a domain  $\Omega$ , if the temperature on its boundary  $\partial\Omega$  is given. Another example is that if the value of the field strength is held constant, then it would be known at that point in space. The boundary gives a value to the normal derivative of the field equation (u) ( $r = 0$ ) then it is a Neumann boundary condition. In this condition, unlike the Dirichlet condition, the Neumann condition ensures only that the equation has a unique solution up to an additional constant. If the Neumann condition is not zero, it does not have a physical meaning because a constant flux inside the domain cannot ensure that the solution is stationary. If the boundary has the form of a curve or surface that gives a value to the normal derivative and the field equation (u) itself then it is a Cauchy boundary condition [23]. The classification of boundary conditions are given in Table 2.1.

Table 2.1. The classification of boundary conditions

Boundary Condition	$r$	$s$
Dirichlet BC	nonzero	zero
Neumann BC	zero	nonzero
Cauchy BC	nonzero	nonzero

## 2.4. Finite Element Method

The finite element analysis of any problem involves basically four steps:

- 1) Discretizing the solution region into a finite number of subregions or elements,
- 2) Deriving governing equations for a typical element,
- 3) Assembling of all elements in the solution region, and
- 4) Solving the system of equations obtained.

The geometrical adaptability and low memory requirements of the FEM have made it one of the most popular numerical methods in all branches of engineering [23, 24, 25]. Its application to boundary value problems involves the subdivision of the computational domain (region where the fields are to be determined) into smaller elements. For two dimensional problems, these elements are typically triangles or quadrilaterals. A three dimensional mesh around a sphere is given as an example in Figure 2.1.

While some physical problems can be represented or approximated by a one or two dimensional mathematical model, all physical problems are three dimensional in nature. When a one or two dimensional representation or approximation is not possible, a three dimensional treatment is then necessary. In this part, the finite element method to three dimensions will be given in a very straightforward manner.

FEM for a general 3D problem, the boundary value problem under consideration

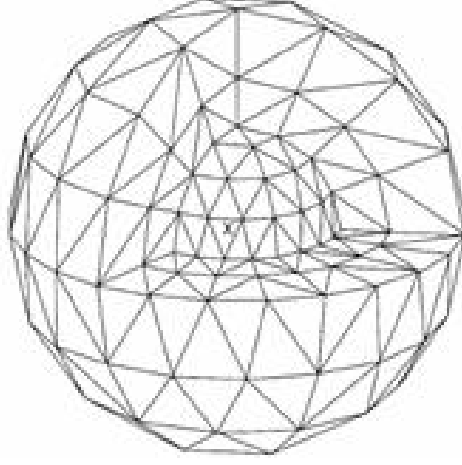


Figure 2.1. Structured tetrahedral mesh around a metallic sphere

is defined by the second order differential equation.

$$-\frac{\partial}{\partial x} \left( \alpha_x \frac{\partial \phi}{\partial x} \right) - \frac{\partial}{\partial y} \left( \alpha_y \frac{\partial \phi}{\partial y} \right) - \frac{\partial}{\partial z} \left( \alpha_z \frac{\partial \phi}{\partial z} \right) + \beta \phi = f, \quad (x, y, z) \in V \quad (2.24)$$

in conjunction with the boundary conditions

$$\phi = p \quad \text{on } S_1 \quad (2.25)$$

$$\left( \alpha_x \frac{\partial \phi}{\partial x} \hat{x} + \alpha_y \frac{\partial \phi}{\partial y} \hat{y} + \alpha_z \frac{\partial \phi}{\partial z} \hat{z} \right) \cdot \hat{n} + \gamma \phi = q(x, y, z) \quad \text{on } S_2 \quad (2.26)$$

where  $S = S_1 + S_2$  denotes the surface enclosing the volume  $V$  and  $\hat{n}$  is its outward normal unit vector.

Various approximation methods have been developed for FEM. This study presents Ritz-Galerkin approximation by minimizing the functional with respect to its variables. The equivalent variational problem for the boundary value problem defined above with

Equations (2.25) and (2.26), is given by:

$$\begin{aligned}
 F(\phi) = & \frac{1}{2} \iiint_V \left[ \alpha_x \left( \frac{\partial \phi}{\partial x} \right)^2 + \alpha_y \left( \frac{\partial \phi}{\partial y} \right)^2 + \alpha_z \left( \frac{\partial \phi}{\partial z} \right)^2 \right] dV + \iint_{S_2} \left( \frac{\gamma}{2} \phi^2 - q\phi \right) dS \\
 & - \iiint_V f\phi dV
 \end{aligned} \tag{2.27}$$

The first step of the finite element analysis is the discretization of the domain of interest. In this case the volume has to be subdivided into a number of small volume elements, tetrahedral elements. As a result, the surface  $S$  is broken into a number of triangular elements. Then, all volume elements with a set of integers and all nodes, which are the vertices of the tetrahedron, with another set of integers have to be labeled. The element numbers and node numbers can be related by a  $4 \times M$  integer array denoted by  $n(i,e)$ , where  $i=1,2,3,4$ ,  $e=1,2,3,\dots,M$ , and  $M$  denotes the total number of volume elements. Once the domain is discretized, the unknown function within each element

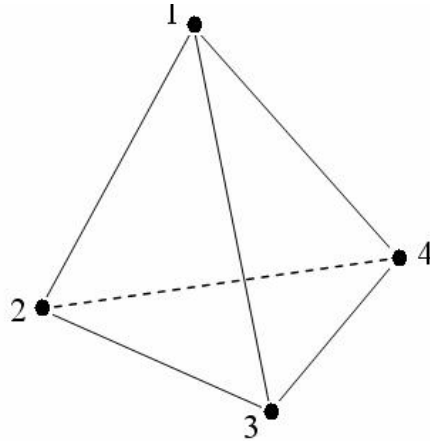


Figure 2.2. Linear tetrahedral element

has to be approximated. For this, the tetrahedral element illustrated in Figure 2.2 will be considered. Within the element, the unknown function  $\phi^e$  can be approximated with linear interpolation as:

$$\phi^e(x, y, z) = a^e + b^e x + c^e y + d^e z \tag{2.28}$$

In general form, the approximated solution  $\phi^e$  which consists of four nodes with the interpolation function is

$$\phi^e(x, y, z) = \sum_1^4 c_i B_i(x, y, z) \quad (2.29)$$

With the discretization and interpolation described above, the problem can be formulated in terms of the unknowns at the nodes using the Ritz-Galerkin method [23, 25].

$$F(\phi) = \sum_{e=1}^M F^e(\phi^e) \quad (2.30)$$

where  $M$  denotes the total number of volume elements and  $F^e$  is given by (2.27). Substituting (2.29) into (2.30) and taking the partial derivative of  $F^e$  with respect to  $\phi_i^e, i = 1, 2, 3, 4$ .

$$\begin{aligned} \frac{\partial F^e}{\partial \phi_i^e} = & \sum_{j=1}^4 c_j \iiint_{V^e} \left[ \alpha_x \left( \frac{\partial B_i}{\partial x} \frac{\partial B_k}{\partial x} \right) + \alpha_y \left( \frac{\partial B_i}{\partial y} \frac{\partial B_k}{\partial y} \right) + \alpha_z \left( \frac{\partial B_i}{\partial z} \frac{\partial B_k}{\partial z} \right) + \beta B_i B_k \right] dV \\ & + \alpha \gamma \iint_{S_2} B_i B_k dS - \iiint_{V^e} f B_k dV - \alpha \iint_{S_2} q B_k dS \end{aligned} \quad (2.31)$$

$$\sum_{i=1}^4 c_i [K_{i,k} + M_{i,k} + R_{i,k}] = F_k + G_k \quad (2.32)$$

After constructing the basis functions and taking the integral of each mesh in Equation (2.33), the linear system is assembled and solved

$$[K + M + R] \phi = F + G \quad (2.33)$$

where  $\phi$  is the matrix consisting of the coefficients of the basis functions,  $K$  is the stiffness matrix,  $M$  is the mass matrix,  $F$  is the load matrix, and  $R$  and  $G$  are matrices related to the boundary conditions.

## 2.5. B-splines

In the mathematical field of numerical analysis, a spline is a special function defined piecewise by polynomials. In the computer science subfields of computer-aided design and computer graphics, the term spline more frequently refers to a piecewise polynomial curve. Splines are popular curves in these subfields because of the simplicity of their construction, their accuracy of evaluation, and their capacity to approximate complex shapes through curve fitting and interactive curve design.

The term "spline" is used to refer to a wide class of functions that are used in applications requiring data interpolation and/or smoothing. Splines may be used for interpolation and/or smoothing of either one-dimensional or multi-dimensional data. They were developed by Carl de Boor, de Casteljaou, and Bezier [5, 6, 7]. They have become popular and many papers have been published on basis splines (b-splines).

The b-splines, which can be used as basis functions for their flexibility and continuity between points, have been taken into consideration to implement basis functions for FEM. It was proven that more accurate results are obtained by using b-spline basis functions as shape functions in order to solve two dimensional electromagnetic field problems for regular regions [25]. Hollig has used b-splines as basis functions to solve boundary value problems using FEM [10]. Using b-splines involving higher order shape functions is simple for the approximation of FEM applications. This method provides to solve electromagnetic problems with high accuracy and can also be applied to irregular domains.

The uniform b-spline  $b^n$  of degree  $n$  is defined by the recursion [5]

$$b^n(x) = \int_{x-1}^x b^{n-1}(t) dt \quad (2.34)$$

starting from the characteristic function  $b^0$  of the unit interval between zero and one. The uniform 3D b-spline  $b^n$  of degree  $n$  is also defined by (2.35). Figure 2.3 shows

the uniform 1D b-splines of degree one, two and three. These are linear (dotted line), quadratic (dashed line), and cubic (dash-dotted line) b-splines respectively. Cubic 1D b-spline functions which are defined by piecewise polynomials are given in Figure 2.4. Table 2.2 and Table 2.3 depict linear, quadratic, and cubic 1D and 3D b-splines which are obtained by using (2.34) and (2.35), respectively.

$$b^n(x, y, z) = \int_{x-1}^x \int_{y-1}^y \int_{z-1}^z b^{n-1}(k, l, m) dk dl dm \quad (2.35)$$

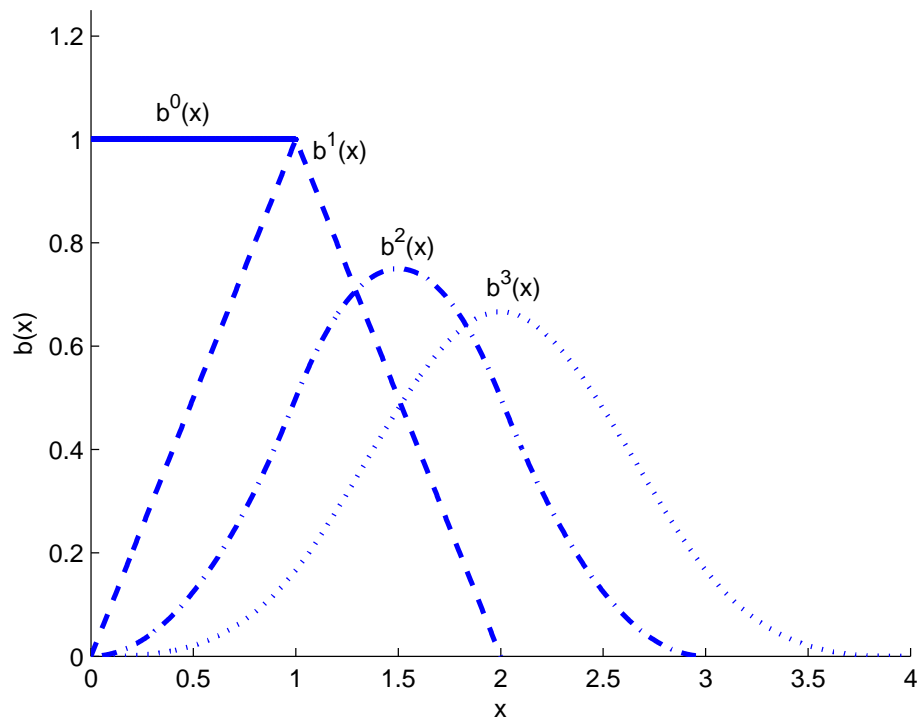


Figure 2.3. The uniform b-splines

### 2.5.1. The Concept of Splines

Identities for  $b^n$  generalize easily to the scaled translated b-splines with grid  $h$  supporting in  $[i, i + n + 1]h$  and scaled formula for the derivative are

$$b_{i,h}^n(x) = b^n(x/h - i) \quad (2.36)$$

Table 2.2. The representation of polynomials for linear, quadratic, and cubic 1D b-splines

$n$	The uniform 1D b-splines
1	$b^1(x) = \begin{cases} \int_0^x dt = x & x \in [0, 1] \\ \int_{x-1}^1 dt = 2 - x & x \in [1, 2] \\ 0 & \text{otherwise} \end{cases}$
2	$b^2(x) = \begin{cases} \int_0^x t dt = \frac{1}{2}x^2 & x \in [0, 1] \\ \int_{x-1}^1 t dt + \int_1^x (2-t) dt = -x^2 + 3x - \frac{3}{2} & x \in [1, 2] \\ \int_{x-1}^2 (2-t) dt = \frac{1}{2}x^2 - 3x + \frac{9}{2} & x \in [2, 3] \\ 0 & \text{otherwise} \end{cases}$
3	$b^3(x) = \begin{cases} \int_0^x \frac{1}{2}t^2 dt = \frac{1}{6}x^3 & x \in [0, 1] \\ \int_{x-1}^1 \frac{1}{2}t^2 dt + \int_1^x -t^2 + 3t - \frac{3}{2} dt = -\frac{1}{2}x^3 + 2x^2 - 2x + \frac{2}{3} & x \in [1, 2] \\ \int_{x-1}^2 -t^2 + 3t - \frac{3}{2} dt + \int_2^x \frac{1}{2}t^2 - 3t + \frac{9}{2} dt = \frac{1}{2}x^3 - 4x^2 + 10x - \frac{22}{3} & x \in [2, 3] \\ \int_{x-1}^3 \frac{1}{2}t^2 - 3t + \frac{9}{2} dt = -\frac{1}{6}x^3 + 2x^2 - 8x + \frac{32}{3} & x \in [3, 4] \\ 0 & \text{otherwise} \end{cases}$

Table 2.3. The representation of polynomials for linear, quadratic, and cubic 3D b-splines

$n$	The uniform 3D b-splines
1	$b^1(x, y, z) = \begin{cases} \int_0^x \int_0^y \int_0^z dkldm & x, y, z \in [0, 1] \\ \int_{x-1}^1 \int_{y-1}^1 \int_{z-1}^1 dkldm & x, y, z \in [1, 2] \\ 0 & \text{otherwise} \end{cases}$
2	$b^2(x, y, z) = \begin{cases} \int_0^x \int_0^y \int_0^z klm dkldm & x, y, z \in [0, 1] \\ \int_{x-1}^1 \int_{y-1}^1 \int_{z-1}^1 klm dkldm \\ + \int_1^x \int_1^y \int_1^z (2-k).(2-l).(2-z) dkldm & x, y, z \in [1, 2] \\ \int_{x-1}^2 \int_{y-1}^2 \int_{z-1}^2 (2-k).(2-l).(2-z) dkldm & x, y, z \in [2, 3] \\ 0 & \text{otherwise} \end{cases}$
3	$b^3(x, y, z) = \begin{cases} \int_0^x \int_0^y \int_0^z \frac{1}{8}k^2l^2m^2 dkldm & x, y, z \in [0, 1] \\ \int_{x-1}^1 \int_{y-1}^1 \int_{z-1}^1 \frac{1}{8}k^2l^2m^2 dkldm \\ + \int_1^x \int_1^y \int_1^z (-k^2 + 3k - \frac{3}{2})(-l^2 + 3l - \frac{3}{2})(-m^2 + 3m - \frac{3}{2}) dkldm & x, y, z \in [1, 2] \\ \int_{x-1}^2 \int_{y-1}^2 \int_{z-1}^2 (-k^2 + 3k - \frac{3}{2})(-l^2 + 3l - \frac{3}{2})(-m^2 + 3m - \frac{3}{2}) dkldm \\ + \int_2^x \int_2^y \int_2^z (\frac{1}{2}k^2 - 3k + \frac{9}{2})(\frac{1}{2}l^2 - 3l + \frac{9}{2})(\frac{1}{2}m^2 - 3m + \frac{9}{2}) dkldm & x, y, z \in [2, 3] \\ \int_{x-1}^3 \int_{y-1}^3 \int_{z-1}^3 (\frac{1}{2}k^2 - 3k + \frac{9}{2})(\frac{1}{2}l^2 - 3l + \frac{9}{2})(\frac{1}{2}m^2 - 3m + \frac{9}{2}) dkldm & x, y, z \in [3, 4] \\ 0 & \text{otherwise} \end{cases}$

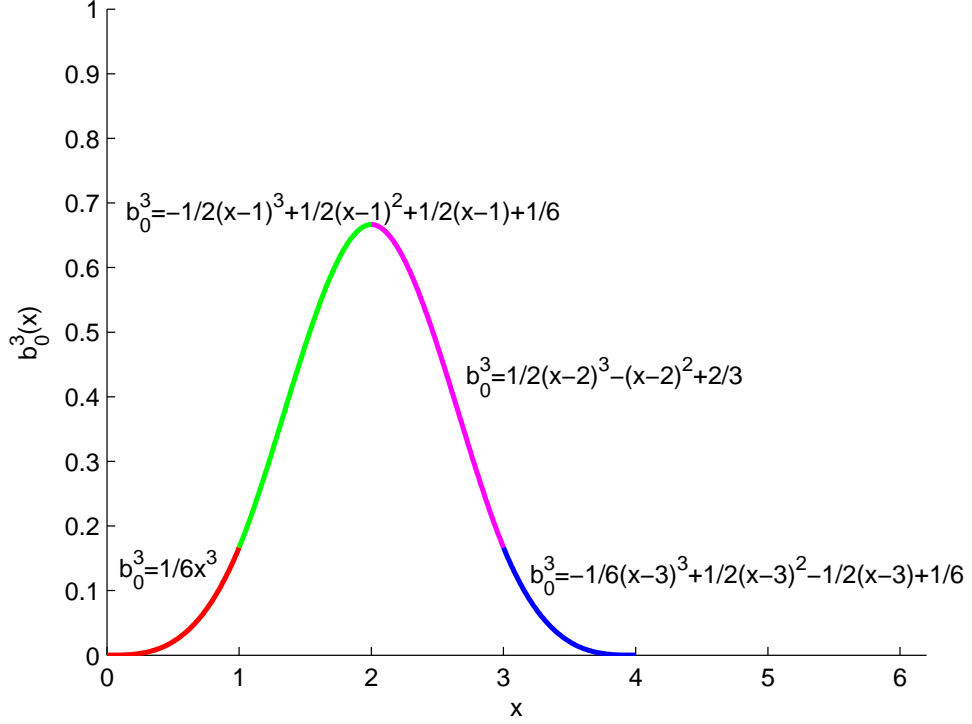


Figure 2.4. Cubic b-spline functions

$$\frac{d}{dx} b_{i,h}^n(x) = \frac{1}{h} [b_{i,h}^{n-1}(x) - b_{i+1,h}^{n-1}(x)] \quad (2.37)$$

While Equations (2.36) and (2.37) allow us to derive the main properties of b-splines in a straightforward manner, it is not well suited for computations. A simple algorithm for evaluating b-splines is provided by the following recurrence relation:

$$b_{i,h}^n(x) = \frac{1}{n} \left[ \left( \frac{x}{h} - i \right) b_{i,h}^{n-1}(x) + \left( n + i + 1 - \frac{x}{h} \right) b_{i+1,h}^{n-1}(x) \right] \quad (2.38)$$

Basis properties of  $b_{i,h}^n(x)$  are that they are positive on  $(0, n + 1)$  and vanishes outside this interval,  $(n - 1)$  times continuously differentiable, piecewise polynomial of degree  $n$  on each interval, symmetric and strictly monotone. Figure 2.5 shows the cubic and the derivative of cubic 1D b-spline.

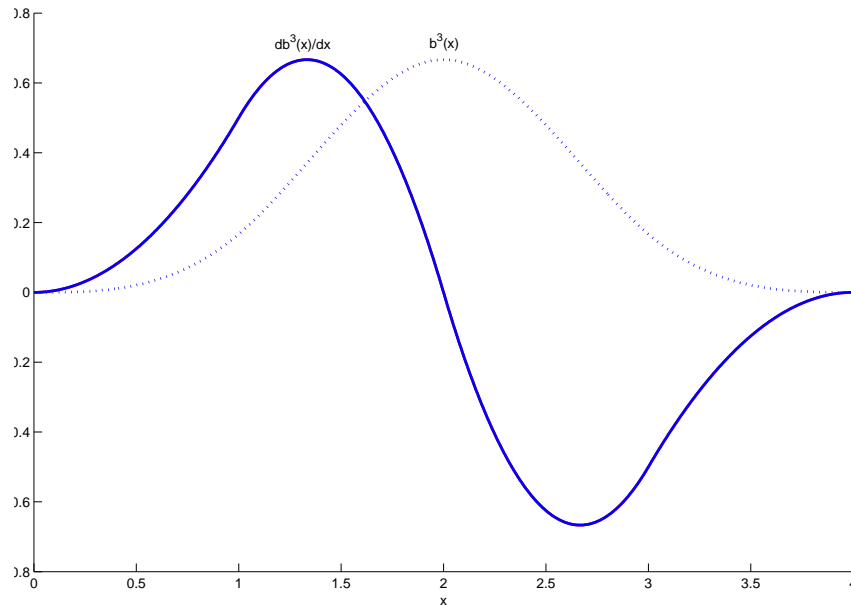


Figure 2.5. The derivative of cubic b-spline

### 2.5.2. Scalar and Tensor Products of B-splines

The integrals of b-splines can be computed easily with the aid of convolution. The convolution of two b-splines of degree  $n_1$  and  $n_2$  is defined as [10]:

$$b^{n_1+n_2+1}(x) = \int_R b^{n_1}(x-y)b^{n_2}(y)dy \quad (2.39)$$

The other significant properties of b-splines are the representation of their scalar product. The scalar product of two b-splines and their derivatives can be shown as:

$$s_{i-k}^n = b_{i,h}^n \cdot b_{k,h}^n = hb^{2n+1}(n+1+i-k) \quad (2.40)$$

$$d_{i-k}^m = \frac{1}{h} (2s_{i-k}^{n-1} - s_{i-k-1}^{n-1} - s_{i-k+1}^{n-1}) \quad (2.41)$$

The tensor product of b-splines helps to construct b-splines in two and three

dimensions. It is defined by multiplying b-splines of each direction. The tensor product of b-splines of degree  $n$  with support  $[i, i + n]h$ , grid index  $i$ , and dimension  $m$  is

$$b_{i,h}^n(x) = h^{-m/2} \prod_{d=1}^m b_{i_d,h}^n(x_d) \quad i \in Z^m, x \in R^m \tag{2.42}$$

Figure 2.6 and Figure 2.7 show the tensor product cubic b-spline for two and three dimensions with their first order partial derivatives with respect to  $x$ , respectively.

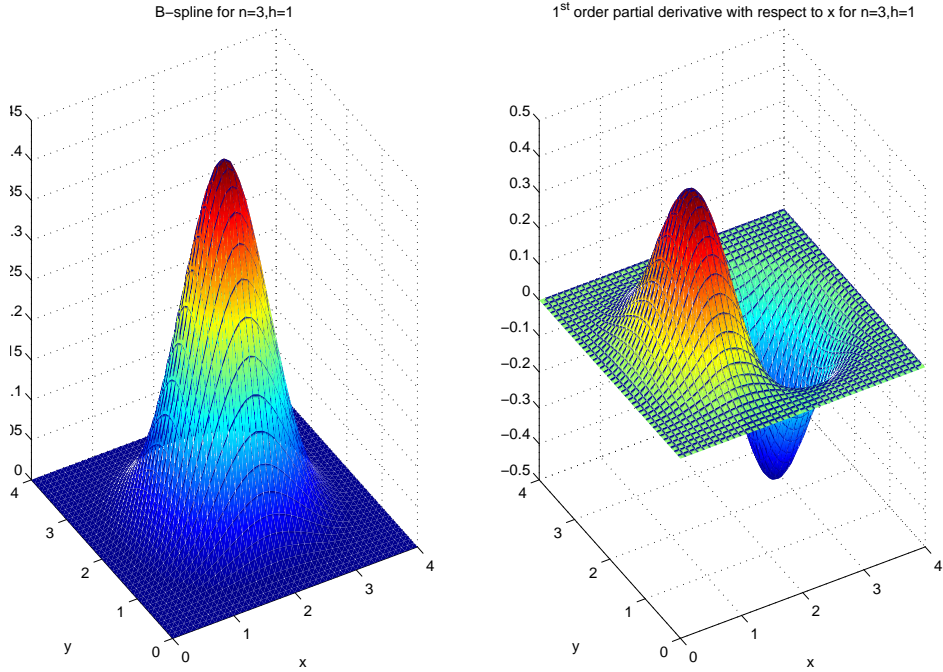


Figure 2.6. Tensor product of cubic b-spline in 2D and first order partial derivative of cubic b-spline with respect to  $x$

**2.5.3. Error Analysis**

The error in finite element approximation is defined as the difference between the exact ( $u_e$ ) and the approximated solution:

$$e = u_e - \tilde{u} \tag{2.43}$$

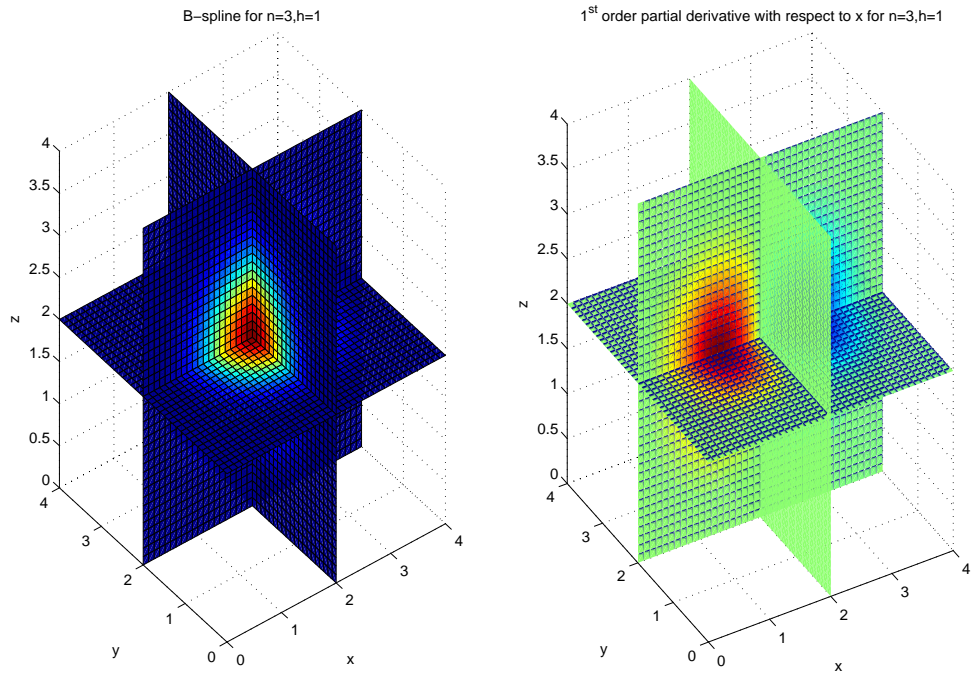


Figure 2.7. Tensor product of cubic b-spline in 3D and first order partial derivative of cubic b-spline with respect to  $x$

For the accuracy studies, the maximum norm measures the maximum absolute value, the relative error measures the absolute value of error divided by the exact value, and relative  $L_2$ -error norm measures the root mean square of integral of a squared error function over the domain ( $\Omega$ ) respectively as:

$$\|e\|_{\infty} = \max|e| \quad (2.44)$$

$$\|e_{rel}\| = \left| \frac{e}{u_e} \right| \quad (2.45)$$

$$L_2 = \|e_{rel}\|_0 = \frac{\sqrt{\int_{\Omega} e^2 d\Omega}}{\sqrt{\int_{\Omega} u_e^2 d\Omega}} \quad (2.46)$$

The convergence rate is significant in order to understand the strength of method

for the numerical computation. It shows how the error reduces when the grid size is divided by two. The grid width is divided by two and taking the logarithms of error ratio with respect to base two gives the convergence rate, which is defined as

$$\text{Convergence rate} = \log_2 \frac{\|e_{h \cdot 2^{1-l}}\|}{\|e_{h \cdot 2^{-l}}\|} \quad (2.47)$$

for the grid widths  $h \cdot 2^{-l}$ ,  $l = 1, 2, 3, 4, \dots$

### 3. FEM WITH B-SPLINES

The use of b-splines as finite element basis functions is very functional with geometric modeling and numerical simulation closely linked in engineering applications. However, at first sight this seems infeasible for two reasons. Firstly, there are some difficulties in modeling essential boundary conditions. For instance, if a linear combination of b-splines is required to vanish on the boundary of the domain, then all coefficients of b-splines with support intersecting the boundary must be zero. Hence, this results in very poor approximation order for solutions of differential equations with Dirichlet boundary conditions. This difficulty can be overcome by modeling homogeneous essential boundary conditions via weight functions. Thus, solutions which vanish on the boundary are approximated with linear combinations of weighted b-splines. Secondly, the restricted b-spline is not uniformly stable due to the outer b-splines having very small support in the domain. This leads to excessively large condition numbers of finite element systems and can cause extremely slow convergence of iterative methods. The stability problem is resolved by adjoining the outer b-splines to the inner b-splines in order to form the extended b-splines having stable basis.

Combining the above ideas gives rise to the definition of weighted extended b-splines. These basis functions possess the usual properties of standard finite elements. FEM applications use basis functions, and meshes. But mesh generation causes consumption in computation duration for higher dimensions. Given the difficulty of constructing finite element meshes [24, 26, 27, 28], not being required the mesh generation is the most important advantage of using the b-splines. In addition, the use of web-splines reduces the dimension of finite element systems, in particular, when high accuracy is required [10], [29-34].

#### 3.1. Flow Chart

The flow chart of FEM using Web-method is focused. Figure 3.1 shows the flow diagram. First of all, the simulation region and the problem are defined by the

storage of inputs for the region, PDE, and boundary conditions. Then the generation of the grid cells and classification of b-splines are done for the simulation region. The next step is to compute the extension coefficients. If there is homogeneous Dirichlet boundary condition, the weight function for the region is determined. After assembling the system of equations, the approximate solution is computed. At the end, the results are shown as an output.

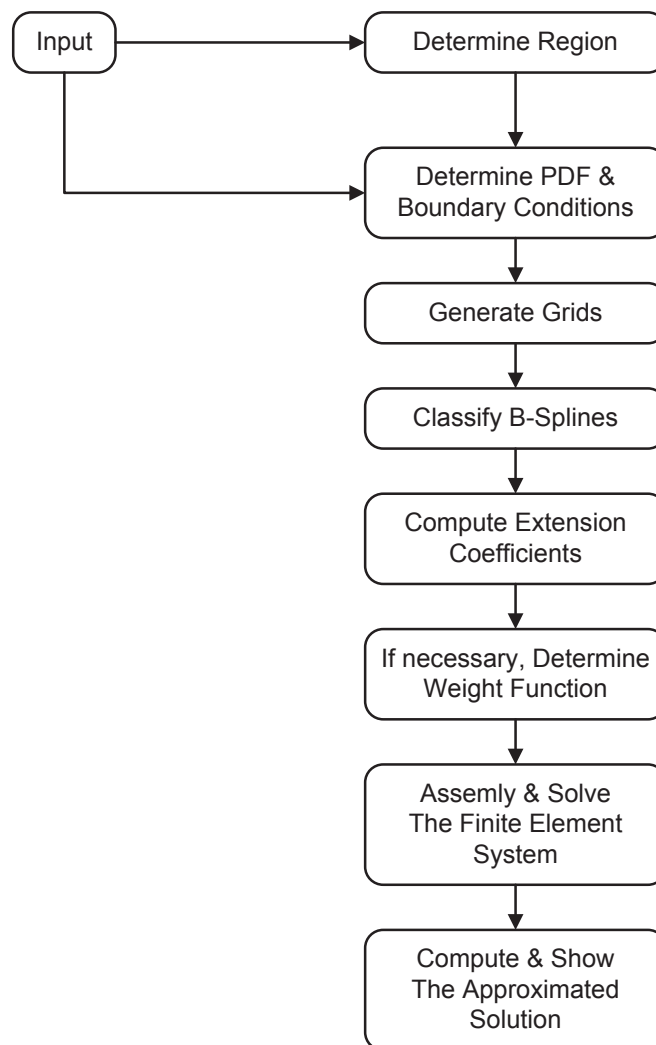


Figure 3.1. The flow diagram of FEM with web-method

### 3.2. Classification of b-splines

There are two types of b-splines; the inner and outer b-splines, which depend on the size of their support in the domain. The outer b-splines are adjoined to the inner b-splines to eliminate instability.

For the domain  $\Omega$ , firstly grid generation is completed. Figure 3.2 shows the projection view of the layers for sphere region with all layers of the grid generation. The grid width is taken as 0.25. The next step is to classify b-splines. The relevant b-splines, which are supporting in the domain, are determined. According to the size of their support, they are classified as inner and outer b-splines. The inner b-splines have at least one complete grid cell of their support in the domain. The other ones supporting the domain are called outer b-splines [10], [29] - [34]. For the outer b-splines, the grid cells of their supports are not completely contained in the boundary.

Figure 3.3, Figure 3.4 and Figure 3.5 show the inner and outer linear, quadratic and cubic b-splines for one layer with the grid width 0.25. According to their center of supports, the inner and outer b-splines are marked by  $(\bullet)$  and  $(\circ)$ , respectively. Three layers and all relevant b-splines of the sphere are depicted in Figure 3.6 and Figure 3.7.

### 3.3. Extension Coefficients

The relevant b-splines supporting in the domain are classified as inner and outer b-splines. The inner b-splines  $(b_k, k \in I)$  have at least one complete grid cell of their support in the domain. The others are outer b-splines  $(b_i \in J(k))$ . For the outer b-splines, the grid cells of their supports are not entirely contained in the domain. Although the outer b-splines have small effect, they must be taken into consideration for stability. So they are adjoined to the closest inner b-splines to form the extended

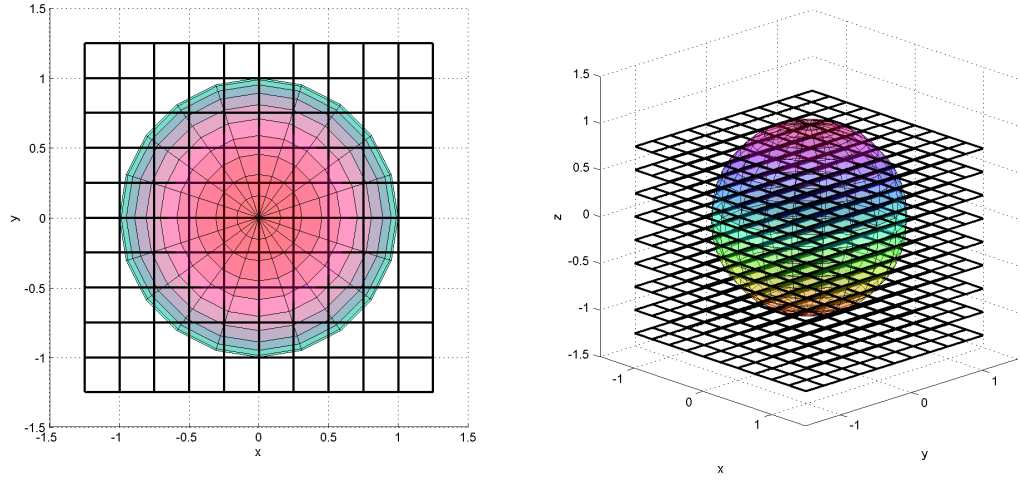


Figure 3.2. The projection view of layers and all layers of the sphere

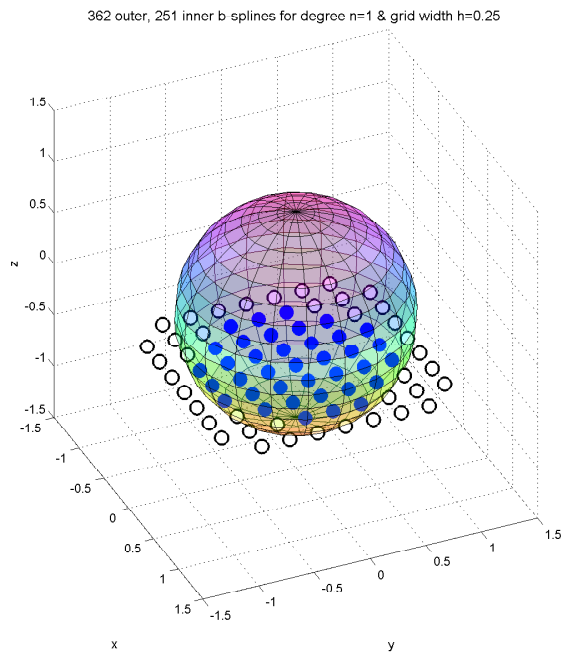


Figure 3.3. Outer and inner b-splines for degree n=1

b-splines  $B_k$ .

$$B_k = b_k + \sum_i e_{k,i} b_i \quad \text{for } k \in I, i \in J(k) \quad (3.1)$$

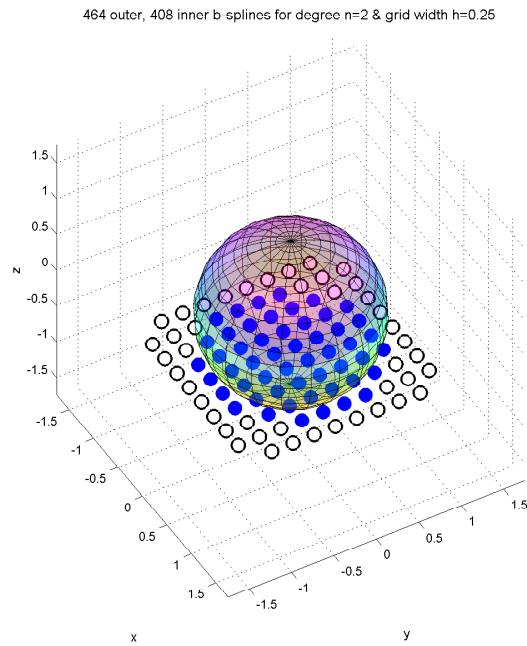


Figure 3.4. Outer and inner b-splines for degree  $n=2$

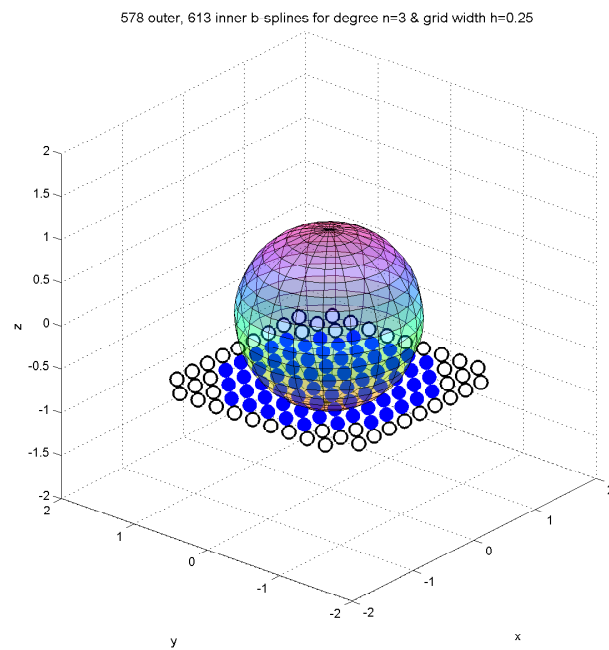


Figure 3.5. Outer and inner b-splines for degree  $n=3$

where  $e_{k,i}$  are the extension coefficients. These extended b-splines inherit all basic features of the standard b-splines  $b_k$ . The extension coefficients are computed by using Lagrange polynomials as:

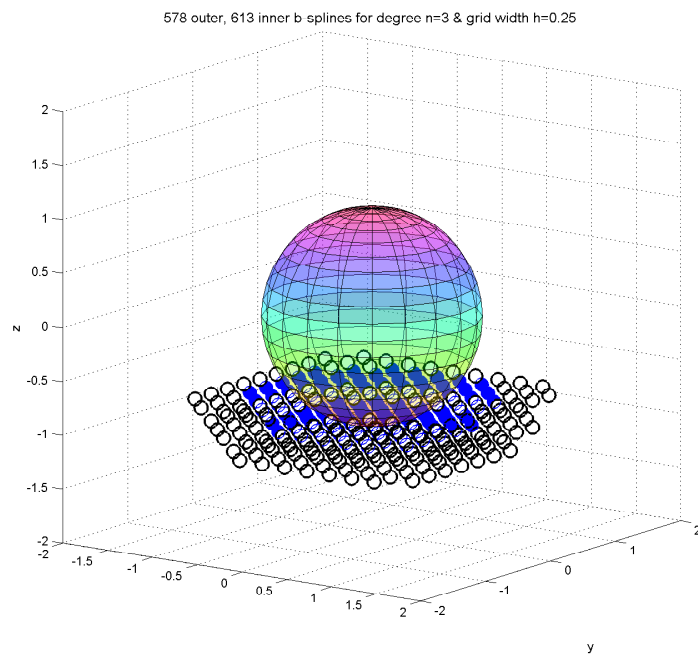


Figure 3.6. Outer and inner b-splines for degree  $n=3$  for three layers of sphere domain

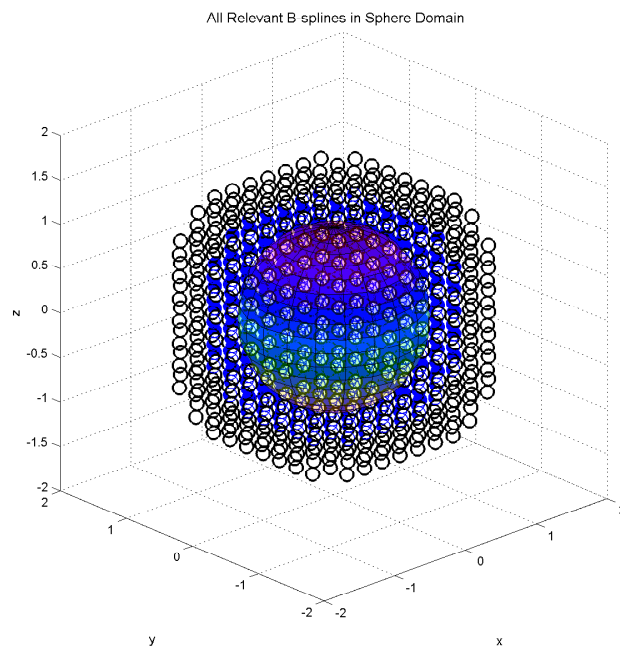


Figure 3.7. All relevant outer and inner b-splines for degree  $n=3$

$$e_{k,i} = \begin{cases} \prod_{d=1}^m \prod_{\mu=0}^n \frac{i_d - l_d - \mu}{k_d - l_d - \mu}, & \text{for } i = j \in J, k \in I(i), l_d + \mu \neq i_d \\ 1, & \text{for } i = k \in I \\ 0, & \text{otherwise} \end{cases} \quad (3.2)$$

where  $l = [l_1, l_2, \dots] \in Z_m$  is the index for the lower left position of  $I(j)$ . 3D extension coefficients for linear, quadratic and cubic b-splines are calculated by Lagrange polynomials and given in Table 3.1.

### 3.4. The Weight Function

The weight function is a continuous positive function in the domain and zero on the boundary. It can be constructed by using smooth distance function as [35, 36, 37]:

$$w(x) = \begin{cases} 1 - \left(1 - \frac{\text{dist}(x, \partial\Omega)}{\delta}\right)^\gamma & \text{dist}(x) < \delta \\ 1 & \text{otherwise} \end{cases} \quad (3.3)$$

where  $\delta$  is the boundary strip,  $\gamma$  is the smoothing parameter, and  $\text{dist}$  is the function which determines the minimum distance to the boundary.

If analytical equations are used for the boundaries, the weight function can be constructed by using Rvachev's R-functions. The intersection, union, or complement of R-functions can be considered as [35, 36, 37]:

$$w_\cap(w_1, w_2) = \frac{1}{1 + \tau} \left( w_1 + w_2 - \sqrt{w_1^2 + w_2^2 - 2\tau w_1 w_2} \right) \quad (3.4)$$

$$w_\cup(w_1, w_2) = \frac{1}{1 + \tau} \left( w_1 + w_2 + \sqrt{w_1^2 + w_2^2 - 2\tau w_1 w_2} \right) \quad (3.5)$$

$$w^c = -w \quad (3.6)$$

Table 3.1. 3D extension coefficients

Degree (n)	Corner Extension Coefficients
<b>1</b>	<b>1. Layer</b> 8 -4 -4 2 <b>2. Layer</b> -4 2 2 -1
<b>2</b>	<b>1. Layer</b> 27 -27 9 -27 27 -9 9 -9 3 <b>2. Layer</b> 27 -27 9 -27 27 -9 9 -9 3 <b>3. Layer</b> 9 -9 3 -9 9 -3 3 -3 1
<b>3</b>	<b>1. Layer</b> 64 -96 64 -16 -96 144 -96 24 64 -96 64 -16 -16 24 -16 4 <b>2. Layer</b> -96 144 -96 24 144 -216 144 -36 -96 144 -96 24 24 -36 24 -6 <b>3. Layer</b> 64 -96 64 -16 -96 144 -96 24 64 -96 64 -16 -16 24 -16 4 <b>4. Layer</b> -16 24 -16 4 24 -36 24 -6 -16 24 -16 4 4 -6 4 -1

respectively where  $\tau$  is a constant ( $-1 < \tau \leq 1$ ). Taking  $\tau = 0$  provides good results in simulations. The examples of weight functions are tabulated in Table 3.2 and plotted in Figure 3.8. Figure 3.9 shows the constructed weight functions for the given domains using Rvachev's R-functions.

Table 3.2. The weight functions and rule for the 3D domain

Functions	$w_1 = 25 - (x + 1)^2 - (y + 5)^2 - (z - 7)^2$ $w_2 = 12 - (x + 3)^2 - (y - 1)^2 - z^2$ $w_3 = 6 - (x + 1)^2 - (y - 5)^2 - z^2$ $w_4 = 20 - (x - 2)^2 - (y - 3)^2 - (z - 4)^2$ $w_5 = 8 - (x - 2)^2 - (y - 3)^2 - (z - 7)^2$
Rule	$\Omega_R = (\Omega_1 \cup \Omega_2) \cap \overline{\Omega_3} \cup \Omega_4 \cap \overline{\Omega_5}$

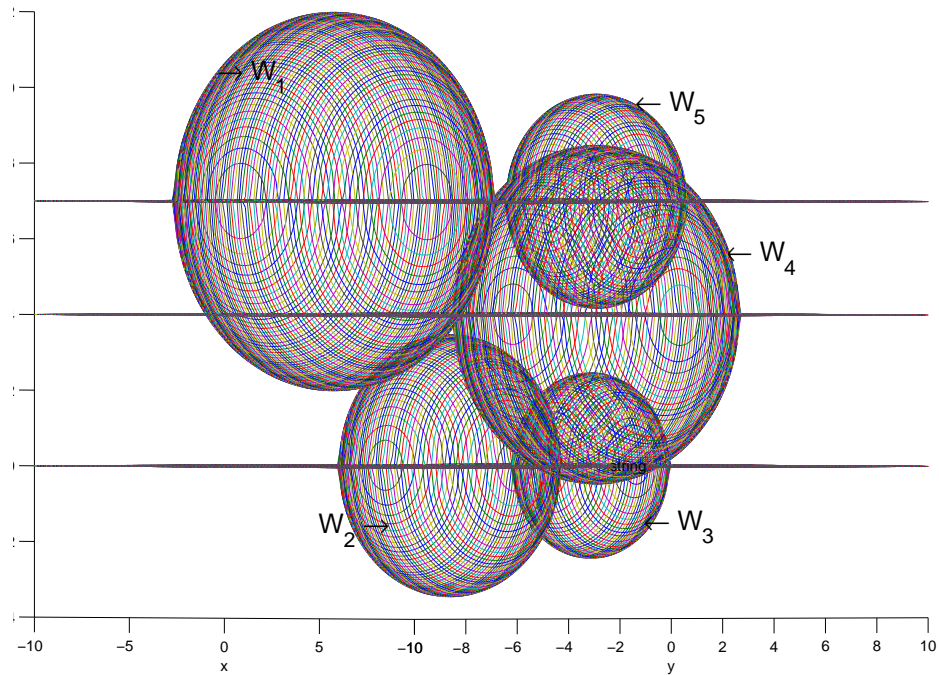


Figure 3.8. The weight functions

### 3.5. Weighted Extended B-splines

The extended b-splines are multiplied by the weight function  $w(x)$  if the Dirichlet boundary conditions are taken into consideration. Weight function is a continuous positive function in the domain, and zero on the boundary. It can be constructed by using analytical function, distance function or Rvachev's R-function. As a result, the web-splines are obtained as:

$$B_k = \frac{w(x)}{w(x_k)} \left( b_k + \sum_i e_{k,i} b_i \right) \quad \text{for } k \in I, i \in J(k) \quad (3.7)$$

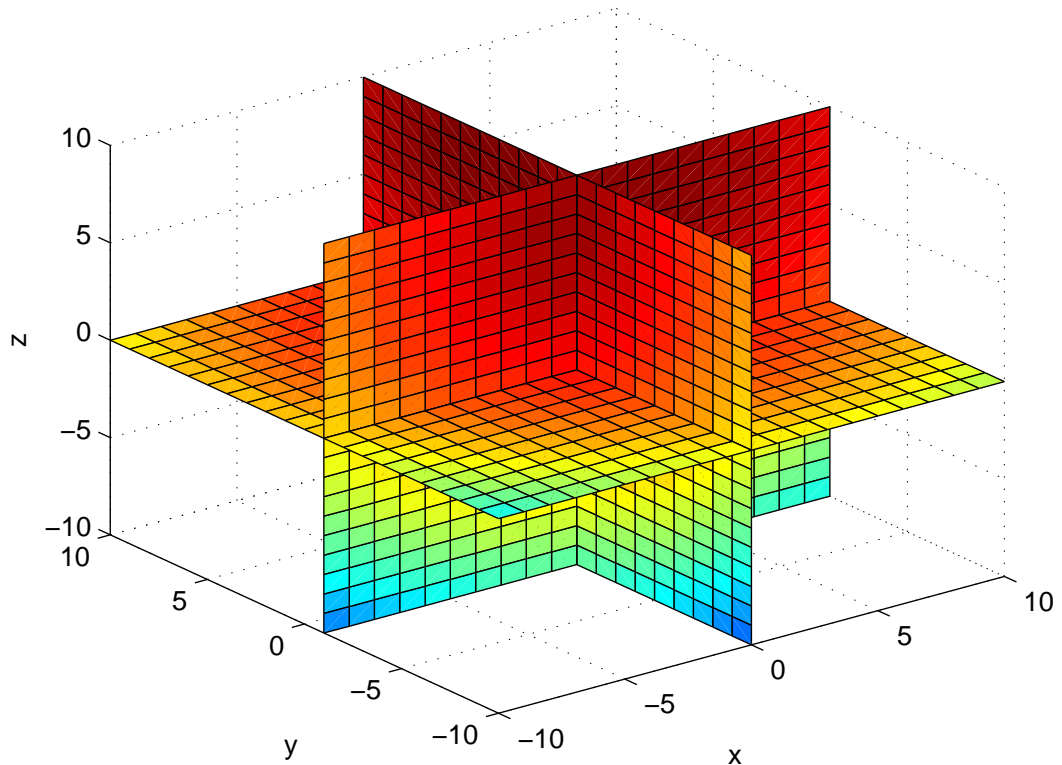


Figure 3.9. The weight function using Rvachev's R-function

where  $x_k$  is in the center of a grid cell which intersects the support of b-spline and the domain completely for normalization,  $w(x)$  is the weight function for  $x \in R^m$  and  $w(x_k)$  is the value of weight function at the center of grid cell.

The significance of web-splines is that the contribution of basis functions which are near the boundary is added to the inner basis functions. So the number of nodes and computing time is reduced. Secondly instability problem can be solved by coupling the outer b-splines with the inner b-splines. If we have a boundary value problem with homogeneous Dirichlet boundary conditions, Equation (3.7) is constructed as a basis function into Equation (2.33). The other boundary conditions use the Equation (3.1) as basis function.

## 4. WEB-SPLINE APPLICATIONS FOR ONE AND TWO DIMENSIONS

### 4.1. One Dimensional EM Problems

The applications of one dimensional electromagnetic problems using FEM with b-splines are given in [12]. The main formula that is being used in one dimension problems is listed below:

The standard uniform b-spline  $b^n$  of degree  $n$  for one dimension is defined by the recursion [10] as:

$$b^n(x) = \int_0^1 b^{n-1}(x-t)dt \quad (4.1)$$

starting from  $b^0$  of the unit interval between zero and one.

The tensor product b-splines for one dimension is

$$b_k^n(x) = h^{-0.5}b^n(x/h - k) \quad (4.2)$$

The extension coefficients,  $e_{i,k}$ , using Lagrange polynomials is same as Equation (3.2). Weight function for one dimension is:

$$w = (x^e - x)(x - x^i) \quad (4.3)$$

where  $x^e$  and  $x^i$  are the beginning and the end points of boundary of the problem, respectively.

### 4.1.1. Electromagnetic Waves Between Parallel Plates

One of the other examples of electromagnetic problems in one dimension is to find the electromagnetic waves between parallel plates, shown in Figure 4.1.

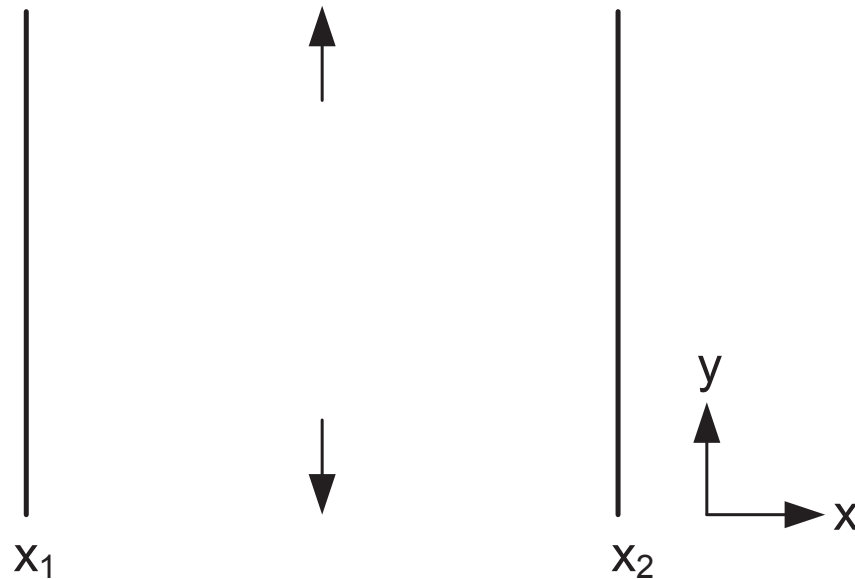


Figure 4.1. Parallel plates

Consider the parallel plate waveguide; the general differential equation is given as [25]:

$$\frac{d}{dx} \left( \frac{1}{\mu_r} \frac{d}{dx} E_y \right) + \tilde{k}_0^2 \varepsilon_r E_y = f(x) \quad (4.4)$$

where  $E_y$  is the electric field between plates, with relative permittivity  $\varepsilon_r$ , relative permeability  $\mu_r$ , wave number  $\tilde{k}_0$ , and  $f(x)$  is the source function.

This application uses the parameters;  $\mu_r = -1$ ,  $\tilde{k}_0^2 \varepsilon_r = \pi^2$ ,  $f(x) = 2\pi^2 \sin(\pi x)$  with the homogeneous Dirichlet boundary conditions  $E_y(0) = E_y(1) = 0$  in order to obtain the results using FEM with web-splines. The exact solution is found as  $E_y(x) = \sin(\pi x)$ .

The simulations are compared with the standard FEM, which uses linear Lagrange polynomial basis functions. As seen in Figure 4.2, by using web-splines basis functions, more accurate results are obtained with respect to the standard FEM analysis.

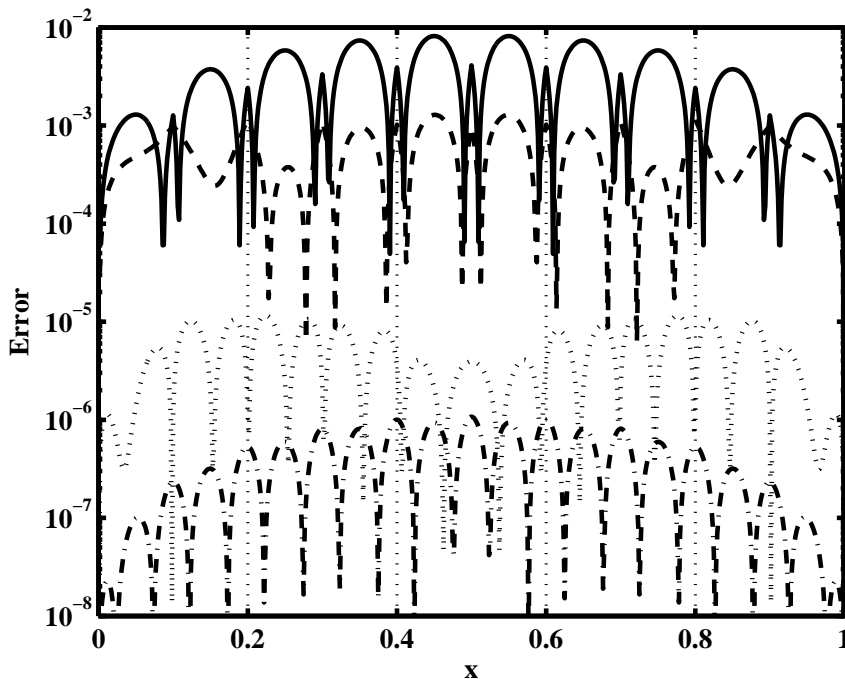


Figure 4.2. Error analysis of parallel plates using standard FEM (solid) and linear (dash), quadratic (dot), and cubic (dash-dot) web-splines

#### 4.2. Two Dimensional EM Problems

The applications of two dimensional electromagnetic problems using FEM with b-splines are given in [13]. The tensor product b-splines help to construct b-splines in two dimensions. It is defined by multiplying b-splines of each direction [10]. The tensor product b-splines  $b_k^n(x, y)$  for  $x, y \in R^m$  is

$$b_k^n(x) = h^{-1}b^n(x/h - k)b^n(y/h - k) \quad (4.5)$$

where  $h$  is the grid width,  $n$  is the degree,  $k = [k_1, k_2, \dots]$  is the grid index. The support of each b-spline consists of  $(n + 1)^m$  grid cells  $(kh + [0, h]^m)$ . The b-splines are positive on their supports, and  $n - 1$  times continuously differentiable.

### 4.2.1. Wave Equation Analysis For Circular Domain

In this section, for the two dimensional wave equation analysis, the circular domain is chosen in order to compare with the exact results. Considering the wave equation with Cauchy boundary conditions, the solution of the wave equation for circular domain is obtained by using linear, quadratic, and cubic extended b-splines. Boundary conditions for circle is given at Equation (2.26) for  $\alpha = 1, \gamma = \tilde{j}k$  and  $q(x, y)$  is as Equation (4.6) where  $\theta$  shows the direction angle of wave. According to the wave equation for circular domain, the web-spline method is compared with the standard FEM by using the exact solution given in Equation (4.7).

$$q(x, y) = \begin{cases} \tilde{j}k(1 - \sin \theta)e^{j\tilde{k}(\cos \theta x + \sin \theta y_1)} & \text{on } \Gamma_1 \\ \tilde{j}k(1 + \cos \theta)e^{j\tilde{k}(\cos \theta x_2 + \sin \theta y)} & \text{on } \Gamma_2 \\ \tilde{j}k(1 + \sin \theta)e^{j\tilde{k}(\cos \theta x + \sin \theta y_2)} & \text{on } \Gamma_3 \\ \tilde{j}k(1 - \cos \theta)e^{j\tilde{k}(\cos \theta x_1 + \sin \theta y)} & \text{on } \Gamma_4 \end{cases} \quad (4.6)$$

$$\phi(x, y) = e^{j\tilde{k}(\cos \theta x + \sin \theta y)} \quad (4.7)$$

Figure 4.3 shows triangulation for the circular domain using 549 nodes and 1032 triangles. Figure 4.4 shows the b-spline basis of the same domain using 68 outer, 148 extended inner, and 76 standard inner quadratic b-splines.

The error analysis shows better approximation when web-splines are used as basis functions. Figure 4.5 shows the relative  $L_2$  error norm versus number of nodes with the standard FEM and the linear, quadratic, and cubic extended b-splines. According to figure, more accurate results are obtained by using web-splines with fewer basis functions instead of standard finite elements.

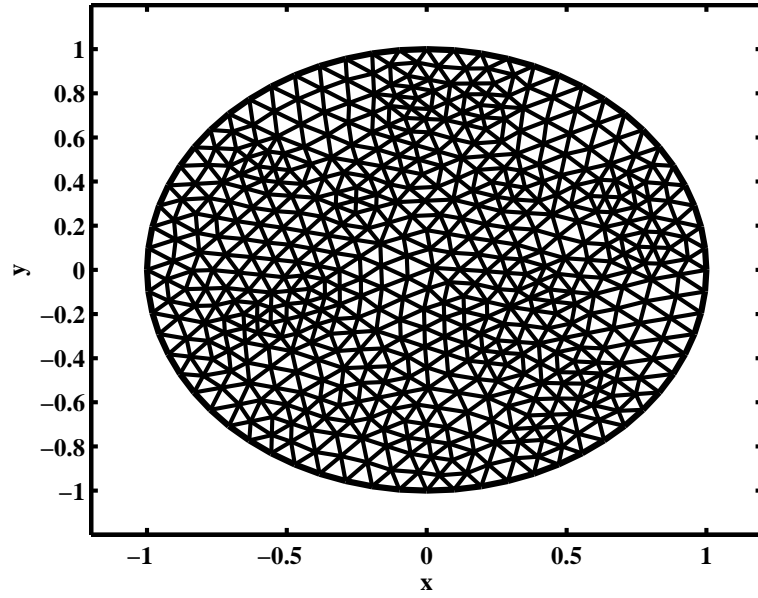


Figure 4.3. Triangulation for circular domain

68 outer, 148 extended inner & 76 standard inner b-splines for  $n=2$  &  $h=0.125$

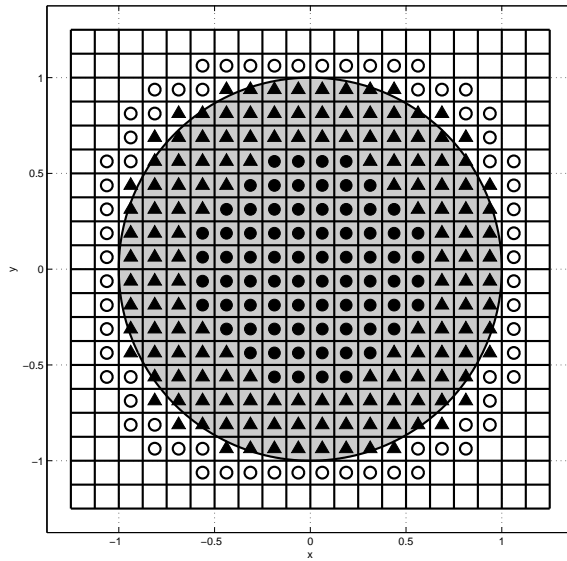


Figure 4.4. Quadratic extended b-splines for circular domain

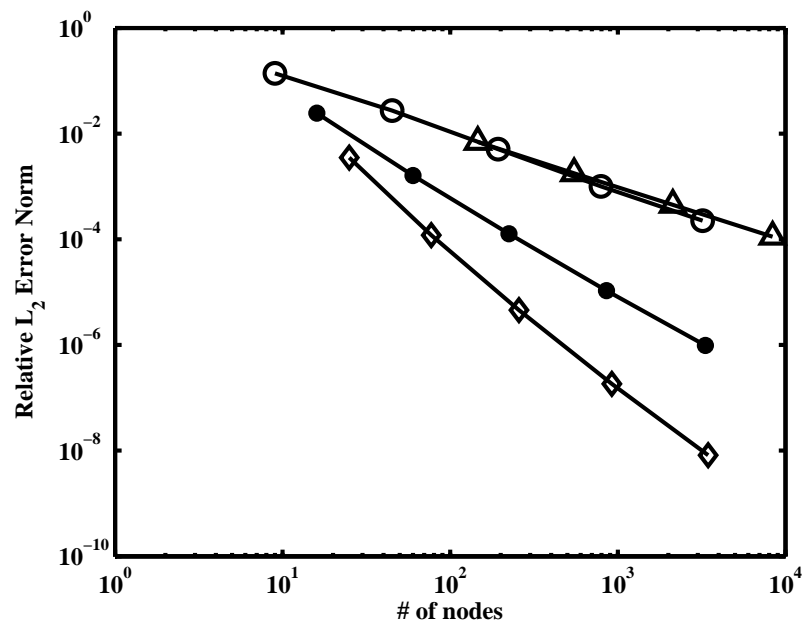


Figure 4.5. The relative  $L_2$  error norm for various basis functions which are linear Lagrange polynomial ( $\Delta$ ), linear ( $\circ$ ), quadratic ( $\bullet$ ), and cubic ( $\diamond$ ) extended b-splines versus the number of nodes for circular domain

## 5. RADIALY SYMMETRIC WEIGHTED EXTENDED B-SPLINE MODEL

In this section, besides using the web-spline method for axisymmetric formulations of electrostatic and EM wave problems, Thus, with the existence of symmetry, a number of physically important two and 3D problems can be solved by using one and two dimensional elements. FEM with web spline applications is given in Chapter 4 for one dimensional (1D) and 2D EM problems for homogeneous boundary conditions in Cartesian coordinates.

The rest of this paper proceeds as follows. The formulation of the web-splines in cylindrical coordinates is introduced in Section 5.1, and in addition the web-spline method including the grid cell classification on the domain, weight functions and numerical integrations is given in detail. Section 5.2 is dedicated to the FEM with web-splines model of the problems derived from the classical heat diffusion equation. The corresponding variational functions of each problem are presented along with the error analysis definitions. Section 5.3 presents the numerical results of electrostatic problems, and electromagnetic wave equation using various web-splines with different grid widths, which are followed by the simulation results. It is shown that by using the web-splines basis functions, more accurate results are obtained with respect to the standard FEM analysis.

### 5.1. Web-spline in cylindrical coordinate

The tensor product b-splines used in cylindrical coordinate is defined by multiplying b-splines of each direction [10]. The tensor product b-splines  $b_k^n(r)$  for  $r \in R^2$  is

$$b_k^n(r) = h^{(-1/2)} b^n(r/h - k) \tag{5.1}$$

where  $h$  is the grid width,  $n$  is the degree,  $k = [k_1, k_2] \in Z^2$  is the grid index. The support of each b-spline consists of  $(n + 1)^2$  grid cells  $(kh + [0, h]^2)$ . The b-splines are positive on their supports, and  $n - 1$  times continuously differentiable.

The polynomial representations of linear, quadratic and cubic b-splines used in cylindrical coordinates are tabulated in Table 5.1.

Table 5.1. Spline functions used in cylindrical coordinates

Type	Representation
Linear (n=1)	$r$
$b_1^1(r)$	$-r + 1$
Quadratic (n=2)	$1/2r^2 - r + 1/2$
$b_1^2(r)$	$-r^2 + r + 1/2$
	$1/2r^2$
Cubic (n=3)	$-1/6r^3 + 1/2r^2 - 1/2r + 1/6$
$b_1^3(r)$	$1/2r^3 - r^2 + 2/3$
	$-1/2r^3 + 1/2r^2 + 1/2r + 1/6$
	$1/6r^3$

The relevant b-splines ( $b_k, k \in K$ ) supporting in the domain are classified as inner and outer b-splines. The inner b-splines ( $b_i, i \in I$ ) have at least one complete grid cell of their support in the domain. The others are outer b-splines ( $b_j, j \in J$ ). For the outer b-splines, the grid cells of their supports are not entirely contained in the domain. Although the outer b-splines have small effect, they must be taken into consideration for stability. So, they are adjoined to the closest inner b-splines in order to form the extended b-splines,  $B_i^{eb}$  [10].

$B_i^{eb}$  can be used to solve boundary value problem with the Neumann boundary conditions. If the Dirichlet boundary conditions are taken into consideration, the extended b-splines are multiplied by the weight function  $w(r)$ , which is a continuous positive function in the domain, and zero on the boundary. It can be constructed by using analytical function, distance function or Rvachev's R-function which is shown in

Figure 5.1 [37]. As a result, the web-splines are obtained as:

$$B_i^{web} = \frac{w(r)}{w(r_i)} \left( b_i + \sum_j e_{i,j} b_j \right) = w B_i^{eb} \quad (5.2)$$

where  $r_i$  is in the center of a grid cell which intersects the support of b-spline and the domain completely for normalization,  $e_{i,j}$  is the extended coefficient,  $w(r)$  is the weight function for  $r \in R^2$ , and  $w(r_i)$  is the value of weight function at the center of grid cell. According to the center of their supports, Figure 5.2 shows the standard ( $\bullet$ ), extended inner ( $\blacktriangle$ ), and outer ( $\circ$ ) quadratic b-splines respectively for the coaxial cable.

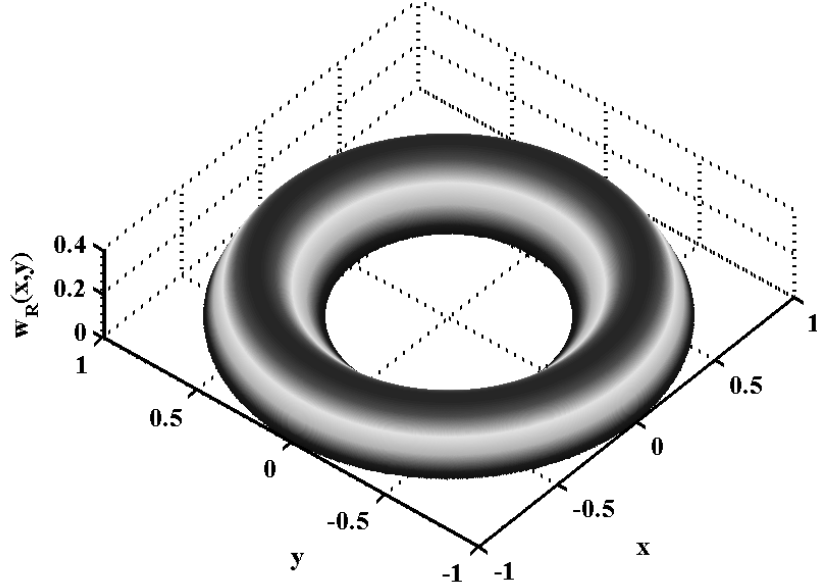


Figure 5.1. The weight function

Until this time, web-splines have been applied only to homogeneous dirichlet boundary conditions. This study extends the applications for inhomogeneous dirichlet boundary conditions. Thus, the weight function plays an important role in the performance of the FEM with web-splines method. It can impose a tremendous influence on the accuracy of the solutions, the complexity of computation and the rate of convergence. To satisfy all given boundary conditions exactly, the R-Function Method (RFM) solution structure is developed for weight function [37]. The solution structure

96 outer, 256 extended inner, 76 standard inner b-splines for n=2, h=0.1

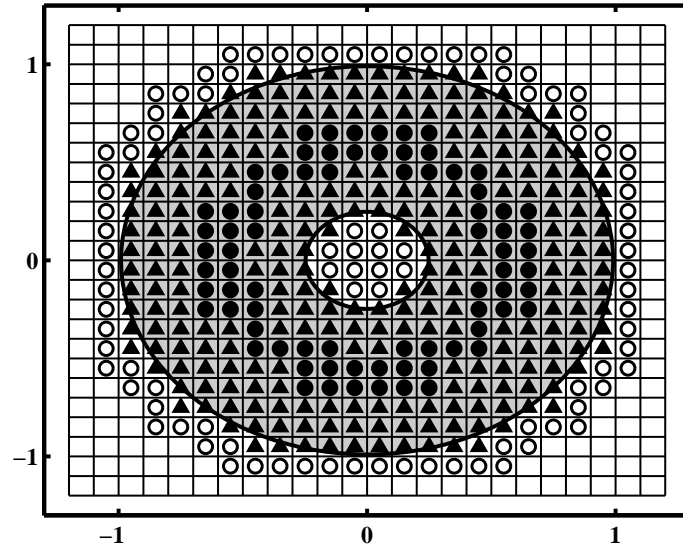


Figure 5.2. The standard (●), extended inner (▲) and outer (○) web-splines for coaxial cable

( $u$ ) for inhomogeneous conditions is

$$u = w \sum_{i=1}^n C_i \chi_i + \varphi \quad (5.3)$$

where  $w : R^n \rightarrow R$  is a known as the weight function,  $C_i$  are scalar coefficients and  $\chi_i$  are some basis functions. Using the transfinite Lagrangian interpolation  $\varphi$ ,

$$\varphi = \frac{\sum_{i=1}^m \varphi_i \sum_{j=1, j \neq i}^m \omega_j}{\sum_{i=1}^m \sum_{j=1, j \neq i}^m \omega_j} \quad (5.4)$$

(5.3) places no restrictions on form, shape, or dimension of the sets  $\omega_i = 0$  [37].

## 5.2. FEM with web-spline

In EMs, most differential equations with the mixed boundary condition in the domain  $\Omega$  can be considered as

$$A \nabla^2 u + \alpha u = f \quad \text{in } \Omega \quad (5.5)$$

$$ru = 0 \quad \text{on} \quad \partial\Omega_1 \quad (5.6)$$

$$s \frac{\partial u}{\partial n} + ru = g \quad \text{on} \quad \partial\Omega_2 \quad (5.7)$$

where  $\partial\Omega_1, \partial\Omega_2$  show the homogeneous Dirichlet ( $g = 0$ ) and Cauchy boundaries around the domain respectively. The corresponding variational function is:

$$J(u) = \frac{1}{2} \int_V [A \nabla^2 u + \alpha u^2] dV + \int_{\Omega_2} \left( \frac{r}{2} u^2 - gu \right) d\Omega_2 - \int_V f u dV \quad (5.8)$$

In FEM analysis, the approximated solution  $u^h$  consisting of  $p$  nodes is,

$$u^h = \int_{i=1}^p c_i B_i \quad (5.9)$$

where  $c_i$  indicates the coefficients of basis functions  $B_i$ . Using the Ritz-Galerkin method, the problem can be formulated in terms of the unknown at the nodes.

$$J(u) = \int_{h=1}^M J^h(u^h) \quad (5.10)$$

where  $M$  denotes the total number of volume elements and  $J^h$  is given by (5.8). Taking the partial derivative of  $J^h$  with respect to  $u_i^h$ , where  $i = 1 \dots p$ ,

$$\frac{\partial J^h}{\partial u_i^h} = \int_{j=1}^p c_j \int_V [A (\nabla B_i (\nabla B_j)^t) + \alpha B_i B_j] dV + Ar \int_S B_i B_j dS - \int_V f B_j dV - A \int_S g B_j dS \quad (5.11)$$

The following notations;  $K_{i,j} = \int_V \nabla B_i (\nabla B_j)^t dV$  (the stiffness matrix),  $M_{i,j} = \int_V \alpha B_i B_j dV$  (the mass matrix),  $F_i = \int_V f B_j dV$  (the load matrix), and the other terms from the boundary conditions help to solve the equation. In inhomogeneous Dirichlet

boundary condition of the type is given as [38, 39]:

$$u(0) = \frac{\gamma_0}{\beta_0}, \quad u(l) = \frac{\gamma_1}{\beta_1} \quad (5.12)$$

In this case,  $u(0) = u_1 = \gamma_0/\beta_0$  and  $u(l) = u_N = \gamma_1/\beta_1$ , so that only  $N - 2$  unknown nodal values  $u_2, u_3, \dots, u_{N-1}$  remain. Then the solution matrix will be reduced to:

$$\begin{bmatrix} K_{22} & K_{23} & 0 & \dots & 0 & 0 \\ K_{32} & K_{33} & K_{34} & \dots & 0 & 0 \\ 0 & K_{43} & K_{44} & \dots & 0 & 0 \\ \vdots & \vdots & \vdots & \vdots & \vdots & \vdots \\ 0 & 0 & 0 & \dots & K_{N-1,N-2} & K_{N-1,N-1} \end{bmatrix} \begin{bmatrix} u_2 \\ u_3 \\ u_4 \\ \vdots \\ u_{N-1} \end{bmatrix} = \begin{bmatrix} F_2 - \frac{K_{21}\gamma_0}{\beta_0} \\ F_3 \\ F_4 \\ \vdots \\ F_{N-1} - \frac{K_{N-1,N}\gamma_1}{\beta_1} \end{bmatrix} \quad (5.13)$$

and the two auxiliary equations corresponding to nodes 1 and  $N$  are,

$$K_{11} \left( \frac{\gamma_0}{\beta_0} \right) + K_{12}u_2 = f_1^1 + \sigma(0) \quad (5.14)$$

$$K_{N,N-1}u_{N-1} + K_{NN} \left( \frac{\gamma_1}{\beta_1} \right) = f_2^{N-1} + \sigma(l) \quad (5.15)$$

A number of physically important 2D and 3D problems can be solved by using 1D and 2D elements. These problems possess symmetry about either a point or an axis. The existence of symmetry modifies the solution techniques. The major modification is the order of the element.

The governing differential equation for quasi-static field problems in cylindrical coordinates is,

$$\frac{\partial^2 V}{\partial r^2} + \frac{1}{r} \frac{\partial V}{\partial r} + \frac{1}{r^2} \frac{\partial^2 V}{\partial \phi^2} + \frac{\partial^2 V}{\partial z^2} + Q = 0 \quad (5.16)$$

with the boundary conditions

$$V = V_B \quad (5.17)$$

or

$$\frac{\partial V}{\partial r} l_r + \frac{\partial V}{\partial \phi} l_\theta + \frac{\partial V}{\partial z} l_z + hV = 0 \quad (5.18)$$

The terms associated with the z direction are deleted in the 2D problem. The statement of symmetry means that  $V \neq f(\phi)$  and  $\phi$  terms are deleted. The governing differential equation for symmetric 2D field problems is

$$\frac{\partial V^2}{\partial r^2} + \frac{1}{r} \frac{\partial V}{\partial r} + Q = 0 \quad (5.19)$$

with the boundary conditions

$$V = V_B \quad (5.20)$$

or

$$\frac{\partial V}{\partial r} l_r + hV = 0 \quad (5.21)$$

The evaluation of the element integrals in FEM is relatively easy [39]. The incremental volume  $dV$  for a unit depth or height is

$$dV = 2\pi r dr \quad (5.22)$$

where in Cartesian coordinates  $dV = dx dy dz$  in three dimensions.

The corresponding variational function used in FEM and FEM with web-spline

methods is:

$$J(V) = \int_{r_1}^{r_2} \left[ \pi r \varepsilon \left( \frac{dV}{dr} \right)^2 - 2\pi r \rho V \right] dr \quad (5.23)$$

### 5.3. Numerical results

In this section, axisymmetric electrostatic, and EM wave are solved using the web-spline method. The results are compared with the exact and FEM solutions.

#### 5.3.1. Electrostatic problems

Axisymmetric formulation of problems such as electrostatics results in a one-dimensional differential equation. The equation for the electric potential  $V(r)$  in axisymmetric cylindrical coordinates is [40]:

$$\varepsilon \frac{d^2V}{dr^2} + \frac{\varepsilon}{r} \frac{dV}{dr} + \rho = 0 \quad (5.24)$$

where the area is constant because it corresponds to the circumference of the cylindrical boundary of the problem.  $\varepsilon$  is the permittivity of the material,  $\rho$  is the charge density. (5.24) can be written in a more concise form as

$$\frac{\varepsilon}{r} \frac{d}{dr} \left( r \frac{dV}{dr} \right) + \rho = 0 \quad (5.25)$$

The exact solution of (5.25) is

$$V = -\frac{\rho r^2}{4\varepsilon} + C_1 \ln r + C_2 \quad (5.26)$$

The axisymmetric coaxial cable illustrated in Figure 5.3 is a good example which

exists in [41] to which FEM with web-spline method in cylindrical coordinates may be applied. For the purpose of discussion we assume that the coaxial cables are very large, so that  $\partial/\partial z = 0$ . The radius of the inner conductor is  $r_a = 5mm$ , the inner radius of the outer conductor is  $r_c = 25mm$ , and the interface radius is  $r_b = 10mm$ . The outer conductor is grounded, so that  $V_{r_c} = 0$ . The inner conductor is held at a fixed potential which is  $V_{r_a} = 500V$ . The interelectrode space,  $a < r < b$ , and  $b < r < c$  are filled with a linear, homogeneous, and isotropic dielectric of permittivity  $\epsilon_1 = 0.5$  and  $\epsilon_2 = 2.0$ , respectively. A charge density of  $\rho_1 = 100$  for the core and  $\rho_2 = 0$  for the outer layer are assumed. Our aim is to determine the potential distribution within the dielectric region.

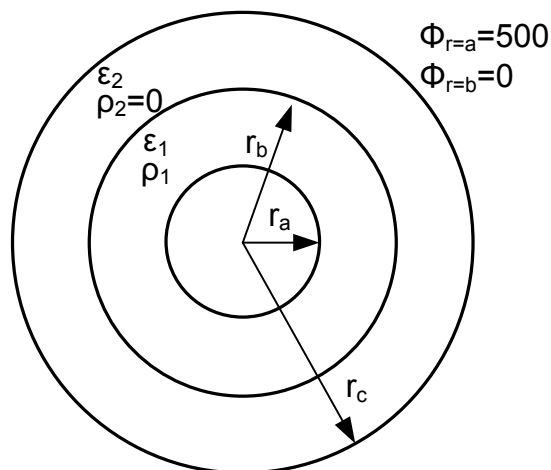


Figure 5.3. Coaxial cable

The general solutions for each cable using (5.25) are:

$$V_1 = -\frac{\rho r^2}{4\epsilon_1} + C_1 \ln r + C_2 \quad a \leq r \leq b \quad (5.27)$$

$$V_2 = -C_3 \ln r + C_4 \quad b \leq r \leq c \quad (5.28)$$

The solutions of (5.27) and (5.28) give  $C_1 = 6009.762$ ,  $C_2 = -7922.339$ ,  $C_3 = -997.560$ ,  $C_4 = 3211.021$  with the boundary conditions given.

To obtain an expression for the electric field intensity, we make use of the relation  $E = -\nabla V$  in cylindrical coordinates [41].

$$E_1 = -100r\vec{a}_r - 6009.762\frac{\vec{a}_r}{r} \quad a \leq r \leq b \quad (5.29)$$

$$E_2 = -997.560\frac{\vec{a}_r}{r} \quad b \leq r \leq c \quad (5.30)$$

The error analysis of the coaxial cable with respect to the exact solution using standard FEM, linear, quadratic and cubic web-splines for a grid width of 2.5 and for a grid width of 1.0 are illustrated in Figure 5.4 and Figure 5.5, respectively.

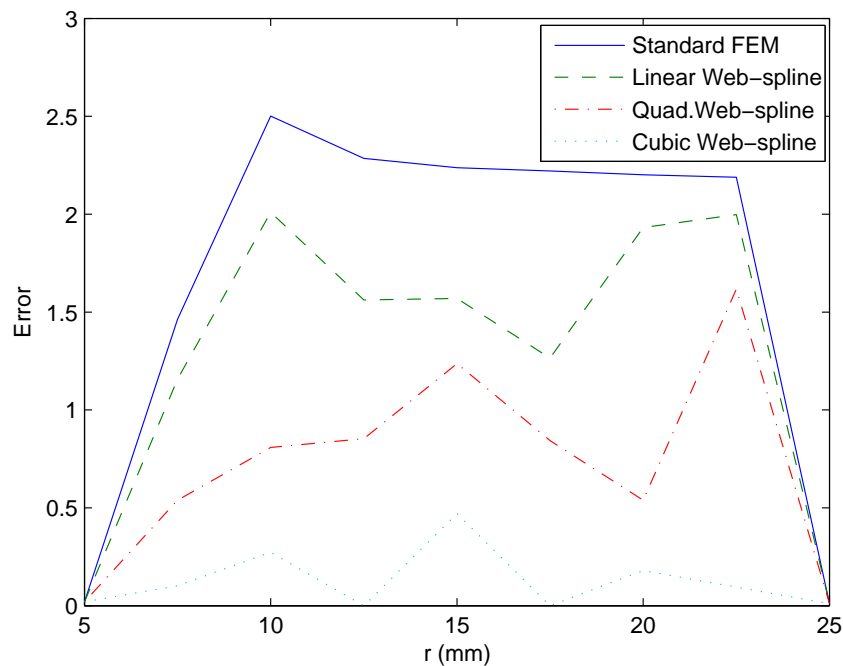


Figure 5.4. Error analysis for the coaxial cable using standard FEM, linear, quadratic, and cubic web-splines for a grid width of 2.5 mm

FEM analysis using quadratic and cubic Lagrange polynomials is not always easy to implement, whereas the implementation of higher order polynomials in web-spline method is much easier. Selection of a grid width is important for higher order polynomials. Thus, when the grid width is decreased from 2.5 (Figure 5.4) to 1.0

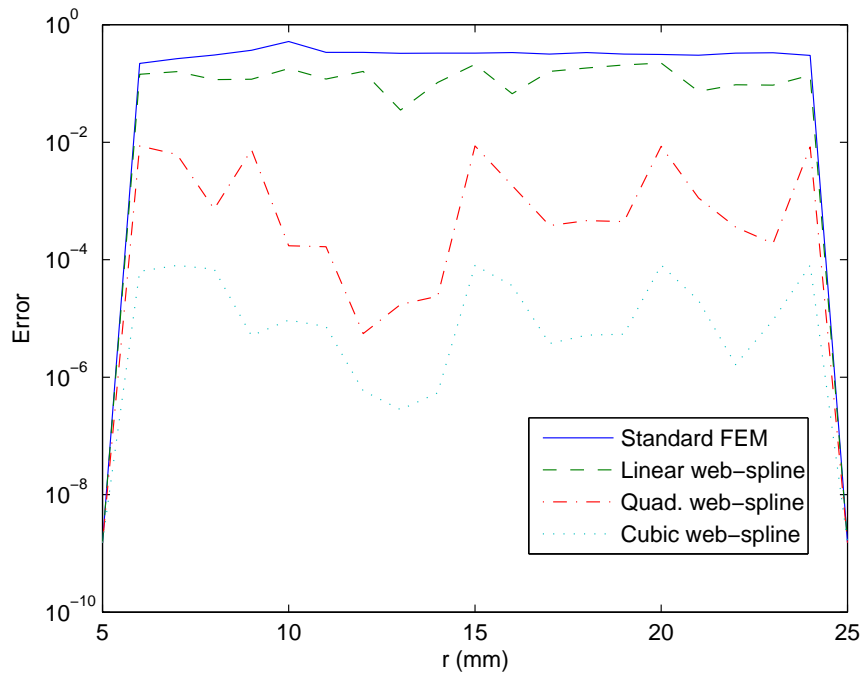


Figure 5.5. Error analysis for the coaxial cable using standard FEM, linear, quadratic, and cubic web-splines for a grid width of 1.0 mm in logarithmic scale

(Figure 5.5), the error analysis shows that our results, in comparison to the other method, gets closer to exact results.

Figure 5.6 shows the  $L_2$  error norm of computation for various basis functions which are linear Lagrange polynomial (solid), linear (dash), quadratic (dot), and cubic (dash-dot) web-splines.

### 5.3.2. The EM wave equation

In this section, the web-spline method is applied to electromagnetic wave problem in cylindrical coordinate which is illustrated in the literature [41]. All parameters are taken the same with the literature for comparisons. The axisymmetric coaxial cable with the radius of the inner conductor is considered as  $r_a = 5mm$ , and the radius of the outer conductor as  $r_c = 10mm$ . The core is assumed to be filled with plexiglass which has the permittivity of 3.4. The frequency is assumed to be 8.2 GHz. The wave

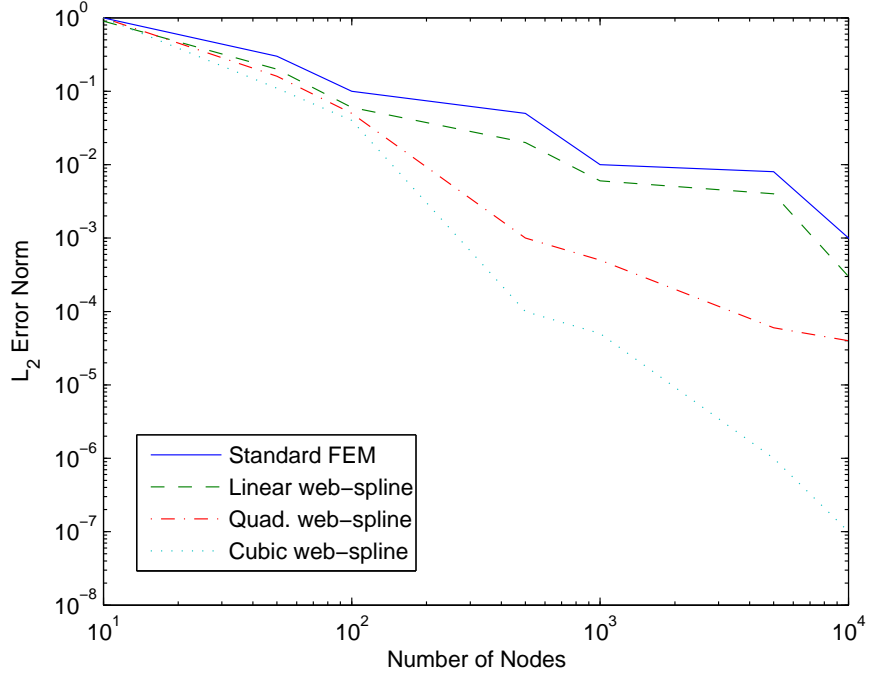


Figure 5.6. The  $L_2$  error norm of coaxial cable for various basis functions versus the number of nodes

equation in cylindrical coordinates is given as,

$$\frac{1}{r} \frac{\partial}{\partial r} \left( r \frac{\partial E_z}{\partial r} \right) + k^2 E_z = 0 \quad (5.31)$$

with inhomogeneous Dirichlet boundary conditions on the range 5 mm-10 mm as 5 mV and 0 V, respectively. Exact solution for the cylindrical wave equation is,

$$E_z = (-0.0087 - j0.0019) \frac{e^{-jkr}}{\sqrt{r}} + (-0.0087 + j0.0019) \frac{e^{jkr}}{\sqrt{r}} \quad (5.32)$$

In FEM analysis, the variational function given by (5.23) is written in terms of shape functions following the method described before and after minimizing with

respect to  $E$  appears as  $\frac{\partial J(E)}{\partial r} = 0$  which is given as:

$$\begin{aligned} \frac{\partial J(E)}{\partial r} = \int_{r_1}^{r_2} \left\{ 2\pi r \begin{bmatrix} -1/R \\ 1/R \end{bmatrix} \begin{bmatrix} -1/R & 1/R \end{bmatrix} dr \right. \\ \left. + 2\pi r \begin{bmatrix} (r_2 - r)/R \\ (r - r_1)/R \end{bmatrix} [k^2] \begin{bmatrix} (r_2 - r)/R & (r - r_1)/R \end{bmatrix} \right\} \begin{bmatrix} E_1 \\ E_2 \end{bmatrix} dr = 0 \end{aligned} \quad (5.33)$$

The shape functions are

$$N_1 = \frac{r_2 - r}{R} \quad \text{and} \quad N_2 = \frac{r - r_1}{R} \quad (5.34)$$

where  $R = r_2 - r_1$ , the length of a radial element. As the radius increases, the volume of the material defined by the integration increases. The matrix multiplication indicated by (5.33) is completed, and the integration in terms of  $r$  gives the local stiffness matrix. The total stiffness matrix and force matrix for the number of element solution is computed accordingly. Figure 5.7 shows the comparison of error analysis with the standard FEM, which uses linear Lagrange polynomial basis functions, and the linear, quadratic, cubic web-splines. As seen in Figure 5.7, the error decreases tremendously when web-splines basis functions are used. The error is in the third, fifth and seventh decimal place for the linear, quadratic, and cubic b-splines, respectively. With the results of higher order of polynomials web-spline method, like cubic web-spline, the results give good agreement with the exact solution.

Figure 5.8 illustrates the maximum error versus various permittivity values. The comparison of maximum error is with the standard FEM and the linear, quadratic, cubic web-splines. It is clearly seen that in Figure 5.8 the error increases for high permittivity values. So, high order polynomials like cubic web-splines are suitable.

### 5.3.3. Conclusion

In this Chapter, the web-splines approach in the FEM is applied to the electrostatic, and electromagnetic wave problems for inhomogeneous boundary conditions and

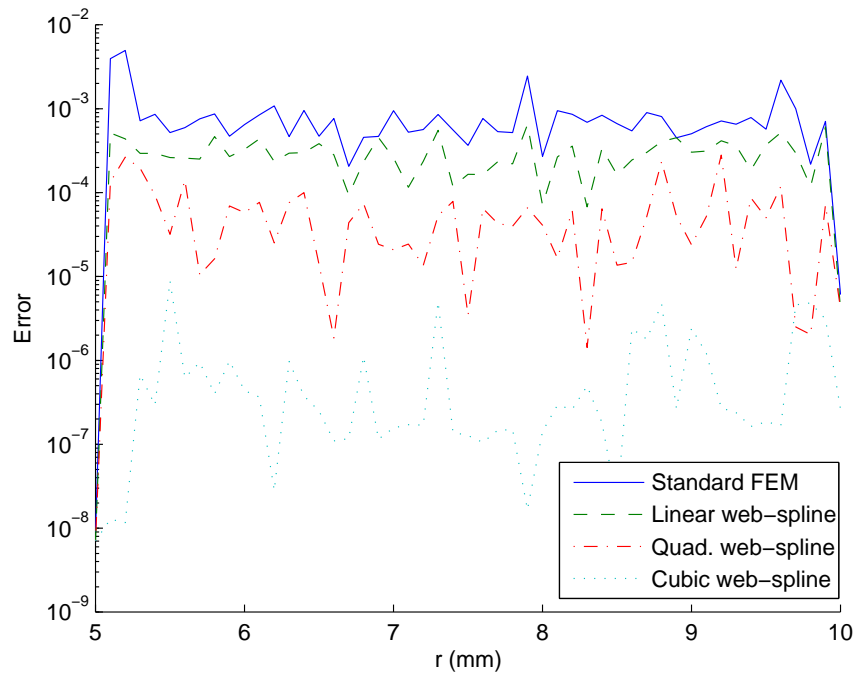


Figure 5.7. The error analysis of the coaxial cable using standard FEM (solid), linear (grey), quadratic (dot), and cubic (dash-dot) web-splines for a grid width of 0.1 mm in logarithmic scale

radially symmetric structures. This new method, which does not need mesh generation overcomes some of the drawbacks of using meshes and piecewise-uniform or linear trial functions.

The analysis presented in this study show the suitability of the proposed method to complex EM problems. This study proposed using the web-spline to solve the electric field problems in cylindrical coordinates. It is the first time that this method is applied to problems having inhomogeneous boundary conditions. The wave equation in cylindrical coordinates has been solved and accurate results have been obtained by increasing the degree of the basis function. With the higher order polynomials in the web-spline method, like the cubic web-spline, the results are in good agreement with the exact solution.

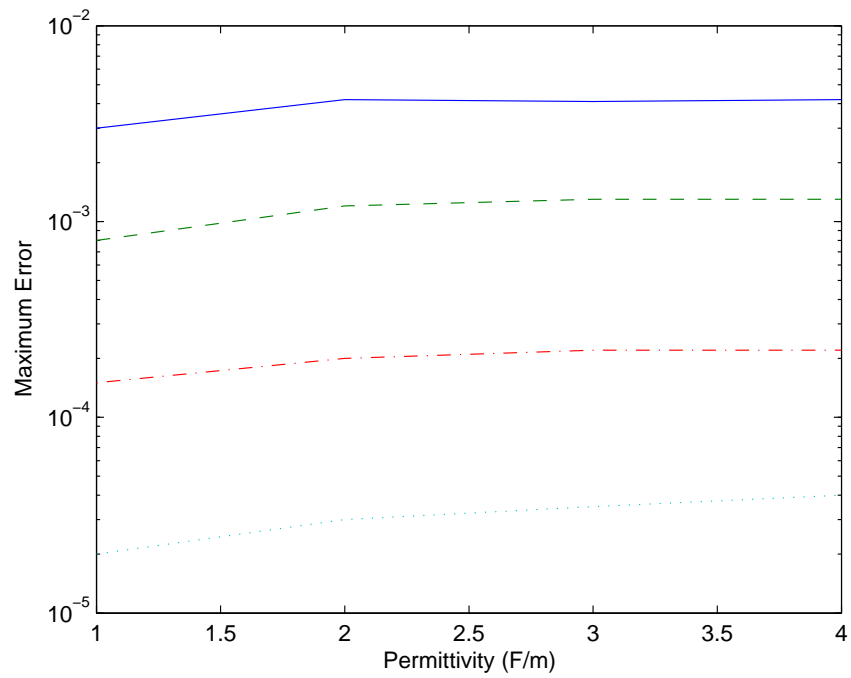


Figure 5.8. Maximum error analysis versus permittivity using standard FEM (solid), and linear (dash), quadratic (dot), and cubic (dash-dot) web-splines

## 6. 3D WEB-SPLINES SOLUTION TO HUMAN EYE HEAT DISTRIBUTION USING BIOHEAT EQUATION

A bioheat transfer model of the human eye is constructed using weighted extended b-splines as shape functions for the FEM. This newly developed computational approach is employed to calculate the steady-state temperature distribution in a normal human eye. Firstly, the human eye is evaluated in two dimensions. The simulation results which are verified using the values reported in the literature, point out better efficiency in terms of the accuracy level. Consequently, to give a more precise representation of the actual human eye, three dimensional modeling is simulated using these new finite elements in conjunction with linear, quadratic and cubic b-splines.

### 6.1. Introduction

Modeling of the heat distribution in the human eye has been popular for the last century with different kinds of techniques taking advantage of the advances in computational technology. In earlier studies, the finite difference time domain method (FDTD) was used to solve Pennes bioheat equations numerically. One of the first eye models in the literature was developed by [42]. They used the FDTD to calculate the transient solutions of the temperature distribution in a microwave-irradiated human eye. [43] also examined the thermal effects of microwave radiation on the human eye for the steady-state temperature distribution. [44] then developed a mathematical model based on the FDTD method to calculate the transient and steady-state temperature distributions in the normal unexposed human eye using the data he observed from the measurements of rabbit eyes. More recently, [45] applied FDTD method to study the temperature rise in the human eye exposed to electromagnetic waves. The drawback of these models was that they assumed the structure of the eye to be homogeneous in the sense that it is composed of a single uniform tissue. Thus, this model by not taking into account the presence of the cornea and the iris, and simplifying the blood flow inside the eye caused a significant error.

Although it is observed that the FDTD mathematical model cannot represent the human eye perfectly as the grids are rigid, the finite element method (FEM) allows precise representation of the ocular surface. The earliest reported model for temperature distribution in the eye using FEM was by [46] and [47]. Their numerical results which were for rabbit eyes subject to electromagnetic waves were reported to be in good agreement with data from experimental measurements. [48] and [49] constructed a two dimensional (2D) FEM of the human eye to analyze the temperature profile during steady-state. Later [50] used her model to compute the temperature rise in the eye when exposed to infrared radiation. The studies of [49, 50] were improved by [51, 52], and [53], respectively. They presented a 2D and three dimensional (3D) finite element and 2D boundary element human eye models which were developed to simulate thermal steady-state conditions of the eye based on the properties and parameters reported in the open literature. In addition, a three dimensional axisymmetric human eye model is developed using boundary element method (BEM) during treatment of laser thermokeratoplasty [54]. The specific regions such as tumor and anterior chamber of human eye's effects on the ocular heat transfer are also examined using BEM, respectively [55, 56]. A brief summary of the various mathematical models of the human eye developed up to date were reviewed in [57].

This chapter proceeds as follows. The mathematical model of the human eye with its properties for different domains is introduced in Section 2. Section 3 is dedicated to the method of the problem. The FEM formulation of the Pennes bioheat equation with the governing boundary equations is presented along with the web-spline method where grid cell classification on the domain, weight functions and numerical integrations are given in detail. Section 4 presents the results of comparing the 2D and 3D web-spline human eye model simulations with the other available FEM and experimental data, which are followed by the conclusion.

## 6.2. Mathematical Model of the Human Eye

The 2D and 3D models of the human eye are developed in this section. A 2D schematic cross section of the eye with the assumption that it is symmetric about the

pupillary axis is given in Figure 6.1, whereas the 3D model is formed by revolving this 2D model  $360^\circ$  around its horizontal pupillary axis. Simplifying assumptions concerning the geometry and structure of the eye are made in order to validate our web-spline model of the human eye using the latest studies done with FEM. First of all, the optic nerve is not simulated due to its minimal effect on the temperature distribution in the eye. Secondly, the eye is divided into six regions comprising the cornea, the aqueous humor, the lens, the iris, the vitreous humor, and the sclera. Each region is assumed to be homogeneous and isotropic. The thermal properties for each region are obtained based on [51] and the value for each is tabulated in Table 6.1. In addition, the coordinates of each region are modeled as in [51]. The properties and parameters used for the 3D model are similar to those of the 2D model.

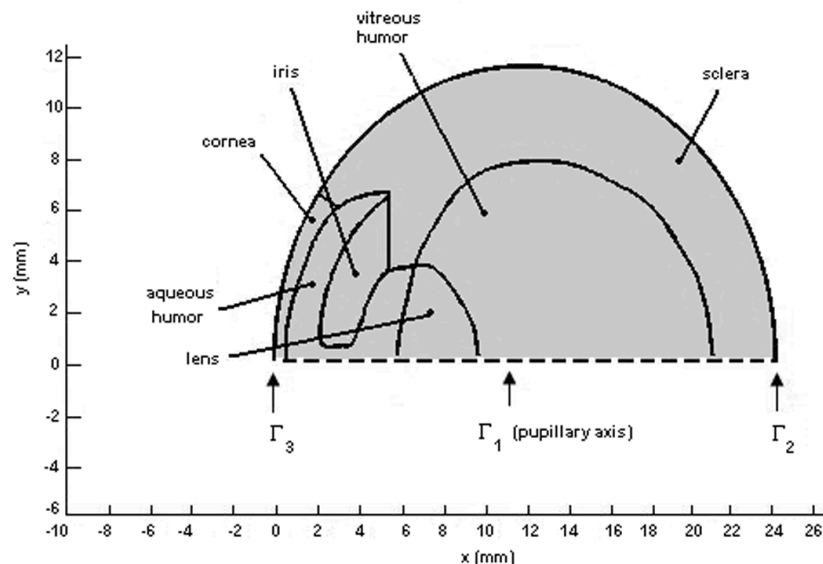


Figure 6.1. The 2D human eye model

The governing differential equation for temperature distribution is the Pennes bioheat transfer equation [58]:

$$\rho c \frac{\partial T}{\partial t} = \nabla \cdot (k \nabla T) + H \quad \text{in } \Omega (\text{inside the eye}) \quad (6.1)$$

where  $\Omega$  is the domain studied and  $\Gamma_1, \Gamma_2, \Gamma_3$  are its boundaries, as indicated in Figure 6.1. The boundary conditions are specified on the pupillary axis, the sclera and

Table 6.1. Properties of the human eye for different domains [51]

Domains	Thermal Conductivity ( $Wm^{-1}C^{-1}$ )	Density ( $kgm^{-3}$ )	Specific Heat Capacity ( $Jkg^{-1}C^{-1}$ )
Cornea	0.58	4178	1050
Aqueous humor	0.58	3997	996
Lens	0.40	3000	1050
Iris	1.0042	3180	1100
Vitreous humor	0.603	4178	1000
Sclera	1.0042	3180	1100

the cornea, given in (6.2), (6.3), and (6.4), respectively.

$$k \frac{\partial T}{\partial n} = 0 \quad \text{on} \quad \Gamma_1(\text{the pupillary axis}) \quad (6.2)$$

$$-k \frac{\partial T}{\partial n} = h_s(T - T_b) \quad \text{on} \quad \Gamma_2(\text{the sclera}) \quad (6.3)$$

$$-k \frac{\partial T}{\partial n} = E + h_c(T - T_{amb}) + \sigma \varepsilon (T^4 - T_{amb}^4) \quad \text{on} \quad \Gamma_3(\text{the anterior cornea surface}) \quad (6.4)$$

The parameters  $k$ ,  $\rho$ , and  $c$  which refer to thermal conductivity, specific heat capacity, and density, respectively, are assumed constant within each region and with temperature variations. The coefficients  $h_s$  ( $65Wm^{-2}C^{-1}$ ) and  $h_c$  ( $10Wm^{-2}C^{-1}$ ) describe the thermal exchanges by convection on the eye surface, respectively, from sclera to body core and from cornea to the surroundings. The other terms describing the radiative heat transfer are represented by  $T$ , unknown temperature ( $^{\circ}C$ );  $t$ , time (s);  $E$ , evaporation rate ( $40Wm^{-2}$ );  $T_{amb}$ , ambient temperature ( $25^{\circ}C$ );  $T_b$ , blood temperature ( $37^{\circ}C$ );  $n$ , the unit vector outward normal (m);  $\sigma$ , Stefan constant ( $5.67 \times 10^{-8}Wm^{-2}K^{-4}$ );  $\varepsilon$ , emissivity of corneal surface (0.975);  $H$ , heat source ( $Wm^{-3}$ ).

The initial temperature distribution ( $t = 0$ ) is found by solving the steady-state

heat transfer equation with no external heat sources as in,

$$\nabla \cdot (k \nabla T) = 0 \quad (6.5)$$

### 6.3. Method of Analysis

In this section, the first the procedures for applying the FEM method to the bioheat equation are described. Additionally, the b-splines and web-splines will be outlined only in 3D, since the detailed account of the method can be found in the literature [10].

#### 6.3.1. The Weak Formulation of the Bioheat Equation

The bioheat transfer equation is used in calculating the temperature distribution in the human eye wherein the domain  $\Omega$  has smooth subdomains  $\Gamma_{1-3}$ . To calculate the approximate temperature  $T_h$ , a variational statement of the steady state problem is obtained by multiplying (6.1) by an arbitrary test function  $B_k$  and integrating the equality. The weak formulation becomes:

$$\int_{\Omega} \left( -\nabla(k \nabla T_h) + \rho c \frac{\partial T_h}{\partial t} - H \right) B_k d\Omega \quad (6.6)$$

Employing the Green's theorem, (6.6) can be expressed as the sum of the functions  $T_1, T_2$ , and  $T_3$  which yield the differential equations,

$$T_1 = -k \int_{\Omega} (\nabla T_h \cdot \nabla B_k^t) d\Omega - \rho c \int_{\Omega} B_k \frac{\partial T_h}{\partial t} d\Omega + H \int_{\Omega} B_k d\Omega \quad \text{volume term} \quad (6.7)$$

$$T_2 = - \int_{\Gamma_2} h_s B_k (T_h - T_b) d\Gamma_2 \quad \text{sclera term} \quad (6.8)$$

$$T_3 = - \int_{\Gamma_3} [h_c B_k (T_h - T_{amb}) + \sigma \varepsilon B_k (T^4 - T_{amb}^4)] d\Gamma_3 \quad \text{cornea term} \quad (6.9)$$

where  $B_k^t$  denotes the transposed matrix of  $B_k$ . The approximate temperature  $T_h$  is replaced with the solution which consists of  $e$  nodes:

$$T_h = \sum_{i=1}^e \alpha_i B_i \quad (6.10)$$

where  $\alpha_i$  indicates the coefficient of the basis functions  $B_i$ . Following the derivation for  $\frac{\partial(T_1, T_2, T_3)}{\partial T}$ , the matrix formulation below is obtained:

$$\left\{ \frac{\partial \sum T}{\partial T} \right\}^e = [K]^e \{T_h\}^e + [M]^e \left\{ \frac{\partial \sum T_h}{\partial t} \right\}^e - \{G\}^e \quad (6.11)$$

where  $i, k = 1 \dots e$ ,

$$[K]^e = k \int_{\Omega^e} \nabla B_i \nabla B_k^t d\Omega^e + h_s \int_{\Gamma_2^e} \nabla B_i \nabla B_k d\Gamma_2^e + h_c \int_{\Gamma_3^e} \nabla B_i \nabla B_k d\Gamma_3^e + \int_{\Gamma_3^e} \sigma \varepsilon (T^4 - T_{amb}^4) B_i d\Omega \quad (6.12)$$

$$[M]^e = \int_{\Omega^e} \rho c B_i B_k^t d\Omega^e \quad (6.13)$$

$$\{G\}^e = (h_c T_{amb} - E) \int_{\Gamma_3^e} B_i d\Gamma_3^e + h_s T_b \int_{\Gamma_2^e} B_i d\Gamma_2^e + H \int_{\Omega^e} B_i d\Omega^e \quad (6.14)$$

Hence, after assembling the elementary matrices, the global system is:

$$\frac{\partial(T_1 + T_2 + T_3)}{\partial T} = \sum_{e=1}^e \left\{ \frac{\partial(T_1 + T_2 + T_3)}{\partial T} \right\}^e = [K]\{T\} + [M] \left\{ \frac{\partial T}{\partial t} \right\} - \{G\} = 0 \quad (6.15)$$

where  $[K]$  is called the global stiffness matrix,  $[M]$  the global mass matrix and  $\{G\}$  is the global load matrix considering boundary conditions.

### 6.3.2. Web-spline Approximation

Having briefly discussed necessary background material for web-splines in Chapter 3, temperature distribution analysis of FEM with web-splines is straightforward. Rewriting (6.10) in 3D using web-splines as finite element basis functions, (6.16) is obtained.

$$T_h(i) = \sum_u \sum_v \sum_w \alpha_{u,v,w,i} B_{u,v,w}(x_i, y_i, z_i) \quad (6.16)$$

where  $B$  is the web-spline basis function,  $x, y, z$  are the coordinates,  $u, v, w$  are web-spline parameters and  $\alpha$  is the coefficient of basis functions. Each point in the equation has three coordinates. Summation is done over all the defined control point 3D tensor products for a given  $xyz$  location. The basis function for a given location is calculated from the degree of the web-spline using the standard iterative formula [6]. Thus, to obtain the approximate solution of the temperature distribution in the eye, the web-splines are incorporated into the global matrix equation in (6.15), and the linear system of equations are assembled and solved easily with the program written in MATLAB.

## 6.4. Simulation Results

In this section, we investigate the steady-state temperature distribution in the 2D and 3D unexposed human eye models, with the use of the web-spline method. For each model, grid convergence analysis has been done. The simulations are performed using linear, quadratic and cubic b-splines with 0.0625 and 0.125 grid widths, respectively. In order to confirm the validity of our results, we compare them with those reported in [49, 51], and [52]. We adjust the thermal properties of the eye tissue constants and size of our model to those in [51], and [52] for 2D and 3D simulations, respectively.

### 6.4.1. 2D results

First, to find the optimum grid number, we computed cubic web-spline approximations for different grid widths  $h=0.5, 0.25, 0.125, 0.0625, 0.03125$ . This grid con-

vergence test is shown graphically in Figure 6.2. It is deduced from the figure that as the grid number increases, the temperature results on the corneal surface gets more stabilized. The optimum number of grids is found to be 193 for which  $h$  is 0.0625.

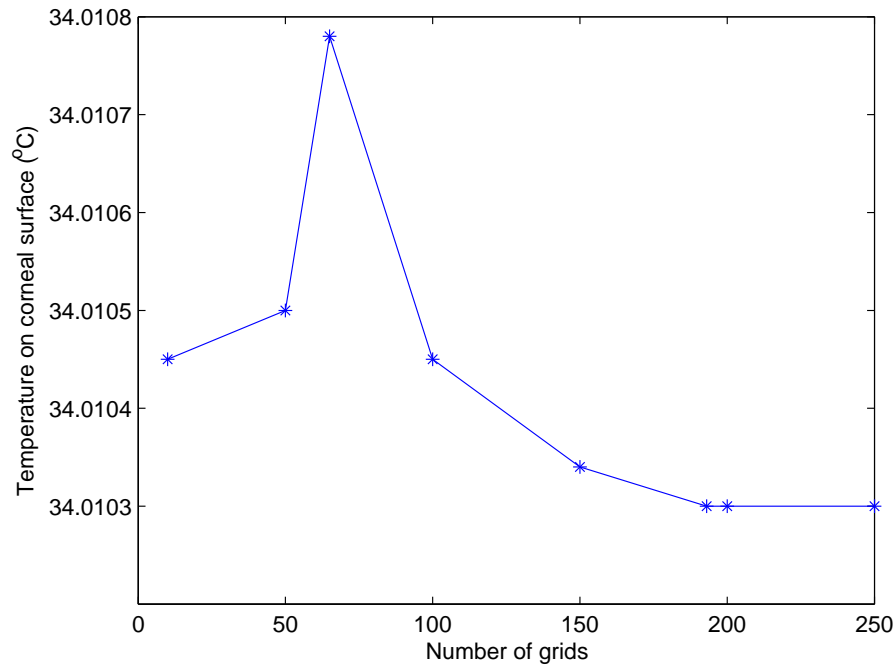


Figure 6.2. Grid convergence for the 2D web-spline model

We illustrate in Figure 6.3 the inner ( $\bullet$ ), the outer ( $\circ$ ) and the extended ( $\blacktriangle$ ) b-splines using cubic basis splines in the 2D human eye whose dimensions are given in Figure 6.1. The simulations were also performed with linear and quadratic b-splines. With cubic b-splines; 39 outer, 42 standard inner and 112 extended inner b-splines are used in the simulations.

The thermal model of the 2D human eye is given in Figure 6.4. From this figure it is clearly observed that the lowest temperature,  $34.01^{\circ}C$  appears on the corneal surface. The highest temperature occurs as we move away from the cornea towards the sclera.

The latest study regarding the calculation of the temperature distribution at steady state with no exposure to radiation in the 2D human eye is done by [49, 51] using the method of finite elements. A corneal surface of  $33.25^{\circ}C$  was obtained in [49]

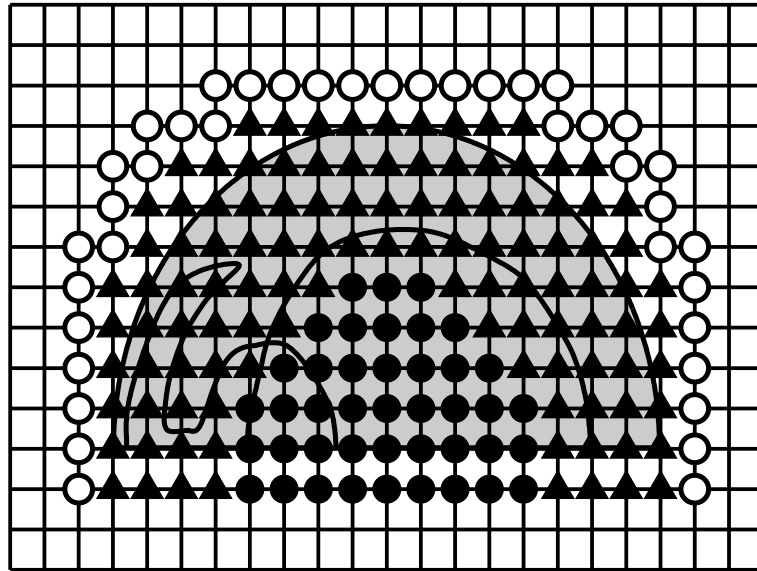


Figure 6.3. The standard (•), extended inner (▲) and outer (◊) cubic b-splines for the human eye

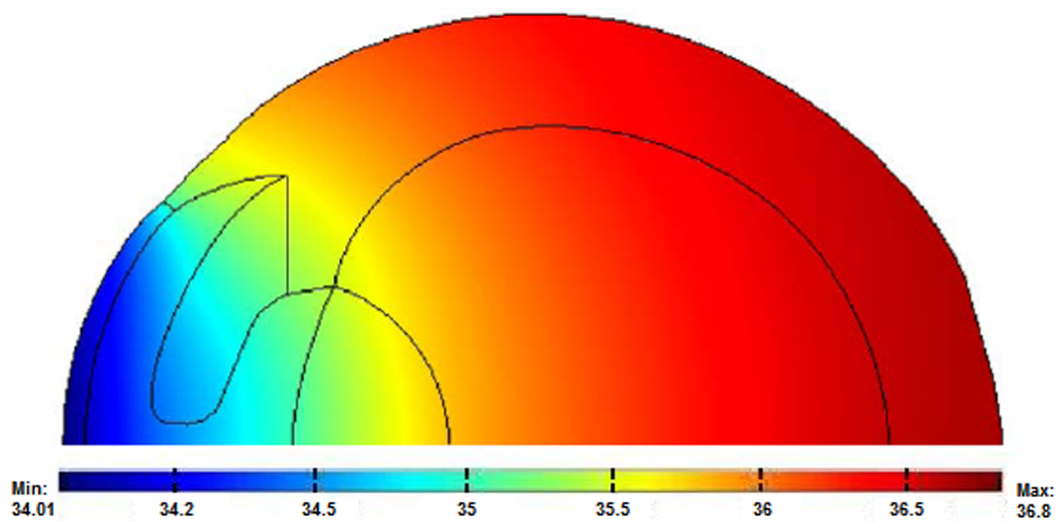


Figure 6.4. Thermal pattern of the 2D model without exposure to radiation

with 496 nodes, and in [51]  $33.64^{\circ}\text{C}$  was approximately found with 8557 triangular elements. Figure 6.5 compares the temperature along the pupillary axis predicted by the two studies with that of the 2D web-spline method. Figure 6.5 reveals that the calculated temperatures along the axis of symmetry are in good agreement with those from the previous 2D finite element studies. In addition, as is evident from Table 6.2, this low number of grids in web-spline technique makes the computation time very low such as 0.1s, 0.2s, and 0.3s for linear, quadratic and cubic b-splines, respectively. The configurations of the computer in the simulations are as follows:

- Microsoft Windows XP, Professional, Version 2002,
- 3.40 GHz Processor,
- 1 GB RAM.

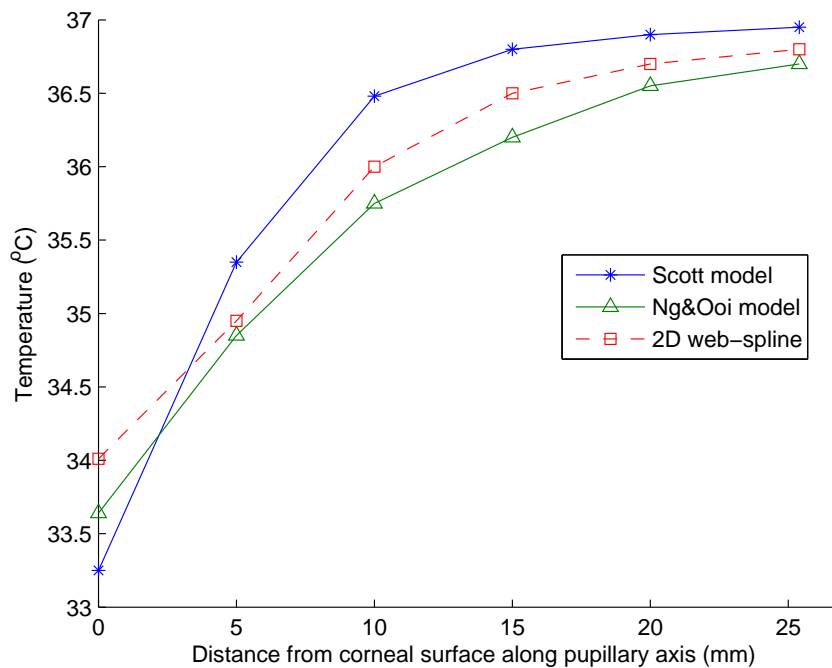


Figure 6.5. Comparison between the 2D web-spline model, [49] and [51]

#### 6.4.2. 3D results

In this subsection, we examined the temperature distribution at steady-state in the 3D human eye model. The 3D model is constructed by revolving one half of the 2D model  $360^{\circ}$  around its horizontal pupillary axis and is depicted in Figure 6.6.

Table 6.2. Efficiency comparison of web-splines with standard FEM studies

Method	Number of Nodes
[49]	496
[51]	8557
Linear 2D Web-spline	137
Quadratic 2D Web-spline	164
Cubic 2D Web-spline	193

First, grid convergence analysis is illustrated in Figure 6.7 for cubic b-splines where the optimum grid width is calculated to be 0.125 (5203 grids) when the gradient of the graph approaches zero. Thus it is assumed that any decreases in the grid width do not change the simulation results.



Figure 6.6. The 3D human eye model

Overview of the 3D human eye model for two layers with the outer, the extended inner and the standard inner cubic web-splines for a grid width of 0.125 are shown in Figure 6.8. There are 2843 extended inner b-splines marked with triangles, 1754 outer b-splines marked with white circles and 606 standard inner b-splines which appear in

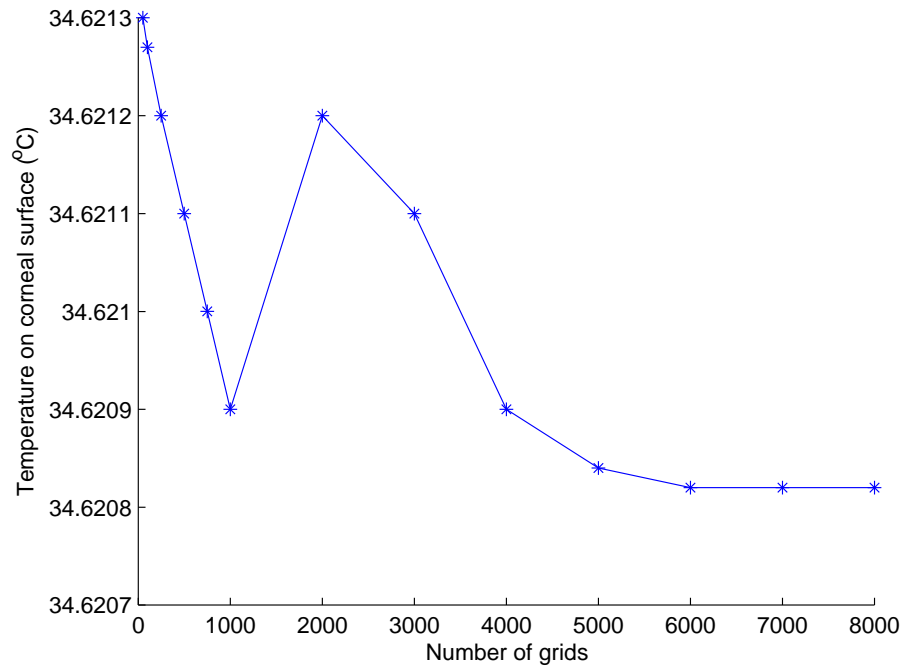


Figure 6.7. Grid convergence for the 3D web-spline model

the middle layer of the sphere. If larger grid width had been used, all inner b-splines would be affected by the outer b-splines and become extended inner b-splines.

The numerical value of the temperature in the thermal pattern of the eye model is calculated to be  $34.52^{\circ}C$  for linear,  $34.55^{\circ}C$  for quadratic, and  $34.62^{\circ}C$  for cubic web-splines at the center of the corneal surface. Figure 6.9 plots the local temperature variation along the horizontal pupillary axis for the FEM models developed by [49]’s 2D, [52]’s 3D models, and the current 3D cubic web-spline model. The temperature distribution of the 3D web-spline model is very similar to those in [49] and [52]. Slight differences in the compared results are mostly attributable to the differences in the modeling of the human eye. In Figure 6.10, the comparison between the different 3D models, namely the one in Ng [52] and the web-spline methods, is shown for the linear, quadratic, and cubic web-splines. In the simulations, it appears that the temperature is decreased at the center of the corneal surface.

The simulation results are compared with the values reported by [51] in which they summarized the results of the corneal surface temperature obtained from the previous

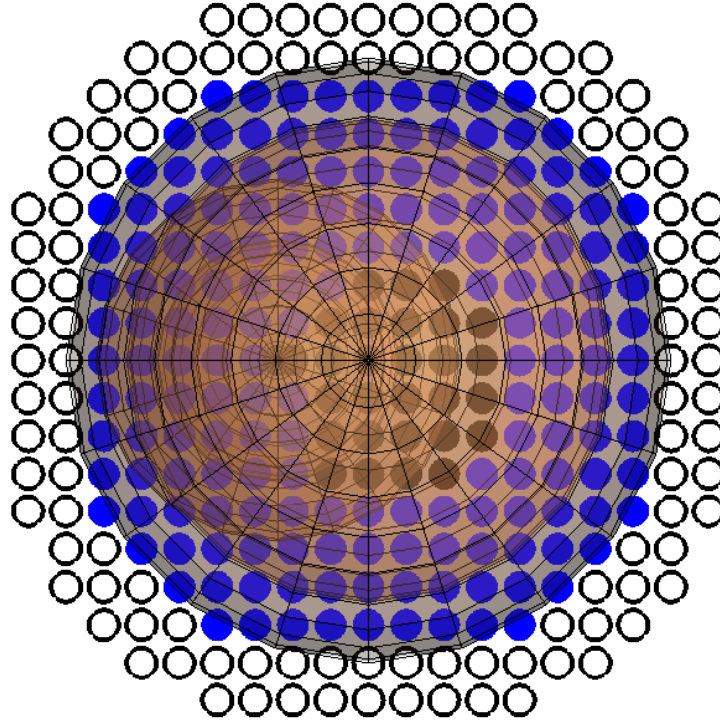


Figure 6.8. Grid representation for the 3D human eye model

experimental studies with the mean value of  $34.65^{\circ}C$ . These studies are depicted in Table 6.3. Upon investigations, it was found that the 3D cubic web-spline model gives only a temperature difference of  $0.03^{\circ}C$  as compared to the  $0.64^{\circ}C$  for the 2D cubic web-spline model.

Table 6.4 summarizes the comparisons between the FEM results on the corneal surface inside the human eye model and the web-spline model. When we compare the simulation results with the mean value of  $34.65^{\circ}C$  on the corneal surface, the current 3D model obtained a discrepancy of only 0.178% while the result of [51] produced a discrepancy of 0.455% and [52] produced a discrepancy of 0.33%. There are some deviations in the results. The reasons for these deviations are the different ambient temperature used ( $20^{\circ}C$  versus  $25^{\circ}C$ ) and the different approximations of material properties in the model. The choice of  $25^{\circ}C$  ambient temperature in the current model is based on a typical laboratory condition in Turkey. In [51], the iris and ciliary body

Table 6.3. The summary of the results of the corneal surface temperature obtained from the previous studies

<b>Author</b>	<b>Mean Temperature °C</b>	<b>Technique</b>
Dohnberg, 1876	36.6	Mercury bulb
Galozowski, 1877	36.4	Mercury bulb
Silex, 1893	35.55	Thermo-element
Gilese, 1894	35.72	Thermo-element
Hertel, 1900	35.65	Mercury bulb
Kirisawa, 1942	34.5	Thermo-element
Holmberg, 1952	36.24	Thermo-electric
Hamano at al, 1964	34	Thermistor
Hill and Leighton, 1965	32.1	Thermistor
Mapstone, 1968	34.8	Infrared
Kolstrad, 1970	32	Thermistor
Kinn and Tell, 1973	35.5	Liquid crystal
Rysa and Sarvaranta, 1974	34.8	Infrared
Horven, 1975	33.67	Contact probe
Hamano at al, 1976	34.4	Infrared
Fatt and Chaston, 1980	34.5	Infrared
Alio and Padron, 1981	32.9	Infrared
Fielder, Winder, Sheridaihah at al	33.4	Infrared
Martin and Fatt, 1985	34.5	Heat flow
Mean Temperature °C	34.65	

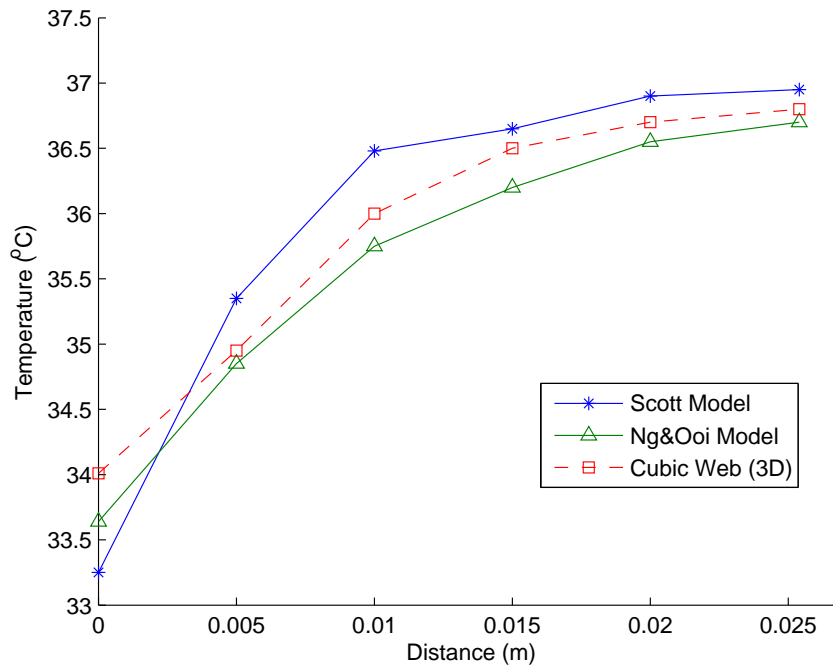


Figure 6.9. Comparison of the results for the 3D model using the methods in [49], [52] and the cubic web-spline method

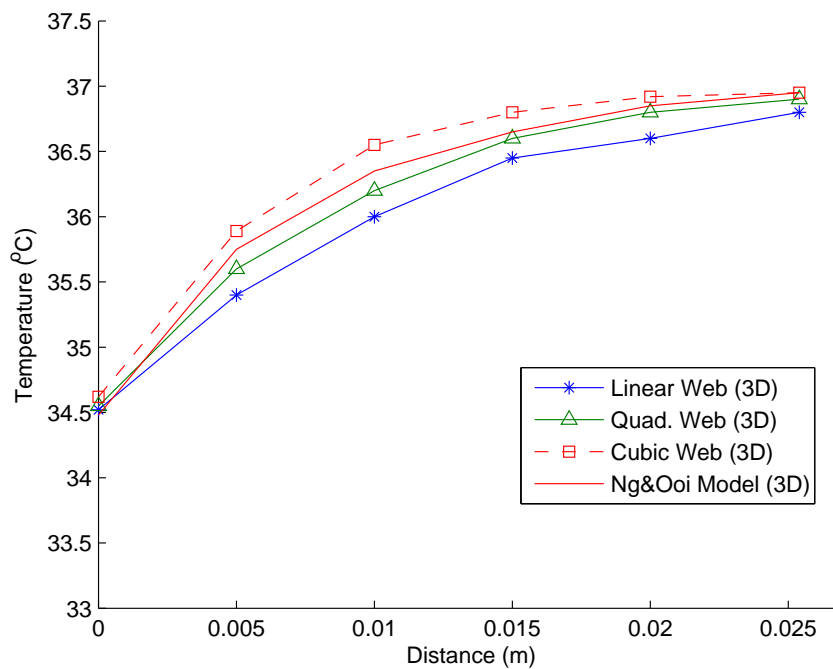


Figure 6.10. Comparison of the results for the 3D model using the method in [52] and the linear, quadratic, and cubic web-spline method

were assumed to have properties similar to aqueous humor whereas the current model obtained different properties for iris and sclera. The number of grids generated in the 3D web-spline model is 2904, 4272, and 5203 for linear, quadratic and cubic b-splines, respectively, whereas 54,796 elements had been used in [52]. The computation time is 1.2s, 1.4s, and 1.5s for linear, quadratic and cubic b-splines, respectively.

Table 6.4. Comparison between the mean value of the experimental results,  $34.65^{\circ}C$  with FEM and the web-spline method solutions on the corneal surface

Author	Method used	Temperature ( $^{\circ}C$ )	Absolute Difference ( $^{\circ}C$ )	Percentage Difference ( $^{\circ}C$ )
[49]	FEM	33.25	1.4	4.04
[51]	FEM	33.64	1.0	2.91
[52]	FEM	34.48	0.17	0.49
Kunter (3D)	Web-spline (linear)	34.52	0.13	0.38
Kunter (3D)	Web-spline (quadratic)	34.55	0.1	0.29
Kunter (3D)	Web-spline (cubic)	34.62	0.03	0.09

## 6.5. Conclusion

A FEM with web-splines, which models the heat transfer in the normal unexposed 2D and 3D representations of the human eye have been developed and employed to calculate the steady-state temperature distribution based on the properties and parameters reported in the literature. Error analysis indicates that our web-spline based method is successful in determining the temperature distribution in the eye.

Based on the investigations in this study, the 3D web-spline model was found to yield better accuracy than the 2D web-spline model and is able to give a more precise interpretation of the temperature inside the human eye. The reason why the differences become larger in the 2D models is that, the actual eye model cannot be sufficient in 2D. Altogether, the 3D heat transfer model is shown to be a more significant representation of the actual human eye than the 2D model.

## 7. WEB-SPLINE COMPUTATION OF TEMPERATURE RISE WITHIN A MODEL OF THE MICROWAVE-IRRADIATED HUMAN EYE

This section is the continuation of the previous Chapter where the only steady-state temperature distribution has been calculated for the unexposed human eye. In this section, we report a calculation of the microwave fields within a model of the human eye. FEM with web-spline computer modeling have been applied to study the corneal surface temperature increase during microwave irradiation. The heat conduction model of the microwave-irradiated eye which is assumed to be 3D is also constructed. The mechanism of heat transfer from the eye and the selection of the thermal parameters of the media of the eye are also discussed. The implementation of these parameters in the web-spline solution of the heat conduction is then developed. Furthermore, temperature rises calculated are compared with the values found in the literature pertaining to microwave-induced cataract formation.

### 7.1. Introduction

Early theoretical work in the area of the biological effects of electromagnetic radiation is centered on the entire human body irradiation. However, because experimental work indicated that harmful local tissue temperature rises could occur, interest in partial body irradiation was stimulated. Under conditions of partial-body exposure to intense EM waves, significant thermal damage can occur in sensitive tissues. One of the most sensitive organs for EM wave exposure is the human eye.

The human eye is one of the most sensitive organs under EM exposure. The exposure of the eye to RF radiation can be sufficient to damage tissues owing to temperature rise. RF energy is generally absorbed in the cornea on the front surface of the eye. A number of models of heat transport in the eye have been proposed, motivated by the development of cataracts after exposure of the eye to infrared and

microwave radiation which are the most common sources of heat that the human eye may be exposed.

One of the earliest study on the thermal effects of microwave radiation in the human eye was done by [43]. They assumed that the eye was spherical and composed of uniform tissue. An analytical solution to the 1-D heat transfer problem was developed for steady state conditions and did not account for transient temperature distributions. [42] computed induced temperatures within a model of the microwave-irradiated human eye at 750 MHz and 1.5 GHz. They concluded that at frequencies higher than 1.5 GHz, maximum temperatures could occur within the eye. With the same incident power level, similar temperature values are computed by Guy et. al. at 2.45 GHz in the irradiated rabbit's eye. Thus, [42] imply that microwave heating of the rabbit eye and of the human eye can be correlated. Another early investigation which included a finite element heat transport model for the rabbit eye was presented by [46]. The initial temperature distribution of normal rabbit eye and eye exposed to microwave radiation was obtained from experimental measurements carried out on actual rabbits.

As wireless communication and industrial, scientific and medical applications of radio frequency have rapidly grown, it is important to consider possible health hazards due to this type of non-ionizing radiations. Temperature rises for the human eye exposure to RF energy were investigated in [59-62]. Various sources of microwave radiation such as mobile phones [63, 64], user antenna in wireless local area networks [65, 66] and radar equipment [45], [67-69] have been investigated. Results from these numerical investigations enabled exposure limits in the various frequency ranges of microwaves to be defined that would help to reduce the potential hazards of microwave radiation.

## 7.2. Thermal Model of The Human eye

### 7.2.1. Electrical Parameters of Eye

Due to the lack of experimental data at the microwave frequencies, the evaluation of the complex permittivity values related to the eye tissues is done by using the Debyes dispersion equation. Debyes equation gives the complex permittivity ( $\epsilon^*$ ) of a dielectric material as a function of the frequency ( $f$ ), according to

$$\epsilon^*(f) = \epsilon'(f) + \frac{\sigma(f)}{j2\pi f\epsilon_0} = \epsilon_\infty + \frac{\sigma_s}{j2\pi f\epsilon_0} + \frac{\epsilon_s - \epsilon_\infty}{1 + j\frac{f}{f_r}} \quad (7.1)$$

where  $f_r$  is the relaxation frequency,  $\epsilon_s - \epsilon_\infty$  is the change in the permittivity due to this relaxation process, and  $\sigma_s$  and  $\epsilon_\infty$  are the limits of the conductivity at very low frequencies and of the permittivity at very high frequencies, respectively [62]. Debye parameters for cornea are  $f_r = 21.5(GHz)$ ,  $\epsilon_s = 42.62$ ,  $\epsilon_\infty = 5.1$ ,  $\sigma_s = 1.21(S/m)$ . For cornea, dielectric and conductivity constants were simplified as a polynomial functions [70].

Polynomial function fitting for permittivity and conductivity of cornea at 1 – 30GHz are

$$\begin{aligned} \epsilon(f) &= -4.9 \times 10^{-5} f^4 + 0.004191 f^3 - 0.112 f^2 + 0.09232 f + 42.62 \\ \sigma(f) &= 5.858 \times 10^{-5} f^4 - 0.005011 f^3 + 0.1342 f^2 - 0.1103 f + 1.308 \end{aligned} \quad (7.2)$$

Dielectric and conductivity variations of cornea tissue is shown in Figure 7.1 with respect to frequency. In this study, human eye model is considered as a homogeneous semi-infinite tissue block characterized with known thermal and physical properties [60].  $H(x, t)$  is the heat source due to electromagnetic energy absorbed by tissue. The power deposited in a semi-infinite tissue exposed to incident electromagnetic wave is

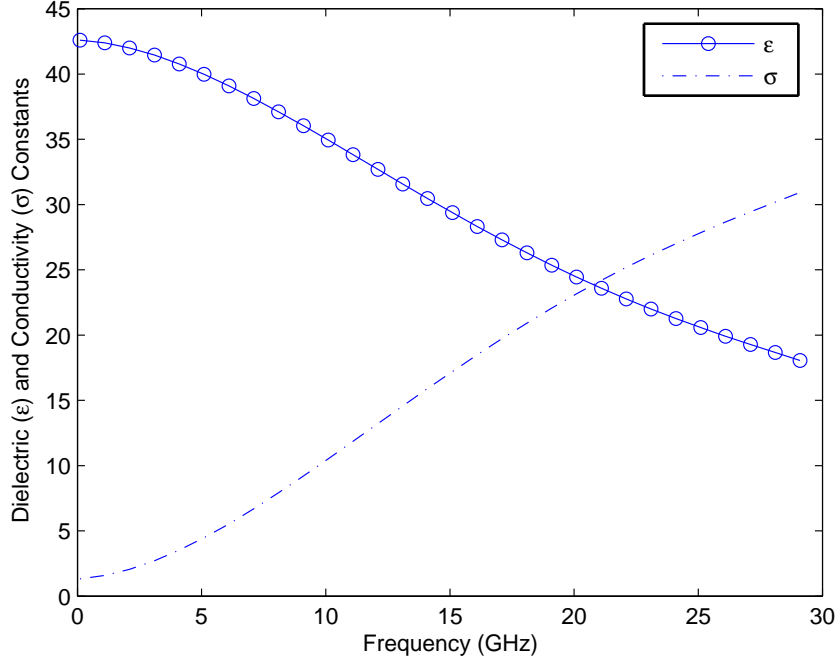


Figure 7.1. Dielectric and conductivity variations of cornea tissue

given as below

$$H(x, t) = \frac{2I_0\zeta}{\delta} e^{-2x/\delta} U(t) \quad (7.3)$$

where  $I_0$  is the power density of incident electromagnetic wave ( $W/m^2$ ),  $\zeta$  is power transmission coefficient between air and tissue,  $\delta$  is penetration depth, and  $U(t)$  is the unit step function. For a plane uniform electromagnetic wave incident normally to the skin surface, the SAR between the tissue can be determined as  $H(x, t)/\rho$ , where  $\rho$  is the density ( $kg/m^3$ ).

Due to biological tissues are nonmagnetic medium, power transmission coefficient  $\zeta$  is defined only with permittivities of free space and the tissue [60].

$$\zeta = 1 - \left| \frac{\sqrt{\epsilon^* \cdot \epsilon_0} - \sqrt{\epsilon_0}}{\sqrt{\epsilon^* \cdot \epsilon_0} + \sqrt{\epsilon_0}} \right|^2 \quad (7.4)$$

The penetration depth  $\delta$  is given as below

$$\delta = \left( \frac{67.52}{f} \right) \left[ \sqrt{(\epsilon')^2 + (\epsilon'')^2} - \epsilon' \right]^{-1/2} \quad (7.5)$$

where  $f$  is the frequency in  $MHz$ , and  $\epsilon'$  and  $\epsilon''$  are the real and imaginary parts of the complex relative permittivity. Table 7.1 depicts the electrical parameters of the cornea at the frequency of interest.

Table 7.1. Electrical parameters of the cornea at the certain frequencies

Frequency $f, GHz$	Permittivity $\epsilon$	Conductivity $\sigma, S/m$	Energy Transmission Coefficient, $\zeta$	Skin Depth $\delta, mm$
1	42.604	1.326	0.4268	27.445
1.8	42.446	1.515	0.446	23.064
2.45	42.23	1.77	0.4507	19.54
6	39.97	4.47	0.458	7.633
10	36.014	9.199	0.4647	3.547
18	27.194	19.728	0.4834	1.483
30	17.786	30.93	0.517	0.802

### 7.2.2. Time Dependent Heat Conduction

The governing differential equation for temperature distribution is the Pennes bioheat transfer equation:

$$\rho c \frac{\partial T}{\partial t} = \nabla(k \nabla T) + H(x, t) \quad \text{in } \Omega(\text{inside the eye}) \quad (7.6)$$

where  $\Omega$  is the domain studied, and  $\Gamma_1, \Gamma_2$  are its boundaries, as indicated in Figure 6.1. The boundary conditions are specified on the sclera and the cornea, given in (7.7), and (7.8) respectively.

$$-k \frac{\partial T}{\partial n} = h_s(T - T_b) \quad \text{on } \Gamma_1(\text{the sclera}) \quad (7.7)$$

$$-k \frac{\partial T}{\partial n} = E + h_c(T - T_{amb}) + \sigma \varepsilon (T^4 - T_{amb}^4) \quad \text{on} \quad \Gamma_2(\text{the anterior cornea surface}) \quad (7.8)$$

The solution of simplified bioheat equation for the surface temperature ( $T(0, t)$ ) is given in [60] as

$$T(0, t) = \left( \frac{I_0 \times \delta \times \zeta}{2k} \right) \times \left[ 2\sqrt{\frac{t}{\pi\tau}} + e^{t/\tau} \operatorname{erfc}\left(\sqrt{\frac{t}{\tau}}\right) - 1 \right] \quad (7.9)$$

$$\tau = \frac{\delta^2 \rho C}{4k} \quad (7.10)$$

where  $\tau$  is the time required for thermal energy to diffuse a distance equal to energy penetration depth,  $\operatorname{erfc}(x)$  is the complementary error function.

### 7.2.3. Derivation of Finite Element Equations

By multiplying both sides of (7.6) by  $\phi^e = \begin{Bmatrix} \phi_1^{(e)} \\ \phi_2^{(e)} \end{Bmatrix}$  where  $\phi_1^{(e)}$  and  $\phi_2^{(e)}$  are the linear shape functions and integrating over  $[x_1^{(e)}, x_2^{(e)}]$ , we get

$$\int_{x_1^{(e)}}^{x_2^{(e)}} \rho C \begin{Bmatrix} \phi_1^{(e)} \\ \phi_2^{(e)} \end{Bmatrix} \frac{\partial T}{\partial t} dx = \int_{x_1^{(e)}}^{x_2^{(e)}} \begin{Bmatrix} \phi_1^{(e)} \\ \phi_2^{(e)} \end{Bmatrix} \left[ \frac{\partial}{\partial x} \left( k_x \frac{\partial T}{\partial x} \right) + H \right] dx \quad (7.11)$$

By using integration by parts formula, right side of (7.11) becomes

$$\begin{aligned} \int_{x_1^{(e)}}^{x_2^{(e)}} \begin{Bmatrix} \phi_1^{(e)} \\ \phi_2^{(e)} \end{Bmatrix} \frac{\partial}{\partial x} \left( k_x \frac{\partial T}{\partial x} \right) dx &= k_x \frac{\partial T}{\partial x} \begin{Bmatrix} \phi_1^{(e)} \\ \phi_2^{(e)} \end{Bmatrix} \Big|_{x_1^{(e)}}^{x_2^{(e)}} - \int_{x_1^{(e)}}^{x_2^{(e)}} \begin{Bmatrix} \frac{\partial \phi_1^{(e)}}{\partial x} \\ \frac{\partial \phi_2^{(e)}}{\partial x} \end{Bmatrix} \left( k_x \frac{\partial T}{\partial x} \right) dx \\ &= \begin{Bmatrix} -k_x \frac{\partial T}{\partial x} \Big|_{x=x_1^{(e)}} \\ k_x \frac{\partial T}{\partial x} \Big|_{x=x_2^{(e)}} \end{Bmatrix} - \int_{x_1^{(e)}}^{x_2^{(e)}} k_x \begin{Bmatrix} \frac{\partial \phi_1^{(e)}}{\partial x} \\ \frac{\partial \phi_2^{(e)}}{\partial x} \end{Bmatrix} \frac{\partial T}{\partial x} dx \end{aligned} \quad (7.12)$$

Combining (7.11) and (7.12), and rearranging the terms, we get

$$\int_{x_1^{(e)}}^{x_2^{(e)}} \rho C \begin{Bmatrix} \phi_1^{(e)} \\ \phi_2^{(e)} \end{Bmatrix} \frac{\partial T}{\partial t} dx + \int_{x_1^{(e)}}^{x_2^{(e)}} k_x \begin{Bmatrix} \frac{\partial \phi_1^{(e)}}{\partial x} \\ \frac{\partial \phi_2^{(e)}}{\partial x} \end{Bmatrix} \frac{\partial T}{\partial x} dx = \begin{Bmatrix} -k_x \frac{\partial T}{\partial x} \Big|_{x=x_1^{(e)}} \\ k_x \frac{\partial T}{\partial x} \Big|_{x=x_2^{(e)}} \end{Bmatrix} + \int_{x_1^{(e)}}^{x_2^{(e)}} \begin{Bmatrix} \phi_1^{(e)} \\ \phi_2^{(e)} \end{Bmatrix} \cdot H dx \quad (7.13)$$

In the terms on the left side of (7.11) we replace  $T(x, t)$  by the finite element interpolation  $[\phi_1^{(e)}(x)\phi_2^{(e)}(x)] \begin{Bmatrix} T_1^{(e)}(t) \\ T_2^{(e)}(t) \end{Bmatrix}$ . Then the term  $\int_{x_1^{(e)}}^{x_2^{(e)}} \rho C \begin{Bmatrix} \phi_1^{(e)} \\ \phi_2^{(e)} \end{Bmatrix} \frac{\partial T}{\partial t} dx$  is replaced by

$$\begin{aligned} & \left( \int_{x_1^{(e)}}^{x_2^{(e)}} \rho C \begin{Bmatrix} \phi_1^{(e)} \\ \phi_2^{(e)} \end{Bmatrix} [\phi_1^{(e)}(x)\phi_2^{(e)}(x)] dx \right) \frac{d}{dt} \begin{Bmatrix} T_1^{(e)} \\ T_2^{(e)} \end{Bmatrix} \\ &= \left( \int_{x_1^{(e)}}^{x_2^{(e)}} \rho C \begin{bmatrix} \phi_1^{(e)}\phi_1^{(e)} & \phi_1^{(e)}\phi_2^{(e)} \\ \phi_2^{(e)}\phi_1^{(e)} & \phi_2^{(e)}\phi_2^{(e)} \end{bmatrix} dx \right) \frac{d}{dt} \begin{Bmatrix} T_1^{(e)} \\ T_2^{(e)} \end{Bmatrix} \end{aligned} \quad (7.14)$$

The term  $\int_{x_1^{(e)}}^{x_2^{(e)}} k_x \begin{Bmatrix} \frac{\partial \phi_1^{(e)}}{\partial x} \\ \frac{\partial \phi_2^{(e)}}{\partial x} \end{Bmatrix} \frac{\partial T}{\partial x} dx$  is replaced by

$$\left( \int_{x_1^{(e)}}^{x_2^{(e)}} k_x \begin{bmatrix} \frac{\partial \phi_1^{(e)}}{\partial x} \frac{\partial \phi_1^{(e)}}{\partial x} & \frac{\partial \phi_1^{(e)}}{\partial x} \frac{\partial \phi_2^{(e)}}{\partial x} \\ \frac{\partial \phi_2^{(e)}}{\partial x} \frac{\partial \phi_1^{(e)}}{\partial x} & \frac{\partial \phi_2^{(e)}}{\partial x} \frac{\partial \phi_2^{(e)}}{\partial x} \end{bmatrix} dx \right) \begin{Bmatrix} T_1^{(e)} \\ T_2^{(e)} \end{Bmatrix} \quad (7.15)$$

As a result, we get

$$\mathbf{M}^{(e)} \dot{\mathbf{T}}^{(e)} + \mathbf{K}^{(e)} \mathbf{T}^{(e)} = \mathbf{F}^{(e)} + \mathbf{Q}^{(e)} \quad (7.16)$$

where

$$\begin{aligned}
\mathbf{T}^{(e)} &= \begin{Bmatrix} T_1^{(e)} \\ T_2^{(e)} \end{Bmatrix}, & \dot{\mathbf{T}}^{(e)} &= \frac{d}{dt} \begin{Bmatrix} T_1^{(e)} \\ T_2^{(e)} \end{Bmatrix}, \\
\mathbf{M}^{(e)} &= \int_{x_1^{(e)}}^{x_2^{(e)}} \rho C \begin{bmatrix} \phi_1^{(e)} \phi_1^{(e)} & \phi_1^{(e)} \phi_2^{(e)} \\ \phi_2^{(e)} \phi_1^{(e)} & \phi_2^{(e)} \phi_2^{(e)} \end{bmatrix} dx, \\
\mathbf{K}^{(e)} &= \int_{x_1^{(e)}}^{x_2^{(e)}} k_x \begin{bmatrix} \frac{\partial \phi_1^{(e)}}{\partial x} \frac{\partial \phi_1^{(e)}}{\partial x} & \frac{\partial \phi_1^{(e)}}{\partial x} \frac{\partial \phi_2^{(e)}}{\partial x} \\ \frac{\partial \phi_2^{(e)}}{\partial x} \frac{\partial \phi_1^{(e)}}{\partial x} & \frac{\partial \phi_2^{(e)}}{\partial x} \frac{\partial \phi_2^{(e)}}{\partial x} \end{bmatrix} dx \\
\mathbf{F}^{(e)} &= \int_{x_1^{(e)}}^{x_2^{(e)}} \begin{Bmatrix} \phi_1^{(e)} \\ \phi_2^{(e)} \end{Bmatrix} \cdot H dx \\
\mathbf{Q}^{(e)} &= \begin{Bmatrix} -k_x \frac{\partial T}{\partial x} \Big|_{x=x_1^{(e)}} \\ k_x \frac{\partial T}{\partial x} \Big|_{x=x_2^{(e)}} \end{Bmatrix}
\end{aligned} \tag{7.17}$$

#### 7.2.4. Numerical Time Integration

The time dependent problem (7.6) is solved numerically by a finite difference scheme. We begin by assuming that the two temperature states  $\mathbf{T}_i$  at time  $t_i$  and  $\mathbf{T}_{i+1}$  at time  $t_{i+1}$  are related by

$$\mathbf{T}_{i+1} = \mathbf{T}_i + [(1 - \theta)\dot{\mathbf{T}}_i + \theta\dot{\mathbf{T}}_{i+1}] \Delta t, \quad 0 \leq \theta \leq 1 \tag{7.18}$$

where  $\Delta t = t_{i+1} - t_i$  denotes the time step. The relation (7.18) follows from the trapezoidal rule, where the parameter  $\theta$  is chosen by the user. Next we express (7.17) in the global form as

$$\mathbf{KT} + \mathbf{M}\dot{\mathbf{T}} = \mathbf{F} \tag{7.19}$$

By using  $t_i$  and  $t_{i+1}$ , we have

$$\begin{aligned}\mathbf{K}\mathbf{T}_i + \mathbf{M}\dot{\mathbf{T}}_i &= \mathbf{F}_i, \\ \mathbf{K}\mathbf{T}_{i+1} + \mathbf{M}\dot{\mathbf{T}}_{i+1} &= \mathbf{F}_{i+1}\end{aligned}\tag{7.20}$$

Then multiplying the first equation in (7.20) by  $(1 - \theta)$  and the second by  $\theta$ ,

$$\begin{aligned}(1 - \theta)(\mathbf{K}\mathbf{T}_i + \mathbf{M}\dot{\mathbf{T}}_i) &= (1 - \theta)\mathbf{F}_i, \\ \theta(\mathbf{K}\mathbf{T}_{i+1} + \mathbf{M}\dot{\mathbf{T}}_{i+1}) &= \theta\mathbf{F}_{i+1}\end{aligned}\tag{7.21}$$

which, after adding together, gives

$$\mathbf{M}[(1 - \theta)\dot{\mathbf{T}}_i + \theta\dot{\mathbf{T}}_{i+1}] + \mathbf{K}[(1 - \theta)\mathbf{T}_i + \theta\mathbf{T}_{i+1}] = (1 - \theta)\mathbf{F}_i + \theta\mathbf{F}_{i+1}\tag{7.22}$$

Now, using (7.18), we delete the time derivative terms and get

$$\frac{\mathbf{M}(\mathbf{T}_{i+1} - \mathbf{T}_i)}{\Delta t} + \mathbf{K}[(1 - \theta)\mathbf{T}_i + \theta\mathbf{T}_{i+1}] = (1 - \theta)\mathbf{F}_i + \theta\mathbf{F}_{i+1}\tag{7.23}$$

Rewriting this equation, we have

$$\left(\frac{1}{\Delta t}\mathbf{M} + \theta\mathbf{K}\right)\mathbf{T}_{i+1} = \left[\frac{1}{\Delta t}\mathbf{M} - (1 - \theta)\mathbf{K}\right]\mathbf{T}_i + (1 - \theta)\mathbf{F}_i + \theta\mathbf{F}_{i+1}\tag{7.24}$$

The time integration to solve for  $\mathbf{T}$  is carried out as follows:

- Given a known initial temperature  $T_0$  at time  $t = 0$  and a time step  $\Delta t$ ;
- Determine  $T_1$  at  $t = \Delta t$ , which is not known, by using (7.24);
- Use  $T_1$  to determine  $T_2$  at  $t = 2 \Delta t$ ; and so on.

### 7.3. Simulation Results

Considerable work has been done in developing exposure standards for radio frequency (RF) radiation. Exposure standards for microwave energy [in particular, ANSI/IEEE C95.1-1992 and ICNIRP] specify times over which the exposure is to be averaged. In ANSI/IEEE and ICNIRP, these times range from 6 to 30 min, with shorter times at frequencies above 1 GHz. Thus to calculate our simulation results with the standards and with [60]; temperature rise occurred by incident power density of  $5 \text{ mW/cm}^2$  and  $10 \text{ mW/cm}^2$  in the surface of cornea was calculated respectively at certain frequencies for exposure time of 6 min.

In this study, the temperature rise in the human eye is computed as follows. First, all tissues in the eye model are assigned a temperature of  $37^\circ\text{C}$ . By using (7.6) (with  $H(x, t) = 0$ ), the temperature in the steady state is computed in order to obtain the initial temperature distribution in the eye in the absence of microwave exposure. Secondly, the  $H(x, t)$  in the eye exposed to microwave is added to (7.6). This is used as the heat source in (7.6) to compute the temperature rise to the steady state with in the eye. Finally, the temperature difference before and after microwave exposure is derived as the temperature rise. The human eye tissue parameters were given in Chapter 6.

Web-spline simulation results with the results of the simplified bioheat equation for the surface temperature ((7.9), 7.10) are given in Table 7.2 for linear, quadratic and cubic web-spline. Results are also given in graphics in Figure 7.2 and Figure 7.3 for  $5 \text{ mW/cm}^2$  and  $10 \text{ mW/cm}^2$  incident power densities, respectively at the frequency range of 1-30 GHz.

It is shown in the simulated figures that as the degree of the spline functions increase temperature increase agrees well with [60] solutions.

Variation of temperature rise of cornea surface to exposure time by means of IC-NIRP and ANSI/IEEE exposure limits at 30 GHz for  $5 \text{ mW/cm}^2$  and  $10 \text{ mW/cm}^2$  is

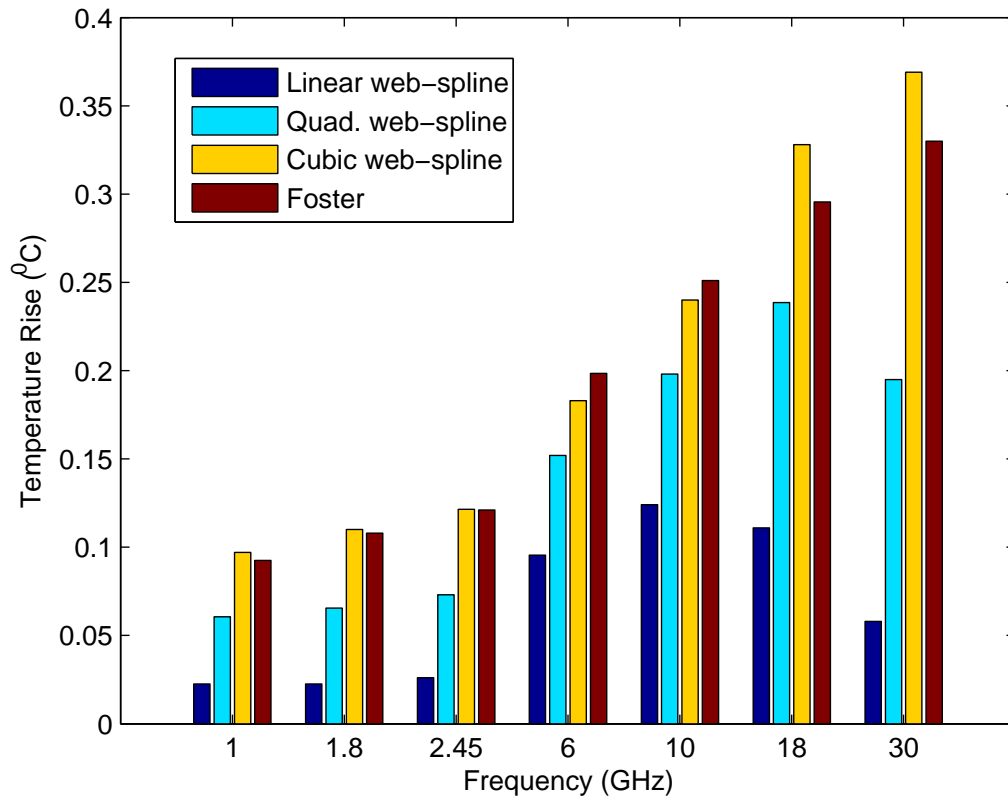


Figure 7.2. Temperature rise on the cornea surface at 6 min. duration at  $5 \text{ mW/cm}^2$

shown in Figure 7.4. For comparison reason, temperature rise of cornea surface versus exposure times are simulated with linear, quadratic and cubic web-spline model; and [60]'s at 6 GHz and 10 GHz with  $5 \text{ mW/cm}^2$  incident power density. Findings are depicted in Figure 7.5 and in Figure 7.6, respectively. It is clearly seen that cubic web-spline solution of bioheat equations give more accurate results than linear, and quadratic web-splines when compared with [60] model. Temperature variation depending on depth of skin eye tissue using web-spline technique was simulated for 6 min exposure times. Skin dept simulations are plotted in Figure 7.7 with the power density of  $5 \text{ mW/cm}^2$  at 2.45 GHz, 6 GHz and 10 GHz frequencies respectively for cubic web-splines.

#### 7.4. Conclusion

Temperature rise on the cornea surface for plane wave exposure have been investigated by using bioheat equation with web-spline model at the frequency range of 1

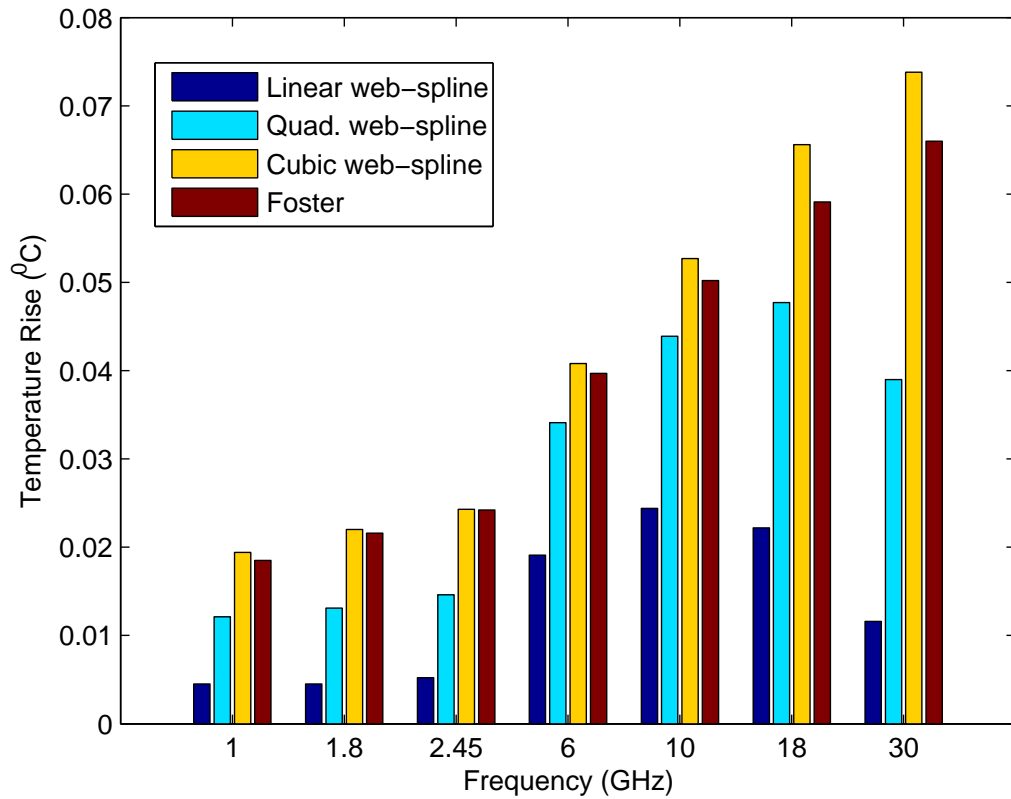
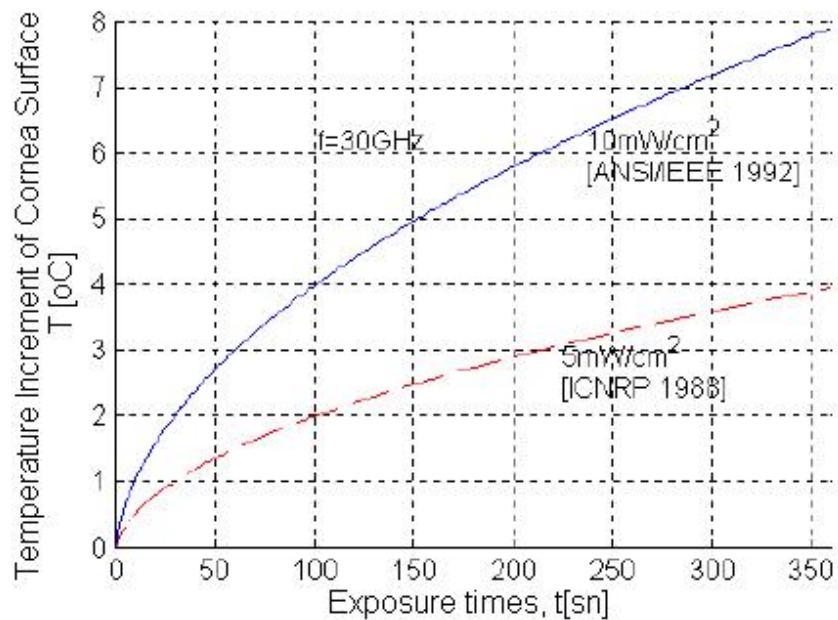


Figure 7.3. Temperature rise on the cornea surface at 6 min. duration at  $10 \text{ mW/cm}^2$  GHz and 30 GHz. Since radio frequency EM energy be absorbed in cornea on the front of surface of the eye, so the threshold temperature rise is  $3.0^\circ\text{C}$  for cataract formation. Maximum temperature rise due to power density of  $5 \text{ mW/cm}^2$ , which is the maximum permissible exposure limit for controlled environment [ICNIRP 1998], is found to be  $0.058^\circ\text{C}$ ,  $0.195^\circ\text{C}$ , and  $0.369^\circ\text{C}$  at 30 GHz for linear, quadratic and cubic web-splines, respectively. For power density of  $10 \text{ mW/cm}^2$  [ANSI/IEEE 1992], it is found to be  $0.116^\circ\text{C}$ ,  $0.39^\circ\text{C}$ , and  $0.66^\circ\text{C}$  at 30 GHz for linear, quadratic and cubic web-splines, respectively.

Table 7.2. Temperature increase values on the cornea surface for plan wave exposure

Frequency (GHz)	$I_0 = 5mW/cm^2$				$I_0 = 10mW/cm^2$			
	$n = 1$	$n = 2$	$n = 3$	<i>Foster</i>	$n = 1$	$n = 2$	$n = 3$	<i>Foster</i>
1	0.023	0.061	0.097	0.093	0.045	0.121	0.194	0.185
1.8	0.023	0.066	0.110	0.108	0.045	0.131	0.220	0.216
2.45	0.026	0.073	0.122	0.121	0.052	0.146	0.243	0.242
6	0.095	0.152	0.183	0.199	0.191	0.341	0.408	0.397
10	0.124	0.198	0.240	0.251	0.244	0.439	0.527	0.502
18	0.111	0.239	0.328	0.296	0.222	0.477	0.656	0.591
30	0.058	0.195	0.369	0.330	0.116	0.390	0.738	0.660

Figure 7.4. Temperature rise on the cornea surface at 6 min. duration at 10  $mW/cm^2$

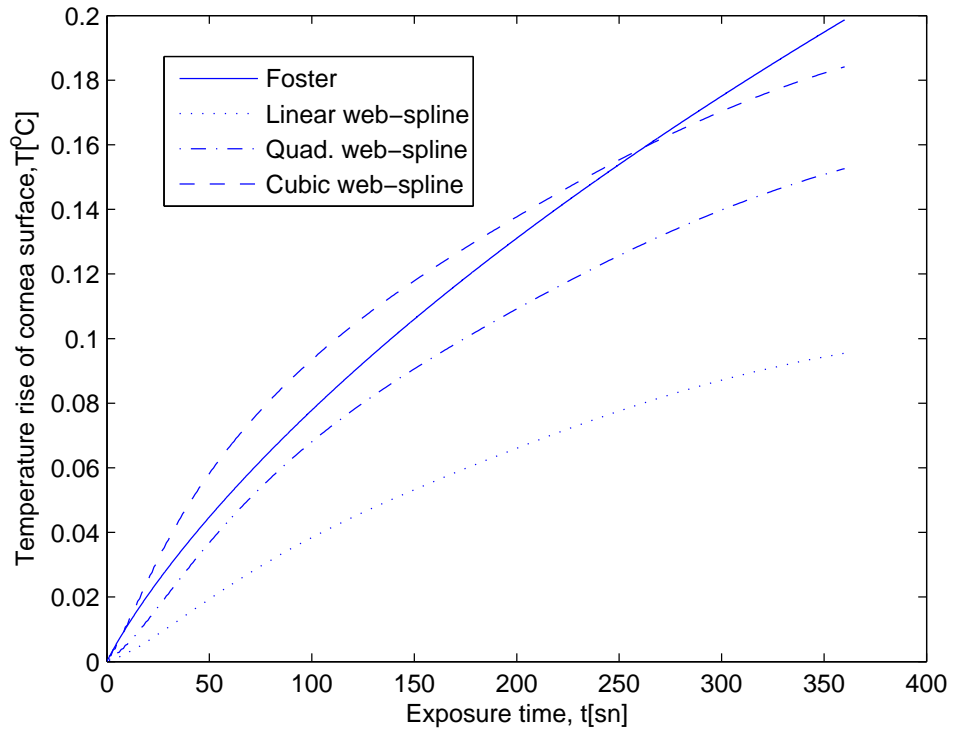


Figure 7.5. Temperature rise on the cornea surface at 6 min. duration at 6 GHz

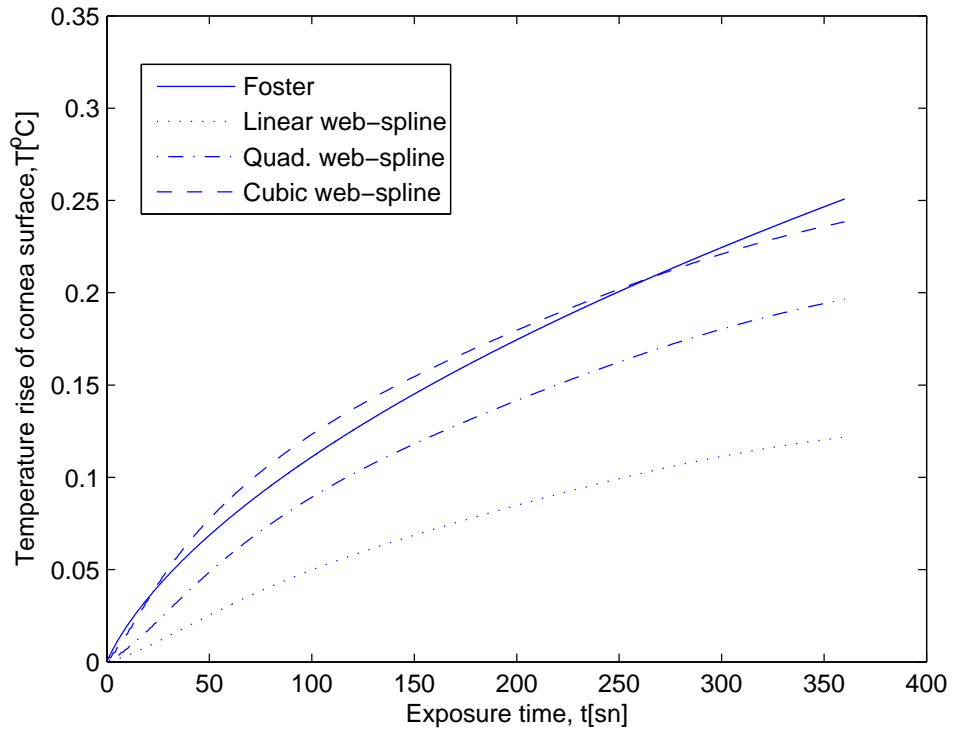


Figure 7.6. Temperature rise on the cornea surface at 6 min. duration at 10 GHz

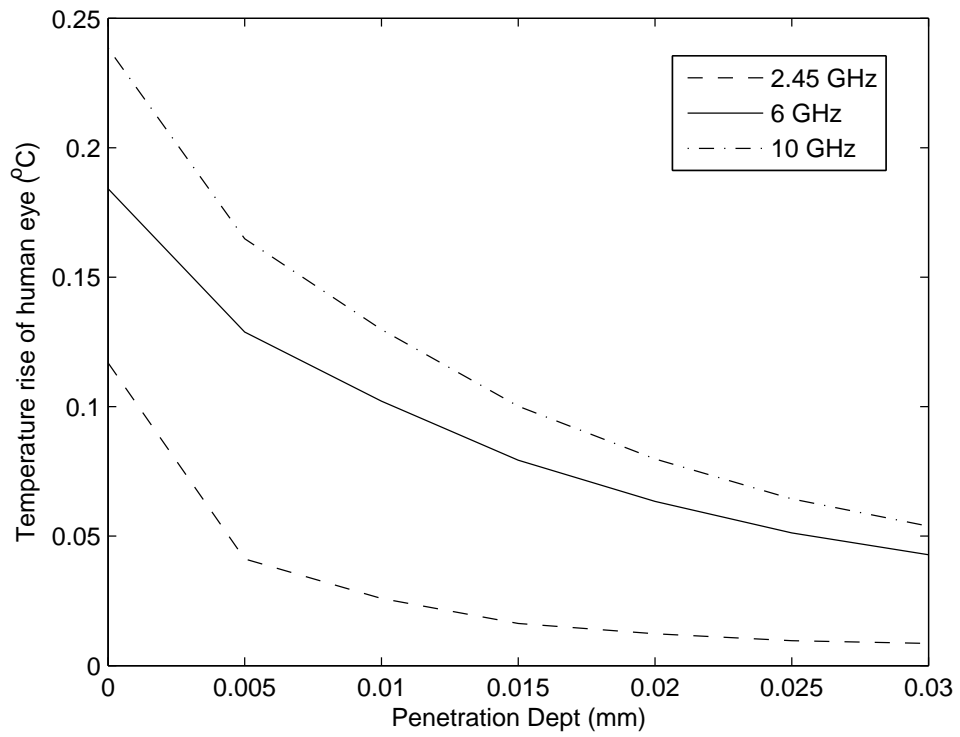


Figure 7.7. Cubic web-spline solution of temperature rise on the human eye for  $I_0 = 5mW/cm^2$  at 10 GHz (-.), 6 GHz (-) and 2.45 GHz (-)

## 8. CONCLUSIONS

The numerical computational electromagnetics in scattering, biomedical problems, and antenna design are taken into consideration in various journals and conferences. There are several numerical methods, which are given attention. One of the popular numerical methods is the Finite Element Method, which is very effective for inhomogeneous materials and allows complex geometries to be represented very precisely. It is a versatile and flexible numerical technique that is often used in the analysis of geometrical complex structures. It is also used in scattering, radiation, and propagation problems.

In this thesis we proposed the use of extended and weighted extended b-spline method to numerically study the electromagnetic models and bioheat transfer problems. Firstly, we have concentrated on using the web-spline to solve the electrostatic and electromagnetic wave problems in cylindrical coordinates. Secondly, a bioheat transfer model of the human eye is constructed using web-splines as shape functions for the FEM to calculate the steady-state temperature distribution in a normal 2D and 3D human eye. Finally, the heat conduction model of the microwave-irradiated eye is constructed.

### 8.1. Contributions and Discussion

This new method bridges the gap between geometric modeling and numerical simulation. In this dissertation, we introduce and implement a minimal degree variant of the web-method for 2D axisymmetric boundary value problems. It is intended primarily for simulations where computational speed is of key importance and only moderate accuracy in simulation parameters are required. Electrostatic, and EM wave equation as a basic model problem already exhibit the essential features of the new method. The wave equation in cylindrical coordinates has been solved and accurate results have been obtained by increasing the degree of the basis function.

FEM with web-splines are applied to analyze the steady-state temperature distribution in 2D and 3D models of the human eye with no external sources. Grid width ( $h$ ) optimization is done by decreasing  $h$  in dependence of the domain. It is observed that below 0.0625mm and 0.125mm in 2D and 3D web-spline models, respectively, decreasing  $h$  does not affect the results substantially. Thus, for saving the computational power and memory, higher numbers of grids are not tested. With the grid convergence number estimates, it is shown that this method reaches higher precision in a shorter period of time with fewer nodes. It is depicted that the errors decrease with increasing basis spline degrees. Besides diminishing the number of nodes, low computational time is also achieved by the web-spline method. The results indicate that FEM with web-spline method is observed to offer a much better performance than the standard FEM.

In this dissertation, the temperature rise in the cornea layer for plane wave exposure are investigated with the tissue block model by using Penne's bioheat equation with the new method, FEM with web-spline, at the frequency range of 1 – 30GHz. We compare our results with the ANSI/IEEE and ICNIRP exposure standards for microwave radiation with respect to the maximal increase in the surface of cornea temperature that would be allowed at the maximal permissible exposures. Subsequently it has been observed that our web-spline model agrees well with the solutions of the simplified bioheat equations especially for higher order b-splines. Finally, temperature variations at varying eye tissue thicknesses at different frequencies were calculated by using incident power density of 5  $mW/cm^2$ .

## 8.2. Future Directions

Eliminating the difficult and time consuming preprocessing step in computational techniques is still a challenge. The constructed 3D web-spline model is to use a number of applications. We plan to address this challenge in different heat sources exposed to human eye. Web-spline technique can also be applicable to finding tumors in the human bodies and it can be used on the other EM problems.

## REFERENCES

1. Yee, K. S., “Numerical Solution of Initial Boundary Value Problems Involving Maxwell’s Equations in Isotropic Media”, *IEEE Transactions on Antennas and Propagation*, Vol. 14, No. 6, pp. 302-307, May 1966.
2. Haupt, R. L., *Part 15: Numerical Techniques*, Handbook of Engineering Electromagnetics, Utah State University, Logan, Utah, U.S.A, 2000.
3. Trowbridge, C. W., *Part 44: Three Dimensional Analysis*, The Electrical Engineering Handbook, Boca Raton: CRC Press LLC, 2000.
4. Sadiku, M., *Numerical Techniques in Electromagnetics*, Second Edition, CRC Press LLC, New York, 2001.
5. De Boor, C., “On Calculating with B-splines”, *Journal of Approximation Theory*, Vol. 6, pp. 50-62, 1972.
6. De Boor, C., *A Practical Guide to Splines*, Applied Mathematics Series 27, Springer-Verlag, New York, 1978.
7. Kipp, A., *Spline Galerkin Approximation*, Ph.D. Thesis, University of Stuttgart, 1998.
8. Zhou, X., “Physical Spline Finite Element (PSFEM) Solutions to One Dimensional Electromagnetic Problems”, *Progress in Electromagnetics Research*, Vol. 40, pp. 271-294, 2003.
9. Han, J. G., W. X. Ren and Y. Huang “A Spline Wavelet Finite-Element Method in Structural Mechanics”, *International Journal for Numerical Methods in Engineering*, Vol. 66, pp. 166-190, 2006.
10. Hollig, K., *Finite Element Methods with B-splines*, Frontiers in Applied Mathe-

- matics, Vol. 26, Society for Industrial and Applied Mathematics (SIAM), Philadelphia, 2003.
11. Srinivas, V. K., V. K. Rathish, P. C. Das, “Weighted Extended B-spline Method for the Approximation of the Stationary Stokes Problem”, *J. Comput. Appl. Math.*, Vol. 186, pp. 335-348, 2006.
  12. Apaydin, G., S. Seker and N. Ari, “Weighted Extended B-splines for One Dimensional Electromagnetic Problems”, *Applied Mathematics and Computation*, Vol. 190, pp. 1125-1135, 2007.
  13. Apaydin, G., S. Seker and N. Ari, “Application of Web-spline Method in Electromagnetics”, *International Journal of Electronic and Communication (AEU)*, Vol.62, pp. 163-173, 2008.
  14. Kunter, F. C., G. Apaydin, N. Ari, S. Seker, “Use of Web-splines for Waveguide of Arbitrary Domain”, *Asia Pac. Microw. Conf.*, Hong Kong and Macau, December 16-20, 2008.
  15. Kunter, F. C., G. Apaydin, N. Ari, S. Seker, “Web-spline Solution of Axisymmetric Cylindrical Problems”, *Asia Pac. Microw. Conf.*, Hong Kong and Macau, December 16-20, 2008.
  16. Apaydin, G., “Efficient Finite Element Method for Electromagnetics”, *IEEE Antennas and Propagation Magazine*, Vol. 51, No. 5, pp. 61-71, 2009.
  17. Kunter, F. C., S. Seker, “Heat Transfer Model of the Human Eye Using Web-Spline Technique”, *14th Biennial IEEE Conference on Electromagnetic Field Computations (IEEE CEFC2010)*, May 9-12, Chicago, Illinois, USA, 2010.
  18. Kunter F. C., S. Seker, “3D web-splines solution to human eye heat distribution using bioheat equation”, *Engineering Analysis with Boundary Elements*, Vol. 35, pp. 639-646, 2011.

19. Kunter, F. C., S. Seker, “Using Bioheat Equation 3D Web-Spline Prediction of Ocular Surface Temperature”, *29th Progress in Electromagnetics Research Symposium*, PIERS 2011, Marrakesh, Morocco, March 20-23, 2011.
20. Faraday, M., *Experimental Researches in Electricity*, Seventh Series, Philosophical Transactions of The Royal Society, London, 1834.
21. Maxwell, J. C., *A Treatise on Electricity and Magnetism*, Dover Publications, New York, 1954.
22. Guru, B., H. Hizirođlu *Electromagnetic Field Theory Fundamentals (2nd Edition)*, Cambridge University Press, 2004.
23. Jin, J., *The Finite Element Method in Electromagnetics*, John Wiley and Sons, 1993.
24. Ho, S. L., S. Yang, J. M. Machado and H. C. Wong, “Application of A Meshless Method in Electromagnetics”, *IEEE Transactions on Magnetics*, Vol. 37, No. 5, pp. 3198-3202, 2001.
25. Volakis, J. L., A. Chatterjee and L. C. Kempel, *Finite Element Method for Electromagnetics*, IEEE Press, New York, 1998.
26. Babushka, I., “The Finite Element Method with Penalty”, *Mathematics of Computation*, Vol. 27, No. 122, pp. 221-228, 1973.
27. Belytschko, T., Y. Krongauz, D. Organ, M. Fleming and P. Krysl, “Meshless Methods: An Overview and Recent Developments”, *Computation Methods in Applied Mechanics and Engineering*, Vol. 139, pp. 3-47, 1999.
28. Wendland, H., “Meshless Galerkin Methods Using Radial Basis Functions”, *Mathematical Computations*, Vol. 68, No. 228, pp. 1521-1531, 2002.
29. Hollig, K., U. Reif and J. Wipper, “Error Estimates for the Web-method”, *Mathe-*

- mathematical Methods for Curves and Surfaces: Oslo 2000*, Vanderbilt University Press, Nashville, TN, pp. 195-209, 2000.
30. Hollig, K., U. Reif and J. Wipper, “Weighted Extended B-spline Approximation of Dirichlet Problems”, *SIAM Journal on Numerical Analysis*, Vol. 39, No. 2, pp. 442-462, 2001.
  31. Hollig, K., U. Reif and J. Wipper, *B-spline Approximation of Neumann Problems*, Mathematics Institute, University of Stuttgart, 2002.
  32. Hollig, K., U. Reif and J. Wipper, “Multigrid Methods with Web-splines”, *Numerische Mathematik*, Vol. 91, No. 2, pp. 237-256, 2002.
  33. Hollig, K., *Handbook of Computer Aided Geometric Design: Finite Element Approximation with Splines*, Mathematics Institute, Elsevier, Amsterdam, pp. 283-308, 2002.
  34. Hollig, K., C. Apprich and A. Streit, “Introduction to the Web-method and its Application”, *Advances in Computational Mathematics*, Vol. 23, pp. 215-237, 2005.
  35. Rvachev, V. L., “Analytical Description of some Geometric Objects”, *Dokl AS USSR*, Vol. 153, No: 4, pp. 765-768, 1963.
  36. Rvachev, V. L., A. N. Shevchenko and V. V. Veretelnik, “Numerical Integration Software for Projection and Projection-grid Methods”, *Cybernetics and System Analysis*, Vol. 30, pp. 154-158, 1994.
  37. Rvachev, V. L. and T. I. Sheiko, “R-functions in Boundary Value Problems in Mechanics”, *Applied Mechanics Reviews*, Vol. 48, No: 4, pp. 151-188, 1996.
  38. Becker, E. B., G. F. Carey, J. T. Oden, “One Dimensional Problems in Finite Elements”, vol. 1, Englewood Cliffs, N.J., Prentice-Hall, USA, 1981.

39. Segerlind, L. J., "Applied Finite Element Analysis", John Wiley and Sons, Inc., USA, 1976.
40. Buchanan, G. R., "One Dimensional Finite Elements, in: Schaum's Outline of Theory and Problems of Finite Element Analysis", McGraw-Hill, Inc., USA, pp. 27-34, 1995.
41. Paris, D. T., F. K. Hurd, "Basic Electromagnetic Theory", McGraw-Hill Book Company, New York, USA, 1969.
42. Taflove, A., M. Brodwin, "Computation of the Electromagnetic Fields and Induced Temperatures Within a Model of the Microwave-irradiated Human Eye", *IEEE Trans. Microw. Theory Tech. MTT-23*, Vol. 11, pp. 888-896, 1975.
43. Al-Badwaihy, K. A., A.B. Youssef, "Biological Effects of Electromagnetic Waves", Vol. 1, ed. C. C. Johnson and M. L. Shore HEW Publication, pp. 61-78, 1976.
44. Legendijk, J. W., "A Mathematical Model to Calculate Temperature Distributions in Human and Rabbit Eyes during Hyperthermic Treatment", *Phys. Med. Biol.*, Vol. 27, No. 11, pp. 1301-1311, 1982.
45. Hirata, A., S. Matsuyama, T. Shiozawa, "Temperature Rises in the Human Eye Exposed to EM Waves in the Frequency Range 0.6-6 GHz", *IEEE Trans. Electromagn. Compat.*, Vol. 42, No. 4, pp. 386-393, 2000.
46. Emery, A. F., P. Kramar, A. W. Guy, J. C. Lin, "Microwave 466 Induced Temperature Rises in Rabbit Eyes in Cataract Research", *Int. J. Heat Transfer*, Vol. 97, pp. 123-128, 1975.
47. Guy, A., J. C. Lin, P. O. Kramar, A. F. Emery, "Effect of 2450 MHz Radiation on the Rabbit Eye", *IEEE Trans. Microw. Theory Tech. MTT-23*, Vol. 6, pp. 492-498, 1975.
48. Amara, E. H., "Numerical Investigations on Thermal Effects of Laser Ocular

- Media Interaction”, *Int J.Heat Mass Trans.*, Vol. 38, pp. 2479-2488, 1995.
49. Scott, J. A., “A Finite Element Model of Heat Transport in the Human Eye”, *Phys. Med. Biol.*, Vol. 33, No. 2, pp. 227-241, 1988.
  50. Scott, J. A., “The Computation of Temperature Rises in the Human Eye Induced by Infrared Radiation”, *Phys. Med. Biol.*, Vol. 33, No. 2, pp. 243-257, 1988.
  51. Ng, E. Y. K., E. H. Ooi, “FEM Simulation of the Eye Structure with Bioheat Analysis”, *Comput. Methods Programs Biomed.*, Vol. 82, No. 3, pp. 268-276, 2006.
  52. Ng, E. Y. K., E. H. Ooi, “Ocular Surface Temperature: A 3D FEM Prediction Using Bioheat Equation”, *Comput. Biol. Med.*, Vol. 37, pp. 829-835, 2007.
  53. Ooi, E. H., W. T. Ang, E. Y. K. Ng, “Bioheat Transfer in the Human Eye: A Boundary Element Approach”, *Eng. Anal. Bound. Elem.*, Vol. 31, pp. 494-500, 2007.
  54. Ooi, E. H., W. T. Ang, E. Y. K. Ng, “A Boundary Element model of the human eye undergoing laser thermokeratoplasty”, *Comput. Biol. Med.*, Vol. 38, pp. 727-737, 2008.
  55. Ooi, E. H., W. T. Ang, E. Y. K. Ng, “A Boundary Element Model for Investigating the Effects of Eye Tumor on the Temperature Distribution Inside the Human Eye”, *Comput. Biol. Med.*, Vol. 39, pp. 667-677, 2009.
  56. Ooi, E. H., E. Y. K. Ng, “Effects of Natural Convection Within the Anterior Chamber on the Ocular Heat Transfer”, *Int. J. Numer. Meth. Biomed. Engng*, (doi: 10.1002/cnm.1411, 2010.
  57. Ooi, E. H., E. Y. K. Ng, “Ocular Temperature Distribution: A Mathematical Perspective”, *J. Mech. Med. Biol.*, Vol.9, No. 2, pp. 199-227, 2009.
  58. Pennes, H. H., “Analysis of Tissue and Arterial Blood Temperatures in the

- Resting Forearm”, *Journal of Applied Physiology*, Vol. 1, pp. 93-122, 1948.
59. Gandhi, O. P., A. Rzaei, “Absorption of Millimeter waves by Human Beings and its Biological Implications”, *IEEE Trans. on Microwave Theory and Techniques*, Vol. MTT-34, pp. 228-235, 1986.
  60. Foster K. R., L. Nozano-Lieto, P. J. Riu, “Heating of Tissues by Microwave: A model Analysis”, *Bioelectromagnetics*, Vol. 19, pp. 420-428, 1998.
  61. Sukru, O., S. Comlekci, O. Cerezci, O. Polat, “Electrical Properties of Human Eye and Temperature Increase Calculation at the Cornea Surface for RF Exposure”, *Biological Effects of EMFs 2nd International Workshop Proceedings*, Vol. 2, Rhodes, Greece, 7-11 October, 2002.
  62. Sukru, O., “Mikrodalga Frekansli EM Radyasyona Maruz Kalan Biyolojik Dokularda Olusan Isil etkinin Teorik ve Deneysel Incelenmesi”, *Sakarya Universitesi, Fen Bilimleri Enstitusu, Thesis*, May 2003.
  63. Wang J., O. Fujiwara, “FDTD Computation of Temperature Rise in the Human Head for Portable Telephones”, *IEEE Transactions on Microwave Theory and Techniques*, Vol. 47, pp. 1528-1534, 1999.
  64. Flyckt, V. M. M., B.W. Raaymakers, H. Kroeze, J.J.W. Lagendijk, “Calculation of SAR and Temperature Rise in a High-Resolution Vascularized Model of the Human Eye and Orbit When Exposed to a Dipole Antenna at 900, 1500 and 1800 MHz”, *Physics in Medicine and Biology*, Vol. 52, pp. 2691-2701, 2007.
  65. Bernardi, P., M. Cavagnaro, S. Pisa, “Evaluation of the Power Absorbed in Human Eyes Exposed to Millimeter Waves”, *International Symposium on Electromagnetics Compatibility*, Rome, Italy, pp. 194-199, 1996.
  66. Bernardi, P., M. Cavagnaro, S. Pisa, E. PiuZZi, “SAR Distribution and Temperature Increase in an Anatomical Model of the Human Eye Exposed to the

- Field Radiated by the User Antenna in a Wireless LAN”, *IEEE Transactions on Microwave Theory and Techniques*, Vol. 46, pp. 2074-2082, 1998.
67. Hirata A., T. Shiozawa, “Heat Transportation Models of the Human Eye for Microwave Exposures”, *Proceeding of the International Workshop Ocular Side-Effects by Non- Ionizing Radiation*, Ishikawa, Japan, 2003.
  68. Hirata A., “Temperature Increase in Human Eyes Due to Near-Field and Far Field Exposures at 900MHz, 1.5GHz and 1.9GHz”, *IEEE Transactions on Electromagnetic Compatibility*, Vol. 47, pp. 68-76, 2005.
  69. Hirata, A., “Improved Heat Transfer Modeling of the Eye for Electromagnetic Wave Exposures”, *IEEE Transactions on Biomedical Engineering*, Vol. 54, pp. 959-961, 2007.
  70. Seker, S., H. Abatay, “New frequency-dependent parametric modeling of dielectric materials, *Int. J. Electronic and Comm. (AEU)*, Vol. 60, pp. 320-327, 2006.